

Advances in Meteorology

# Carbonaceous Particles in the Atmosphere: Experimental and Modelling Issues

Guest Editors: Giulia Pavese, Lucas Alados-Arboledas, Junji Cao, and S. K. Satheesh





---

# **Carbonaceous Particles in the Atmosphere: Experimental and Modelling Issues**

Advances in Meteorology

---

## **Carbonaceous Particles in the Atmosphere: Experimental and Modelling Issues**

Guest Editors: Giulia Pavese, Lucas Alados-Arboledas,  
Junji Cao, and S. K. Satheesh



---

Copyright © 2014 Hindawi Publishing Corporation. All rights reserved.

This is a special issue published in “Advances in Meteorology.” All articles are open access articles distributed under the Creative Commons Attribution License, which permits unrestricted use, distribution, and reproduction in any medium, provided the original work is properly cited.

## Editorial Board

Paulo Artaxo, Brazil  
Guy Brasseur, USA  
Mladjen Ćurić, Serbia  
Raymond Desjardins, Canada  
Klaus Dethloff, Germany  
Panuganti C. S. Devara, India  
Julio Diaz, Spain  
Shouting Gao, China  
Luis Gimeno, Spain

Sven-Erik Gryning, Denmark  
Ismail Gultepe, Canada  
Hiroyuki Hashiguchi, Japan  
Didier Hauglustaine, France  
Ivar S A Isaksen, Norway  
Yasunobu Iwasaka, Japan  
Hann-Ming H. Juang, USA  
George Kallos, Greece  
Harry D. Kambezidis, Greece

Richard Leitch, Canada  
Monique Leclerc, USA  
Gwo-Fong Lin, Taiwan  
Edward Llewellyn, Canada  
Kyaw T. Paw, USA  
Sara C. Pryor, USA  
Eugene Rozanov, Switzerland  
Zhihua Zhang, China

## Contents

**Carbonaceous Particles in the Atmosphere: Experimental and Modelling Issues**, Giulia Pavese, Lucas Alados-Arboledas, Junji Cao, and S. K. Satheesh  
Volume 2014, Article ID 529850, 2 pages

**Black Carbon and Elemental Carbon from Postharvest Agricultural-Waste Burning Emissions in the Indo-Gangetic Plain**, Atinderpal Singh, Prashant Rajput, Deepti Sharma, M. M. Sarin, and Darshan Singh  
Volume 2014, Article ID 179301, 10 pages

**Annual Patterns of Atmospheric Pollutions and Episodes over Cairo Egypt**, Y. Aboel Fetouh, H. El Askary, M. El Raey, M. Allali, W. A. Sprigg, and M. Kafatos  
Volume 2013, Article ID 984853, 11 pages

**Spatial and Temporal Trends in PM<sub>2.5</sub> Organic and Elemental Carbon across the United States**, J. L. Hand, B. A. Schichtel, W. C. Malm, and N. H. Frank  
Volume 2013, Article ID 367674, 13 pages

**Comparison of Spheroidal Carbonaceous Particle Data with Modelled Atmospheric Black Carbon Concentration and Deposition and Air Mass Sources in Northern Europe, 1850–2010**, Meri Ruppel, Marianne T. Lund, Henrik Grythe, Neil L. Rose, Jan Weckström, and Atte Korhola  
Volume 2013, Article ID 393926, 15 pages

**Comparisons between Hygroscopic Measurements and UNIFAC Model Predictions for Dicarboxylic Organic Aerosol Mixtures**, Jae Young Lee and Lynn M. Hildemann  
Volume 2013, Article ID 897170, 9 pages

**Identification and Characterization of Black Carbon Aerosol Sources in the East Baltic Region**, Steigvilė Byčenkienė, Vidmantas Ulevicius, Vadimas Dudoitis, and Julija Pauraitė  
Volume 2013, Article ID 380614, 11 pages

## Editorial

# Carbonaceous Particles in the Atmosphere: Experimental and Modelling Issues

**Giulia Pavese,<sup>1</sup> Lucas Alados-Arboledas,<sup>2</sup> Junji Cao,<sup>3</sup> and S. K. Satheesh<sup>4</sup>**

<sup>1</sup> *Institute of Methodologies for Environmental Analysis, National Council of Research (CNR-IMAA),  
Contrada S. Loja, 85050 Tito Scalo, Italy*

<sup>2</sup> *Centro Andaluz de Medio Ambiente, University of Granada, 18071 Granada, Spain*

<sup>3</sup> *Key Laboratory of Aerosol, SKLLQG, Institute of Earth Environment, Chinese Academy of Sciences, Xi'an 710075, China*

<sup>4</sup> *Centre for Atmospheric and Oceanic Sciences, Indian Institute of Science, Bangalore 560012, India*

Correspondence should be addressed to Giulia Pavese; [pavese@imaa.cnr.it](mailto:pavese@imaa.cnr.it)

Received 11 May 2014; Accepted 11 May 2014; Published 26 May 2014

Copyright © 2014 Giulia Pavese et al. This is an open access article distributed under the Creative Commons Attribution License, which permits unrestricted use, distribution, and reproduction in any medium, provided the original work is properly cited.

Carbonaceous particles and their organic component are one of the major combustion by-products and they are recognized to play a relevant role in radiative transfer, air quality, and human health, due to their fine-submicrometric nature. These effects are magnified by transboundary air masses transport of natural fires plumes or anthropogenic emissions from domestic heating and industrial activities, affecting not only the source areas. In fact, analysis on snow samples from different arctic sites revealed the presence of carbonaceous particulate matter, with biomass burning identified as responsible for more than 90% of these particles. As a consequence of this deposition, snow albedo variations are added to the other factors influencing Earth's radiative budget.

For these reasons, there is a growing interest toward the above-mentioned arguments, but there is also a need to assess the role of carbonaceous particles [1] and to review the different measurements techniques, highlighting their limitations and uncertainties [2].

The papers included in this special issue improve the comprehension of processes involving carbonaceous particles considering them under different points of view because both experimental and modeling approaches are examined.

S. Byčenkienė et al., starting from one-year continuous aethalometer measurements of black carbon (BC) content at a background site in Lithuania, were able to study the transport of different air masses. In particular, air masses

from Ukraine and the volcanic plume from the Grimsvotn eruption were characterized by estimating the alpha absorption parameter at shorter and longer wavelengths. In this way, they demonstrate that grass burning was the major source of carbonaceous particles in the atmosphere. Moreover, new secondary particle formation from volcanic gas emissions, occurred within the lower troposphere, was detected even at a large distance from the eruption site.

Y. Aboel Fetouh et al. use long-term series of parameters from the Tropospheric Emission Spectrometer (TES) on board the Aura satellite to assess the dominant component below the inversion layer. Time series analysis, autocorrelations, and cross correlations were useful to understand the connections between those parameters and their local effect. In particular, they were able to identify different pollution episodes known as Black Clouds over Cairo city and their climatic origin, confirming biomass burning to be a serious problem affecting air quality in that area.

J. L. Hand et al. aggregated OC and EC data from 2007 to 2010 at over 300 sites from the rural/remote IMPROVE (interagency monitoring of protected visual environments) network and the Environmental Protection Agency's urban chemical speciation network to characterize the spatial and seasonal patterns in rural and urban carbonaceous aerosols. From the interpolation of these data, they found large spatial patterns from which local and regional impacts of carbonaceous aerosols across the United States were inferred.

In particular, they found urban impact the highest and more localized in the West in winter. Eastern particulate organic matter (POM) concentrations were the highest in the Southeast in spring, during prescribed fires, and were more regional during summer with a major influence of secondary sources.

M. Ruppel et al. compared sedimentary measurements of spheroidal carbonaceous particles (SCP), obtained from lake sediments in Northern Europe from 1850 to 2010, to model data from the chemistry transport model OsloCTM2. To determine the origin of SCPs, they generated back trajectories of air masses to the study sites. In general, they found a good agreement between trends of SCP deposition and modelled results but, on a smaller geographical scale, they highlighted the lack of detailed information on air mass transport patterns in the model, suggesting the need for numerous observational records to reliably validate model results.

J. Y. Lee and L. M. Hildemann studied the hygroscopic behavior at 12°C over aqueous bulk solutions containing dicarboxylic acids (malonic, glutaric, and succinic). They compared their results to Peng's modified UNIFAC model results. They observed systematic differences between measured and modelled hygroscopic behavior for mixtures of dicarboxylic acids couples, over a range of concentrations. These results suggest considering interactions between different organic components in order to accurately model aerosol hygroscopicity and, for this reason, further measurements are strongly requested.

A. Singh et al. measured the mass concentrations of both black carbon (BC) and elemental carbon (EC) in the Indo-Gangetic Plain (IGP), using both optical and thermo-optical techniques, with the objective to assess the characteristics of BC and EC from various kinds of biomass burning emissions. They observed BC/EC ratios greater than 1.0 during paddy-residue burning emissions associated with high mass concentrations of EC, OC, and OC/EC ratio and estimated the value of the Ångström exponent ( $\alpha$ ), derived from aethalometer data, that is, approximately 1.5, for the postharvest agricultural-waste burning emissions. This value was so far unknown for the IGP.

*Giulia Pavese*  
*Lucas Alados-Arboledas*  
*Junji Cao*  
*S. K. Satheesh*

## References

- [1] T. C. Bond, S. J. Doherty, and D. W. Fahey, "Bounding the role of black carbon in the climate system: a scientific assessment," *Journal of Geophysical Research: Atmosphere*, vol. 118, pp. 5380–5552, 2013.
- [2] D. A. Lack, H. Moosmüller, G. R. McMeeking, R. K. Chakrabarty, and D. Baumgardner, "Characterizing elemental, equivalent black, and refractory black carbon aerosol particles: a review of techniques, their limitations and uncertainties," *Analytical and Bioanalytical Chemistry*, vol. 406, pp. 99–122, 2014.

## Research Article

# Black Carbon and Elemental Carbon from Postharvest Agricultural-Waste Burning Emissions in the Indo-Gangetic Plain

Atinderpal Singh,<sup>1</sup> Prashant Rajput,<sup>2</sup> Deepti Sharma,<sup>1</sup> M. M. Sarin,<sup>2</sup> and Darshan Singh<sup>1</sup>

<sup>1</sup> Department of Physics, Punjabi University, Patiala 147 002, India

<sup>2</sup> Geosciences Division, Physical Research Laboratory, Ahmedabad 380 009, India

Correspondence should be addressed to Darshan Singh; dsjphy@yahoo.com

Received 21 March 2013; Revised 10 June 2013; Accepted 8 January 2014; Published 26 February 2014

Academic Editor: Lucas Alados-Arboledas

Copyright © 2014 Atinderpal Singh et al. This is an open access article distributed under the Creative Commons Attribution License, which permits unrestricted use, distribution, and reproduction in any medium, provided the original work is properly cited.

We compare the mass concentrations of black carbon (BC) and elemental carbon (EC) from different emissions in the Indo-Gangetic Plain (IGP), using optical (Aethalometer; 880 nm) and thermo-optical technique (EC-OC analyzer; 678 nm), respectively. The fractional contribution of BC mass concentration measured at two different channels (370 and 880 nm), OC/EC ratio, and non-sea-salt  $K^+$ /EC ratios have been systematically monitored for representing the source characteristics of BC and EC in this study. The mass concentrations of BC varied from 8.5 to 19.6, 2.4 to 18.2, and 2.2 to 9.4  $\mu\text{g m}^{-3}$  during October–November (paddy-residue burning emission), December–March (emission from bio- and fossil-fuel combustion) and April–May (wheat-residue burning emission), respectively. In contrast, the mass concentrations of EC varied from 3.8 to 17.5, 2.3 to 8.9, and 2.0 to 8.8  $\mu\text{g m}^{-3}$  during these emissions, respectively. The BC/EC ratios conspicuously greater than 1.0 have been observed during paddy-residue burning emissions associated with high mass concentrations of EC, OC, and OC/EC ratio. The Ångström exponent ( $\alpha$ ) derived from Aethalometer data is approximately 1.5 for the postharvest agricultural-waste burning emissions, hitherto unknown for the IGP. The mass absorption efficiency (MAE) of BC and EC centers at  $\sim 1\text{--}4\text{ m}^2\text{ g}^{-1}$  and  $2\text{--}3\text{ m}^2\text{ g}^{-1}$  during the entire study period in the IGP.

## 1. Introduction

Black carbon (BC) and elemental carbon (EC) are primary constituents of atmospheric aerosols produced from incomplete combustion of fossil fuel vis-à-vis biomass burning emission [1]. The atmospheric significance of BC and EC is due to their potential light absorption characteristics and recognition as a driver of the global warming demands for their spatial distribution and temporal variability records [2, 3]. Furthermore, the assessment of global climate change also reports a large uncertainty in the estimation of aerosol radiative forcing, arising mainly due to complexity in absorbing and scattering particles characteristics [4]. In addition, the impact of these light-absorbing aerosols on Indian summer monsoon and heating rates of the elevated regions of the Himalayan-Tibetan plateau has been realized [5, 6]. Thus, the records on atmospheric variability of BC as well as EC are

significantly important for assessing its impact on climate. A couple of earlier studies suggest the assessment of the role of organic aerosols when assessing the impact of absorbing aerosols (BC, EC) on the radiative forcing estimations [2, 7]. To assess the characteristics of BC and EC from various kinds of biomass burning emissions, we have conducted a campaign from a source region in the Indo-Gangetic Plain (IGP).

The terminology of black carbon and elemental carbon (BC, EC) has originated from their measurement technique. The BC refers to the light-absorbing part of the carbonaceous aerosols and is determined using optical method. In contrast, the EC is a refractory constituent of the aerosols and is determined using thermo-optical technique under oxidizing condition. In this study, we also adhere to this conventional terminology and report that BC concentrations are measured optically by Aethalometer at 880 nm, whereas EC concentrations are measured using thermo-optical method on

EC-OC analyzer at 678 nm. The optical method monitors the attenuation of light through aerosol-loaded filter at a given wavelength (here 880 nm by Aethalometer) and uses a constant attenuation cross section ( $\sigma_{\text{ATN}}$ ) of  $16.6 \text{ m}^2 \text{ g}^{-1}$  to determine the BC mass concentrations. However, several studies have addressed the issue on the spatial variability of  $\sigma_{\text{ATN}}$  [8–11]. In contrast, the thermo-optical method (EC-OC analyzer at 678 nm) determines the mass concentrations of organic and elemental carbon (OC, EC) in aerosols based on their chemical properties [10, 11].

The main objective of this study is to assess the characteristics of elemental and black carbon (EC and BC) based on their mass absorption efficiency (MAE). The fractional contribution of BC at 370 nm and 880 nm exhibits a typical signature of biomass burning emission during the paddy- and wheat-residue burning. In contrast, during wintertime the BC from mixed sources (fossil-fuel combustion and biomass burning) is observed. A similar characteristic for EC is also observed based on the chemical tracers such as the OC/EC and  $\text{nss-K}^+/\text{EC}$  ratios (non-sea-salt:  $\text{nss-K}^+$ ). Our study shows that BC/EC ratios are conspicuously greater than 1 during the postharvest paddy-residue burning emission (associated with relatively high concentration of EC, OC, and OC/EC ratio). Furthermore, we document the Ångström exponent ( $\alpha$ ) for entire range (370–950 nm) utilizing the Aethalometer data and also provide the absorption coefficient ( $b_{\text{abs}}$ ) and mass absorption efficiency (MAE:  $\sigma_{\text{abs}}$ ) of these absorbing aerosols (BC and EC) for the study period from October 2008 to May 2009 in the IGP.

## 2. Materials and Methods

**2.1. Site Description.** The sampling site at Patiala ( $30.2^\circ\text{N}$ ;  $76.3^\circ\text{E}$ ; 250 m above mean sea level) is located upwind of major population and industrial polluting sources in the Indo-Gangetic Plain (IGP; Figure 1). The site is strategically surrounded by agricultural fields (nearest distance  $\sim 1 \text{ km}$ ) and located in the state of Punjab, where over 84% of the land area is in use under the cultivation [12]. The present study has been carried out from October 2008 to May 2009. The entire study period from October to May is subdivided into three emission phases: October–November, referred to as postmonsoon, is influenced by emissions from postharvest paddy-residue burning; December–March, referred to as wintertime, is dominated by emissions from biofuel burning and fossil-fuel combustion [13]. Furthermore, the wintertime period in the IGP is associated with shallower atmospheric boundary layer and fog formation events. The time period from April to May, referred to as premonsoon, is influenced by postharvest wheat-residue burning emissions [13]. The period from June to September (SW-monsoon) is associated with frequent rain events that keep the ambient atmosphere relatively clean. For further details related to the site description, reference is made to our earlier publications [13, 14]. The important information on the assessment of emission budget of carbonaceous species (EC, OC, and polycyclic aromatic hydrocarbons) and determination of organic



FIGURE 1: Map showing the sampling site at Patiala in the Indo-Gangetic Plain (IGP) in Northern India.

mass-to-organic carbon (OM/OC) ratio for these aerosol samples has been documented elsewhere [15, 16].

**2.2. Methodology.** The mass concentrations of BC from the sampling site at Patiala were determined by an Aethalometer (model: AE-31, Magee Scientific, USA). It monitors the optical attenuation (absorbance) of light at seven wavelengths (370, 470, 520, 590, 660, 880, and 950 nm) with a typical half-width of 20 nm [17]. However, the BC mass concentration is assessed at 880 nm wavelength. While determining the BC mass concentration using Aethalometer, the change in attenuation of light passing through the filter is monitored for a given interval of time. Assuming that BC is the only absorbing component in the atmospheric aerosols, a linear relationship of BC mass concentration with the change in attenuation of light is used to determine the BC mass concentration [8, 18]. In this study, the attenuation signal has been integrated for 5 minutes and flow rate was maintained at  $3.4 \text{ L min}^{-1}$ . The analytical uncertainty in BC measurements is  $\sim \pm 2\%$  (as reported in the manual). However, it has also been reported that sometimes the BC mass concentrations can be overestimated due to presence of other absorbing aerosols in the atmosphere [19]. More details on the analytical technique of the Aethalometer can be found elsewhere [20, 21]. The Aethalometer uses a constant attenuation cross section ( $\sigma_{\text{ATN}}$ ) of  $16.6 \text{ m}^2 \text{ g}^{-1}$ , in determining the BC mass concentrations. The attenuation coefficient ( $b_{\text{ATN-AETH}}$ ;  $\text{Mm}^{-1}$ ) of BC from Aethalometer (at 880 nm) can be represented mathematically by the following equation:

$$b_{\text{ATN-AETH}} = \text{BC} (\mu\text{g}/\text{m}^3) \times 16.6 (\text{m}^2/\text{g}). \quad (1)$$

For the simultaneous determination of EC mass concentration from the same site, the ambient aerosols with

aerodynamic diameter less than  $2.5 \mu\text{m}$  ( $\text{PM}_{2.5}$ ) were collected onto the precombusted tisuquartz filters by filtering ambient air at a flow rate of  $\sim 1.2 \text{ m}^3 \text{ min}^{-1}$  using a high volume sampler (Thermo Scientific). During the first phase (October–November) of sampling, aerosols were collected for nearly 24 h continuously, whereas, during rest of the period, the sampling was integrated for 10–12 h for adequate aerosol collection. The EC mass concentrations were determined from a filter aliquot ( $1.5 \text{ cm}^2$  rectangular punch) using EC-OC analyzer (model 2000, Sunset Laboratory, USA), by NIOSH (National Institute for Occupational Safety and Health) thermo-optical transmittance (TOT) protocol [22, 23]. Briefly, employing the thermo-optical method on EC-OC analyzer, the organic carbon (OC) and elemental carbon (EC) are oxidized to  $\text{CO}_2$  separately, by heating the aerosol sample in inert (helium) and oxidizing conditions (helium + oxygen), respectively. Subsequent conversion of  $\text{CO}_2$  to methane ( $\text{CH}_4$ ) by a methanator facilitates the quantification of OC and EC using a flame ionization detector (FID). The simultaneous monitoring of optical attenuation (ATN) from a laser source (at 678 nm) determines the split point between OC and EC and facilitates the correction for pyrolyzed carbon. Duplicate analysis of aerosols ( $n = 45$ ) provided the uncertainty on OC and EC measurements to be within  $\pm 3\%$  and  $\pm 7\%$ , respectively [13]. Analytical accuracy in determining total carbon is assessed by analyzing known amount of potassium hydrogen phthalate (KHP) solution ( $n = 16$ ); the average ratio of measured carbon to expected carbon is  $1.05 \pm 0.04$  ( $\text{Av} \pm \text{sd}$ ). Analysis of several field-based samples ( $n = 10$ ), spiked with sucrose, further ascertained the OC-EC split point and provides uncertainty on OC measurements of  $\pm 10\%$  at most. The optical attenuation (ATN, a unitless parameter) of EC at 678 nm can be represented by the following equation:

$$\text{ATN} = \ln \left( \frac{I_0}{I} \right). \quad (2)$$

The attenuation coefficient from EC-OC analyzer ( $b_{\text{ATN-ECOC}}$ ;  $\text{Mm}^{-1}$ ) can be estimated from the ATN signal measured at 678 nm using the following equation:

$$b_{\text{ATN-ECOC}} (\text{Mm}^{-1}) = \text{ATN} \times \left( \frac{A}{V} \right). \quad (3)$$

The terms  $A$  and  $V$  represent the aerosol loaded tisuquartz filter area ( $400 \times 10^{-4} \text{ m}^2$  for present study) and volume of air filtered for each sample collection ( $\text{m}^3$ ), respectively. The attenuation cross section ( $\sigma_{\text{ATN-ECOC}}$ ;  $\text{m}^2 \text{ g}^{-1}$ ) can be directly obtained by correcting the measured ATN signal for shadowing effect [ $R(\text{ATN})$ ; explained later] and dividing by the EC concentration per unit area of the quartz filter ( $\text{EC}_S$  in  $\mu\text{g cm}^{-2}$ ; surface loading of EC) as shown in the following equation:

$$\sigma_{\text{ATN-ECOC}} = \left( \frac{\text{ATN}}{R(\text{ATN}) * \text{EC}_S} \right). \quad (4)$$

The absorption coefficient of EC ( $b_{\text{abs-ECOC}}$ ;  $\text{Mm}^{-1}$ ;  $1 \text{ M} = 10^{-6}$ ) is calculated by the following equation:

$$b_{\text{abs-ECOC}} = \left( \frac{A}{V} * \frac{\text{ATN}}{R(\text{ATN}) * C} \right), \quad (5)$$

where  $C$  and  $R(\text{ATN})$  are the two empirical constants to correct the measured absorption signal for multiple scattering and shadowing effects, respectively. The value of  $R = 1$  and  $C = 2.827$  has been adopted as the correction factor for shadowing and multiple scattering effects for EC, respectively [24, 25].

Furthermore, the mass absorption efficiency of EC (MAE in  $\text{m}^2 \text{ g}^{-1}$ ;  $\sigma_{\text{abs-ECOC}}$ ) is calculated by the following equation:

$$\text{MAE} = \left( \frac{b_{\text{abs}}}{\text{EC} (\mu\text{g m}^{-3})} \right). \quad (6)$$

It is important to state here that (5) and (6) are also applicable for BC, since filter substrate is of quartz fiber. For Aethalometer data, the values of  $R = 1$  and  $C = 2.355, 2.656, 2.677, 2.733, 2.827, 2.933,$  and  $2.925$  have been used for seven wavelengths (370, 470, 520, 590, 660, 880, and 950 nm) [24, 25].

### 3. Results and Discussion

The temporal variability records in the mass concentrations of BC and EC and the BC-to-EC ratio are shown in Figures 2(a) and 2(b). The primary objective of this study is to assess the characteristics of elemental and black carbon (EC and BC) based on their mass absorption efficiency (MAE). This study has been conducted from an upwind site in the Indo-Gangetic Plain. The source characteristics of BC and EC are discussed below.

**3.1. Aethalometer-Based BC.** The average concentrations of BC are 15.4, 8.5, and  $4.2 \mu\text{g m}^{-3}$  during the paddy-residue burning emissions (October–November), bio- and fossil-fuel combustion, and wheat-residue burning emission, respectively. To assess the impact of different emission sources on Aethalometer-based BC at the measurement site, we have utilized a literature based approach [26, 27]. Basically, the method utilizes the percentage difference of BC mass concentrations measured at two different channels [i.e.,  $(\text{BC}_{370} - \text{BC}_{880}) / \text{BC}_{880}$ ]. The positive ratio is indicator for the dominant contribution of biomass burning emissions [26]. Whereas, the negative ratio suggests for the dominant contribution of fossil-fuel combustion sources [27]. In our study, as evident from Figure 2(c), the  $(\text{BC}_{370} - \text{BC}_{880}) / \text{BC}_{880}$  ratio is positive for almost all the data points during the paddy-residue burning emission (October–November) and wheat-residue burning emission (April–May). During wintertime (December–March), this ratio varying between positive and negative indicates for the mixed contribution from fossil-fuel combustion sources and biomass burning emissions to BC mass concentration. A recent study has also estimated the percentage difference of BC mass concentration at two different stations during wintertime in India namely Delhi and Manora peak [28]. Their study reports positive ratio of

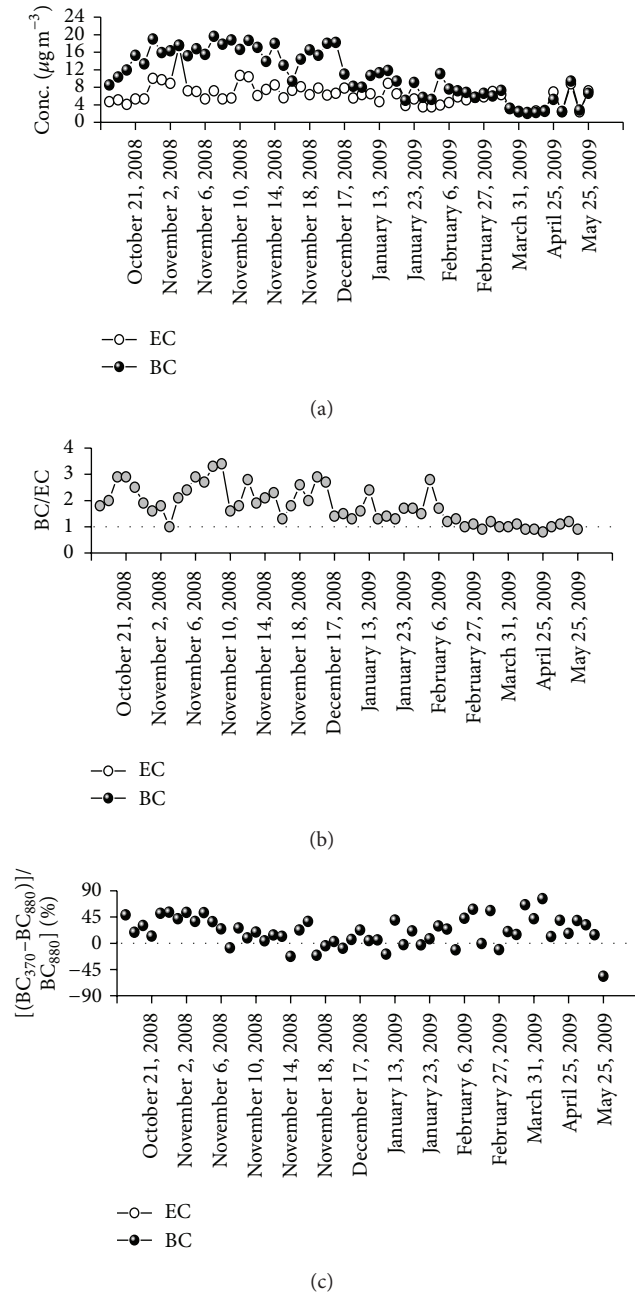


FIGURE 2: Temporal variability in the: (a) mass concentrations of BC and EC; (b) BC-to-EC ratio and; (c) percentage contribution of BC measured at 370 nm and 880 nm for different emissions during the study period from October 2008 to May 2009.

$(BC_{370}-BC_{880})/BC_{880}$  at both the stations during wintertime and attributes to dominant contribution of biomass burning emissions.

The variation of spectral absorption coefficient ( $b_{\text{abs}}$ ) of BC during different emissions is shown in Figure 3. A power law is preferentially used to express the wavelength ( $\lambda$ ) dependence of absorption coefficient ( $b_{\text{abs}}$ ), as follows:

$$b_{\text{abs}} \propto \lambda^{-\alpha}. \quad (7)$$

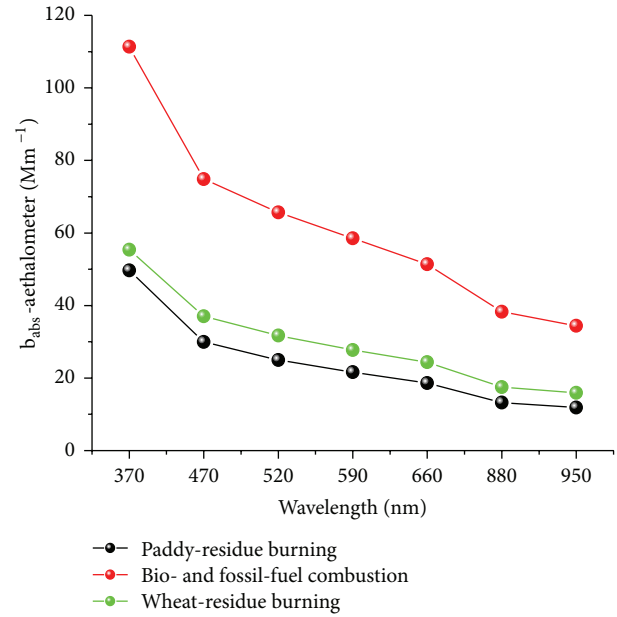


FIGURE 3: The spectral variation of averaged absorption coefficient ( $b_{\text{abs}}$ ) of BC during different emissions in this study.

The Ångström exponent ( $\alpha$ ) is determined empirically using the Aethalometer based  $b_{\text{abs}}$  at multiwavelength (370–950 nm), from the power law (7), serving for comparison with other studies. In this study, the value of  $\alpha$  is found to be 1.52 for paddy-residue burning emission, 1.25 for emissions from bio- and fossil-fuel combustion, and 1.32 from the wheat-residue burning emission in the Indo-Gangetic Plain. This information is hitherto unknown in the literature. In an earlier study [29], the authors report  $\alpha$  value of 1.02 from a downwind location at Kanpur in the IGP. Another study distinguishes aerosol source based on differences in the wavelength dependence in light absorption [30]. The study reports for light absorption varying approximately as  $\lambda^{-1}$  (weak wavelength dependence) by the vehicular aerosols, indicating for BC to be the dominant absorbing component. In contrast, the aerosols from savanna biomass burning were found to have much stronger wavelength dependence, nearly  $\lambda^{-2}$  [30]. Literature based values suggest that  $\alpha$  varies from 1 to 2.9 for BC derived from residential bio-fuel [31]. From our study in the Indo-Gangetic Plain, we document that light absorption by aerosol from postharvest agricultural-waste burning emissions exhibits wavelength dependence of approximately  $\lambda^{-1.5}$ .

**3.2. EC-OC Analyzer Based EC.** The organic carbon (OC) and non-sea-salt potassium ( $\text{nss-K}^+$ , a tracer of the biomass burning emission; Table 1) have been determined to assess diagnostic ratios of OC/EC and  $\text{nss-K}^+/\text{EC}$  in these emissions. The  $\text{K}^+$  concentrations measured in aerosols using Ion-Chromatograph [23] have been corrected for the contribution from sea salts using the  $\text{Na}^+$  tracer method and represented as  $\text{nss-K}^+$  [32]. The  $\text{PM}_{2.5}$  concentrations varied from 110 to  $390 \mu\text{g m}^{-3}$  during October–November during

TABLE 1: Ambient concentration and optical characteristics of black carbon (BC) and elemental carbon (EC) from different emissions in the Indo-Gangetic Plain (IGP).

| Concentration<br>( $\mu\text{g m}^{-3}$ )                      | Paddy-residue burning<br>(October–November; $n = 33$ ) | Bio- and fossil-fuel combustion<br>(December–March; $n = 28$ ) | Wheat-residue burning<br>(April–May; $n = 10$ ) |
|--|--|--|---|
| BC   | 8.5–19.6 ( $15.4 \pm 3.0$ )                            | 2.4–18.2 ( $8.5 \pm 3.9$ )                                     | 2.2–9.4 ( $4.2 \pm 2.7$ )                       |
| EC   | 3.8–17.5 ( $7.3 \pm 2.7$ )                             | 2.3–8.9 ( $5.3 \pm 1.6$ )                                      | 2.0–8.8 ( $3.9 \pm 2.6$ )                       |
| Characteristic ratios [range (Arithmetic average $\pm$ stdev)] |  |  |   |
| OC/EC  | 4.6–25.7 ( $13.0 \pm 4.6$ )                            | 1.9–10.1 ( $5.6 \pm 2.1$ )                                     | 2.5–6.5 ( $4.0 \pm 1.1$ )                       |
| nss- $\text{K}^+$ /EC  | 0.2–2.0 ( $0.8 \pm 0.4$ )                              | 0.1–0.8 ( $0.3 \pm 0.2$ )                                      | 0.2–0.8 ( $0.4 \pm 0.2$ )                       |
| BC/EC  | 1.0–3.4 ( $2.2 \pm 0.6$ )                              | 0.9–2.9 ( $1.6 \pm 0.6$ )                                      | 0.8–1.2 ( $1.0 \pm 0.1$ )                       |
| $b_{\text{abs-AETH}}$ (at 880 nm)                              | 8–18 ( $13 \pm 3$ )                                    | 7–64 ( $27 \pm 17$ )   | 11–28 ( $16 \pm 6$ )                            |
| $b_{\text{abs-ECOC}}$ (corrected for 880 nm)                   | 8–55 ( $15 \pm 9$ )                                    | 8–28 ( $15 \pm 5$ )  | 7–20 ( $13 \pm 5$ )                             |
| $b_{\text{abs-AETH}}/b_{\text{abs-ECOC}}$                      | 0.3–1.6 ( $1.0 \pm 0.3$ )                              | 0.3–5.7 ( $2.0 \pm 1.6$ )                                      | 1.0–1.5 ( $1.2 \pm 0.2$ )                       |

the postharvest paddy-residue burning emissions and 18 to  $123 \mu\text{g m}^{-3}$  during the wheat-residue burning emissions (April–May). The average concentration of OC is  $92 \mu\text{g m}^{-3}$  during the paddy-residue burning emission and  $15 \mu\text{g m}^{-3}$  during the wheat-residue burning emission. The  $\text{PM}_{2.5}$  concentrations varied from 33 to  $220 \mu\text{g m}^{-3}$  and OC varied from 9 to  $58 \mu\text{g m}^{-3}$  during the bio- and fossil-fuel combustion period (December–March). The average concentrations of EC are 7.3, 5.3, and  $3.9 \mu\text{g m}^{-3}$  during October–November, December–March, and April–May, respectively (Table 1). The OC/EC ratio varied from 4.6 to 25.7 (Av: 13.0) during paddy-residue burning emission, 1.9 to 10.1 (Av: 5.6) during bio- and fossil-fuel combustion, and 2.5 to 6.5 (Av: 4.0) for the wheat-residue burning emission. The large temporal variability in the concentrations of particulate species and OC/EC ratio during the first (October–November: paddy-residue burning period) and third emission periods (April–May: wheat-residue burning) is attributable to the difference in the type of two biomass burning emissions and their source strength. Furthermore, the moisture contents in the two biomasses burned are also significantly different: moisture content of paddy-residue is 40–50% and wheat-residue is <5% [13]. However, during December–March, the variability in OC/EC ratio is attributable to varying contributions from bio-fuel burning emission and fossil-fuel combustion sources in the Indo-Gangetic Plain. Furthermore, the nss- $\text{K}^+$ /EC ratio varied from 0.2 to 2.0 (Av: 0.8), 0.1 to 0.8 (Av: 0.3), and 0.2 to 0.8 (Av: 0.4) during these emissions. The  $\text{K}^+$ /EC ratios varying from  $\sim 0.1$  to 0.6 have been reported earlier for characterization of different kinds of biomass burning emissions [33]. In this study, the nss- $\text{K}^+$ /EC average ratio of  $\sim 0.4$ –0.8 is suggested to represent the biomass burning emissions in the Indo-Gangetic Plain.

**3.3. Intercomparison of BC and EC.** The mass concentrations of BC and EC varied from 2.2 to  $19.6 \mu\text{g m}^{-3}$  and from 2.0 to  $17.5 \mu\text{g m}^{-3}$ , respectively, during the entire study period from October 2008 to May 2009. The mass concentrations of BC and EC exhibit near similar trends in seasonal variability with maximum during the paddy-residue burning and minimum during the wheat-residue

burning emission. However, a significant difference in the concentrations of BC and EC measured by two different techniques was observed, in particular, during the paddy-residue burning emission (October–November). The difference between mass concentrations of BC and EC was relatively low (compared to paddy-residue burning) during wintertime (December–March), when emissions from bio-fuel burning and fossil-fuel combustion dominate in the Indo-Gangetic Plain (Table 1). Thus overall, during these two emission scenarios, the BC mass concentrations were always higher than the EC concentrations. In sharp contrast, the mass concentrations of BC and EC were quite similar during the wheat-residue burning period (April–May). The BC-to-EC ratio was  $2.2 \pm 0.6$  during paddy-residue burning period,  $1.6 \pm 0.6$  during emissions from bio-fuel burning and fossil-fuel combustion, and approach to unity ( $1.0 \pm 0.1$ ) during the wheat-residue burning period (Figure 2(b)). An earlier study [34] has suggested that the NIOSH type protocol operated at  $850^\circ\text{C}$  during the OC-EC split could lead to underestimation of EC up to  $\sim 25\%$ . It is noteworthy to mention that even after correcting the measured concentration of EC by 25%, the BC-to-EC ratio becomes  $1.8 \pm 0.5$ ,  $1.2 \pm 0.5$ , and  $0.8 \pm 0.1$  during the aforementioned three consecutive emissions. Thus, the BC/EC ratios conspicuously greater than 1 in particular during paddy-residue burning emissions suggest assessing the contribution of light-absorbing organic aerosols in the IGP.

The scatter plots between BC/EC and OC/EC ratios are shown for different emissions in the IGP (Figures 4(a), 4(b), and 4(c)). During the paddy-residue burning emission (October–November), when OC/EC average ratio is  $13.0 \pm 4.6$  [average OC:  $92 \mu\text{g m}^{-3}$ ; EC:  $7.3 \mu\text{g m}^{-3}$ ], the BC/EC average ratio is  $2.2 \pm 0.6$  ( $R = 0.49$ ;  $P < 0.01$ , Figure 4(a)). During wintertime (December–March), when emission from bio-fuel burning and fossil-fuel combustion is dominant source of carbonaceous aerosols in the IGP, the OC/EC average ratio is  $5.6 \pm 2.1$  [average OC:  $29 \mu\text{g m}^{-3}$ ; EC:  $5.3 \mu\text{g m}^{-3}$ ] and the BC/EC average ratio is  $1.6 \pm 0.6$  ( $R = 0.90$ ;  $P < 0.01$ , Figure 4(b)). However, during the wheat-residue burning period (April–May; Figure 4(c)), when OC/EC average ratio is  $4.0 \pm 1.1$  [average OC:  $15 \mu\text{g m}^{-3}$ ; EC:  $3.9 \mu\text{g m}^{-3}$ ], the BC/EC average ratio is  $1.0 \pm 0.1$  (Table 1). Our investigations

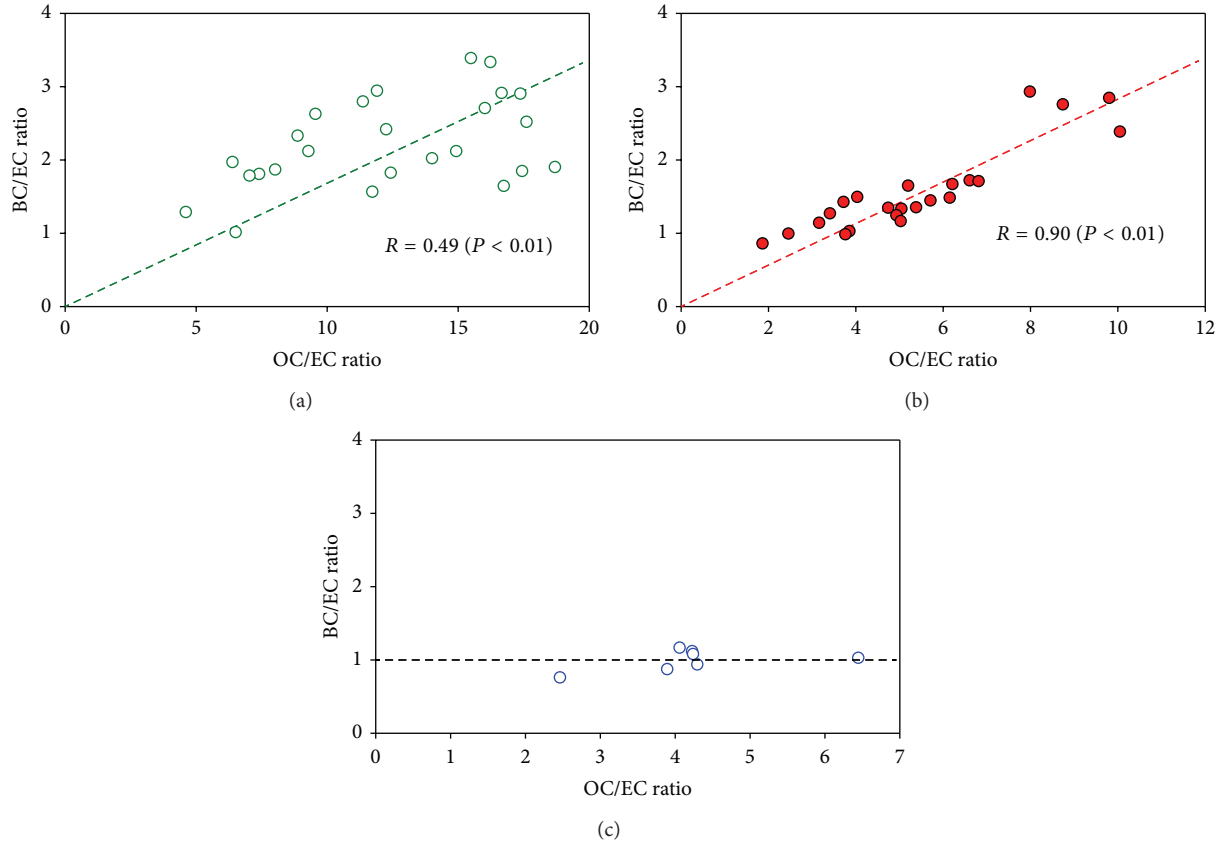


FIGURE 4: Scatter plots between the BC/EC ratio and OC/EC ratio during: (a) paddy-residue burning emission (October–November); (b) biofuel burning emission and fossil-fuel combustion (December–March); and (c) wheat-residue burning emission (April–May).

on comparing the mass concentrations of BC and EC during different emissions in the IGP suggest for relatively large difference between the two, by a factor of 2–3, when the mass concentrations of particulate OC, EC, and OC/EC ratios are relatively high (paddy-residue burning). In contrast, the Aethalometer-based BC and EC-OC analyzer based EC concentrations look quite similar when OC concentrations are less than  $20 \mu\text{g m}^{-3}$  and OC/EC ratio is  $\sim 2$ –4. In future, studies would be required to assess and address to the variability records of light-absorbing organic aerosol species from these large-scale biomass burning emissions in the IGP [2, 30].

The optical attenuation (ATN at 678 nm) from EC-OC analyzer is utilized to determine the attenuation cross section ( $\sigma_{\text{ATN-ECOC}}$ ) during different emissions in the IGP. The scatter plot between the optical attenuation (ATN) and  $\text{EC}_s$  ( $\mu\text{g}/\text{cm}^2$ ) during three different emissions exhibits a linear dependence with significant correlations ( $R \geq 0.74$ ,  $P < 0.01$ ; Figures 5(a), 5(b), and 5(c)). The slope of regression line for different emissions provides the attenuation cross section of EC. Accordingly, the attenuation cross section ( $\sigma_{\text{ATN-ECOC}}$  at 678 nm) values are  $7.2 \pm 0.4 \text{ m}^2 \text{ g}^{-1}$ ;  $8.9 \pm 0.8 \text{ m}^2 \text{ g}^{-1}$ , and  $9.1 \pm 0.7 \text{ m}^2 \text{ g}^{-1}$  for the paddy-residue burning emission (October–November), for emissions from bio-fuel burning and fossil-fuel combustion (December–March) and wheat-residue burning emission (April–May; Figures 5(a), 5(b), and

5(c)). After normalization at 880 nm the  $\sigma_{\text{ATN-ECOC}}$  values are  $4.8 \pm 0.3 \text{ m}^2 \text{ g}^{-1}$ ;  $6.4 \pm 0.6 \text{ m}^2 \text{ g}^{-1}$ ; and  $6.4 \pm 0.5 \text{ m}^2 \text{ g}^{-1}$  for the paddy-residue burning emission (October–November), for emissions from bio-fuel burning and fossil-fuel combustion (December–March) and wheat-residue burning emission (April–May), respectively. It is remarkable that all these values ( $\sigma_{\text{ATN-ECOC}}$ , at 880 nm) are  $\sim 30$ –40% of the attenuation cross section used in Aethalometer for the determination of BC mass concentration.

**3.4. Absorption Coefficient and Mass Absorption Efficiency of EC and BC.** Absorption coefficient of BC ( $b_{\text{abs-AETH}}$ ) as well as EC ( $b_{\text{abs-ECOC}}$ ) is the essential input parameters involved in the direct radiative forcing calculations. It is important to mention that the filter-based absorption technique yields systematic error in the optical attenuation (ATN) [9, 35]. In this context, suggestions from earlier studies to incorporate the corrections due to multiple scattering and shadowing effects have been applied [24, 25]. The  $b_{\text{abs-AETH}}$  (at 880 nm) are ranging from 8–18 ( $13 \pm 3$ )  $\text{Mm}^{-1}$ , 7–64 ( $27 \pm 17$ )  $\text{Mm}^{-1}$ , and 11–28 ( $16 \pm 6$ )  $\text{Mm}^{-1}$  during the paddy-residue burning emission, bio-fuel burning emission and fossil-fuel combustion, and wheat-residue burning emission, respectively (Table 1). The  $b_{\text{abs-ECOC}}$  (at 678 nm) are ranging from 11–82 ( $22 \pm 14$ )  $\text{Mm}^{-1}$ , 12–38 ( $21 \pm 7$ )  $\text{Mm}^{-1}$ , and

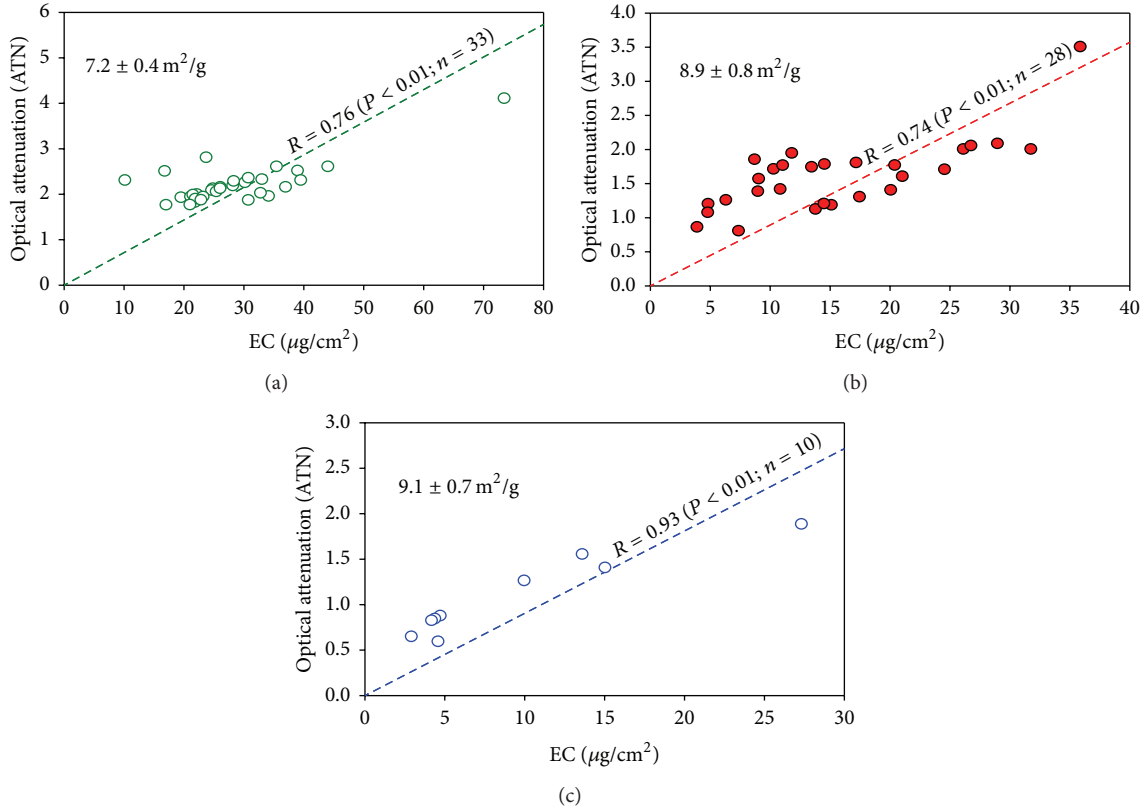


FIGURE 5: Attenuation cross section of EC at 678 nm ( $\sigma_{\text{ATN-ECOC}}$  in  $\text{m}^2 \text{g}^{-1}$ ) during: (a) paddy-residue burning emission (October–November); (b) emissions from biofuel burning and fossil-fuel combustion (December–March); and (c) wheat-residue burning emission (April–May).

9–29 ( $18 \pm 6$ )  $\text{Mm}^{-1}$  during the paddy-residue burning emission (October–November), bio-fuel burning emission and fossil-fuel combustion (December–March), and wheat-residue burning emission (April–May), respectively. Normalized to 880 nm,  $b_{\text{abs-ECOC}}$  (at 880 nm) are ranging from 8–55 ( $15 \pm 9$ )  $\text{Mm}^{-1}$ , 8–28 ( $15 \pm 5$ )  $\text{Mm}^{-1}$ , and 7–20 ( $13 \pm 5$ )  $\text{Mm}^{-1}$  during the paddy-residue burning emission, bio-fuel burning emission and fossil-fuel combustion, and wheat-residue burning emission, respectively. Relatively high values of  $b_{\text{abs-ECOC}}$  (as high as  $55 \text{Mm}^{-1}$ ) during the paddy-residue burning emission (during October–November) indicate the high light absorption characteristics of EC in the ambient air during this period as compared to those during the other emissions, assessed in this study (wheat-residue burning during April–May and bio- and fossil-fuel combustion during December–March). The average ratio of  $b_{\text{abs-AETH}}/b_{\text{abs-ECOC}}$  (at 880 nm) for the postharvest paddy- and wheat-residue burning emissions is close to 1. In sharp contrast, this ratio is  $\sim 2$  for emissions from bio- and fossil-fuel combustion in the IGP. The Aethalometer based mass absorption efficiency (MAE) of BC (at 880 nm) is  $0.9 \pm 0.1 \text{m}^2 \text{g}^{-1}$ ,  $3.5 \pm 2.2 \text{m}^2 \text{g}^{-1}$ , and  $4.4 \pm 1.3 \text{m}^2 \text{g}^{-1}$  during paddy-residue burning emission, bio-fuel burning emission and fossil-fuel combustion, and wheat-residue burning emission. The MAE (at 678 nm) of EC has been determined by the linear regression analysis between absorption coefficients ( $b_{\text{abs}}$ ;  $\text{Mm}^{-1}$ ) and EC mass

concentration ( $\mu\text{g m}^{-3}$ ). The slope of regression line gives the MAE for different emissions impacting the sampling site. Accordingly, the MAE of EC (at 678 nm) are  $3.0 \pm 0.8 \text{m}^2 \text{g}^{-1}$  ( $R = 0.57, P < 0.01$ ),  $3.8 \pm 0.8 \text{m}^2 \text{g}^{-1}$  ( $R = 0.78, P < 0.01$ ), and  $4.1 \pm 0.4 \text{m}^2 \text{g}^{-1}$  ( $R = 0.93, P < 0.01$ ) during paddy-residue burning emission (October–November), bio-fuel burning emission and fossil-fuel combustion (December–March), and wheat-residue burning emission (April–May). Normalizing to 880 nm, the MAE of EC (at 880 nm) are  $2.0 \pm 0.5 \text{m}^2 \text{g}^{-1}$  ( $R = 0.57, P < 0.01$ ),  $2.7 \pm 0.6 \text{m}^2 \text{g}^{-1}$  ( $R = 0.78, P < 0.01$ ), and  $2.9 \pm 0.3 \text{m}^2 \text{g}^{-1}$  ( $R = 0.93, P < 0.01$ ) during paddy-residue burning emission, bio-fuel burning emission and fossil-fuel combustion, and wheat-residue burning emission (Figure 6). The literature based values on MAE of EC suggest for a wide range, varying from 2 to  $25 \text{m}^2 \text{g}^{-1}$ , depending on its emission source and mixing state of EC [9, 18, 36, 37]. For example, [18] has reported a value of  $7.5 \pm 1.2 \text{m}^2 \text{g}^{-1}$  (at 550 nm), for the uncoated soot particles. Furthermore, the freshly emitted particles coexist as external mixture of light scattering and absorbing (EC) components [38, 39]. Subsequently, during the course of transport away from its emission source, these aerosols undergo internal mixing. Towards this, the global simulation models suggest that in  $\sim 1$ –5 days, the EC can be internally mixed with other aerosols [3]. After mixing, the physicochemical characteristics of pure EC will no longer be retained, due to the coating of other aerosols such as sulfate

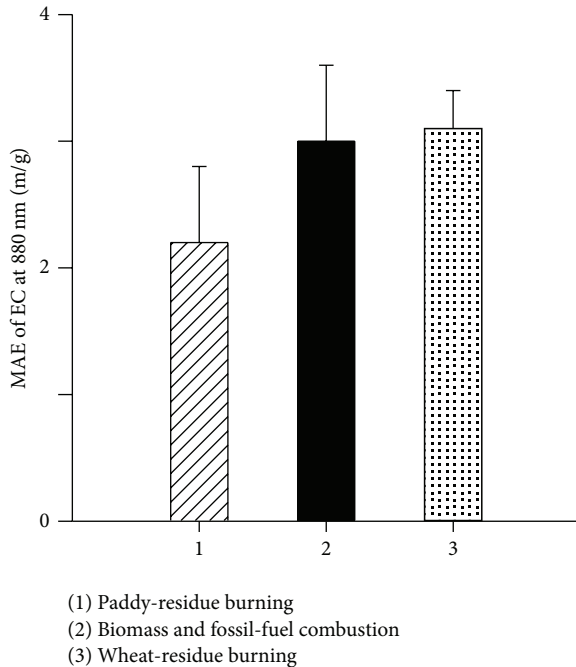


FIGURE 6: Mass absorption efficiency (MAE;  $\text{m}^2 \text{g}^{-1}$ ) of EC at 880 nm during different emissions in Northern India.

and organics. The MAE of coated-EC has been reported to be relatively high as compared to that for the uncoated EC [40]. The plausible mechanism for enhancement in the MAE of EC due to coating is widely referred to as the lensing effect, focusing the light into core of EC. In this study, we report the MAE of EC (at 880 nm) from two distinct postharvest biomass burning emissions (paddy-residue burning:  $2.0 \pm 0.5 \text{ m}^2 \text{g}^{-1}$ ; wheat-residue burning:  $2.9 \pm 0.3 \text{ m}^2 \text{g}^{-1}$ ) and during the emissions from bio- and fossil-fuel combustion (MAE:  $2.7 \pm 0.6 \text{ m}^2 \text{g}^{-1}$ ; December–March). A near similar MAE of EC varying from  $3.0$  to  $6.8 \text{ m}^2 \text{g}^{-1}$  at 632 nm from biomass burning emissions had also been reported earlier [41]. In contrast, the MAE from diesel exhaust has been found relatively high (Av:  $8.4 \text{ m}^2 \text{g}^{-1}$ ) [41]. Thus, the MAE of EC centering at  $2.7 \text{ m}^2 \text{g}^{-1}$  during December–March period suggests that biomass burning emission is the dominant source of EC. However, future studies are needed in order to assess the impact of mixing state on the MAE of BC and EC in the Indo-Gangetic Plain.

#### 4. Summary

This study has been carried out from October 2008 to May 2009 at Patiala, an upwind location in the Indo-Gangetic Plain (Northern India). The important conclusions drawn from this study are as follows.

- (1) The OC/EC ratio varying from 4.6 to 25.7 (Av  $\pm$  sd:  $13.0 \pm 4.6$ ) and nss- $\text{K}^+$ /EC ratio varying from 0.2 to 2.0 ( $0.8 \pm 0.4$ ) have been recorded from the postharvest paddy-residue burning emission (October–November). In contrast, during the

postharvest wheat-residue burning emission during April–May, the OC/EC ratio varied from 2.5 to 6.5 (Av  $\pm$  sd:  $4.0 \pm 1.1$ ) and nss- $\text{K}^+$ /EC ratio varied from 0.2 to 0.8 ( $0.4 \pm 0.2$ ). Furthermore, the inference on dominance of biomass burning emissions during the period from December to March has been made, using the nss- $\text{K}^+$ /EC ratio (chemical tracer) of  $0.3 \pm 0.2$  (range: 0.1–0.8) in conjunction with the OC/EC ratio of  $5.6 \pm 2.1$  (range: 1.9–10.1).

- (2) Overall, the BC mass concentrations varied from 2 to  $20 \mu\text{g m}^{-3}$ , and the EC concentrations varied from 2 to  $18 \mu\text{g m}^{-3}$ . The BC/EC ratios are significantly higher ( $2.2 \pm 0.6$ ) during the postharvest paddy-residue burning emission (October–November), decrease to  $1.6 \pm 0.6$  during emissions from bio-fuel burning and fossil-fuel combustion (December–March) and  $1.0 \pm 0.1$  during the wheat-residue burning emission (April–May).
- (3) The BC/EC ratios conspicuously greater than 1 have been observed during paddy-residue burning emission (October–November), associated with high abundance of EC, OC, and OC/EC ratio. This suggests assessing the contribution of light-absorbing organic aerosol species.
- (4) The light absorption by aerosol from postharvest agricultural-waste (paddy- and wheat-residue) burning emissions exhibits wavelength dependence of approximately  $\lambda^{-1.5}$ .
- (5) The attenuation cross section ( $\sigma_{\text{ATN-ECOC}}$ ) inferred from EC-OC analyzer at 880 nm is  $\sim 30$ – $40\%$  lower than that used in the Aethalometer.
- (6) The mass absorption efficiency (MAE;  $\sigma_{\text{abs}}$ ) of EC at 880 nm is  $2.0 \pm 0.6 \text{ m}^2 \text{g}^{-1}$ ,  $2.7 \pm 0.6 \text{ m}^2 \text{g}^{-1}$ , and  $2.9 \pm 0.3 \text{ m}^2 \text{g}^{-1}$  during paddy-residue burning, emissions from bio-fuel burning and fossil-fuel combustion, and wheat-residue burning emission, respectively.

#### Conflict of Interests

The authors declare that there is no conflict of interests regarding the publication of this paper.

#### Acknowledgments

This work is financially supported by ISRO-Geosphere Biosphere Program (Bengaluru, India). The authors thank the anonymous reviewers for their constructive comments and suggestions and Dr. Lucas Alados-Arboledas for the Editorial handling of this paper.

#### References

- [1] A. Petzold, J. A. Ogren, M. Fiebig et al., “Recommendations for the interpretation of “black carbon” measurements,” *Atmospheric Chemistry and Physics*, vol. 13, pp. 8365–8379, 2013.
- [2] M. O. Andreae and A. Gelencsér, “Black carbon or brown carbon? The nature of light-absorbing carbonaceous aerosols,”

- Atmospheric Chemistry and Physics*, vol. 6, no. 10, pp. 3131–3148, 2006.
- [3] M. Z. Jacobson, “Strong radiative heating due to the mixing state of black carbon in atmospheric aerosols,” *Nature*, vol. 409, no. 6821, pp. 695–697, 2001.
  - [4] S. Solomon, D. Qin, M. Manning et al., Eds., *Climate Change 2007: The Physical Science Basis. Contribution of Working Group I to the Fourth Assessment Report of the Intergovernmental Panel on Climate Change*, Cambridge University Press, Cambridge, UK, 2007.
  - [5] C. Wang, D. Kim, A. M. L. Ekman, M. C. Barth, and P. J. Rasch, “Impact of anthropogenic aerosols on Indian summer monsoon,” *Geophysical Research Letters*, vol. 36, no. 21, Article ID L21704, 2009.
  - [6] W. K. M. Lau, M.-K. Kim, K.-M. Kim, and W.-S. Lee, “Enhanced surface warming and accelerated snow melt in the Himalayas and Tibetan Plateau induced by absorbing aerosols,” *Environmental Research Letters*, vol. 5, no. 2, Article ID 025204, pp. 1–10, 2010.
  - [7] M. V. Ramana, V. Ramanathan, Y. Feng et al., “Warming influenced by the ratio of black carbon to sulphate and the black-carbon source,” *Nature Geoscience*, vol. 3, no. 8, pp. 542–545, 2010.
  - [8] D. C. Snyder and J. J. Schauer, “An inter-comparison of two black carbon aerosol instruments and a semi-continuous elemental carbon instrument in the urban environment,” *Aerosol Science and Technology*, vol. 41, no. 5, pp. 463–474, 2007.
  - [9] C. Liousse, H. Cachier, and S. G. Jennings, “Optical and thermal measurements of black carbon aerosol content in different environments: variation of the specific attenuation cross-section, sigma ( $\sigma$ ),” *Atmospheric Environment A*, vol. 27, no. 8, pp. 1203–1211, 1993.
  - [10] K. Ram, M. M. Sarin, and S. N. Tripathi, “Inter-comparison of thermal and optical methods for determination of atmospheric black carbon and attenuation coefficient from an urban location in northern India,” *Atmospheric Research*, vol. 97, no. 3, pp. 335–342, 2010.
  - [11] K. Ram and M. M. Sarin, “Absorption coefficient and site-specific mass absorption efficiency of elemental carbon in aerosols over urban, rural, and high-altitude sites in India,” *Environmental Science and Technology*, vol. 43, no. 21, pp. 8233–8239, 2009.
  - [12] K. V. S. Badarinath, T. R. K. Chand, and V. K. Prasad, “Agriculture crop residue burning in the Indo-Gangetic Plains—a study using IRS-P6 AWiFS satellite data,” *Current Science*, vol. 91, no. 8, pp. 1085–1089, 2006.
  - [13] P. Rajput, M. M. Sarin, R. Rengarajan, and D. Singh, “Atmospheric polycyclic aromatic hydrocarbons (PAHs) from post-harvest biomass burning emissions in the Indo-Gangetic Plain: isomer ratios and temporal trends,” *Atmospheric Environment*, vol. 45, no. 37, pp. 6732–6740, 2011.
  - [14] D. Sharma, D. Singh, and D. Sumit, “Case studies of black carbon aerosol characteristics during agriculture crop residue burning period over Patiala, Punjab, India using the synergy of ground based and satellite observations,” *International Journal of Geology, Earth and Environmental Sciences*, vol. 2, no. 2, pp. 315–326, 2012.
  - [15] P. Rajput, M. M. Sarin, D. Sharma, and D. Singh, “Characteristics and emission budget of carbonaceous species from post-harvest agricultural-waste burning in source region of the Indo-Gangetic Plain,” *Tellus B*, vol. 66, Article ID 21026, 2014.
  - [16] P. Rajput and M. M. Sarin, “Polar and non-polar organic aerosols from large-scale agricultural-waste burning emissions in Northern India: implications to organic mass-to-organic carbon ratio,” *Chemosphere*, 2013.
  - [17] A. D. A. Hansen, *The Aethalometer Manual*, Magee Scientific, Berkeley, Calif, USA, 2005.
  - [18] T. C. Bond and R. W. Bergstrom, “Light absorption by carbonaceous particles: an investigative review,” *Aerosol Science and Technology*, vol. 40, no. 1, pp. 27–67, 2006.
  - [19] A. D. A. Hansen, V. N. Kapustin, V. M. Kopeikin, D. A. Gillette, and B. A. Bodhaine, “Optical absorption by aerosol black carbon and dust in a desert region of Central Asia,” *Atmospheric Environment A*, vol. 27, no. 16, pp. 2527–2531, 1993.
  - [20] A. D. A. Hansen, H. Rosen, and T. Novakov, “The aethalometer—an instrument for the real-time measurement of optical absorption by aerosol particles,” *Science of the Total Environment*, vol. 36, pp. 191–196, 1984.
  - [21] A. D. A. Hansen, *Magee Scientific Aethalometer User’s Guide*, Magee Scientific, Berkeley, Calif, USA, 1996.
  - [22] M. E. Birch and R. A. Cary, “Elemental carbon-based method for monitoring occupational exposures to particulate diesel exhaust,” *Aerosol Science and Technology*, vol. 25, no. 3, pp. 221–241, 1996.
  - [23] R. Rengarajan, M. M. Sarin, and A. K. Sudheer, “Carbonaceous and inorganic species in atmospheric aerosols during winter-time over urban and high-altitude sites in North India,” *Journal of Geophysical Research: Atmospheres*, vol. 112, no. D21, Article ID D21307, 2007.
  - [24] P. R. Sinha, R. K. Manchanda, D. G. Kaskaoutis, Y. B. Kumar, and S. Sreenivasan, “Seasonal variation of surface and vertical profile of aerosol properties over a tropical urban station Hyderabad, India,” *Journal of Geophysical Research: Atmospheres*, vol. 118, no. 2, pp. 749–768, 2013.
  - [25] O. Schmid, P. Artaxo, W. P. Arnott et al., “Spectral light absorption by ambient aerosols influenced by biomass burning in the Amazon Basin. I: comparison and field calibration of absorption measurement techniques,” *Atmospheric Chemistry and Physics*, vol. 6, no. 11, pp. 3443–3462, 2006.
  - [26] M. Wang, S. Ghan, M. Ovchinnikov et al., “Aerosol indirect effects in a multi-scale aerosol-climate model PNNL-MMF,” *Atmospheric Chemistry and Physics*, vol. 11, no. 11, pp. 5431–5455, 2011.
  - [27] H. Herich, C. Hueglin, and B. Buchmann, “A 2.5 year’s source apportionment study of black carbon from wood burning and fossil fuel combustion at urban and rural sites in Switzerland,” *Atmospheric Measurement Techniques*, vol. 4, no. 7, pp. 1409–1420, 2011.
  - [28] A. K. Srivastava, K. Ram, P. Pant, P. Hegde, and H. Joshi, “Black carbon aerosols over Manora Peak in the Indian Himalayan foothills: implications for climate forcing,” *Environmental Research Letters*, vol. 7, no. 1, Article ID 014002, 2012.
  - [29] S. Dey and S. N. Tripathi, “Estimation of aerosol optical properties and radiative effects in the Ganga basin, northern India, during the wintertime,” *Journal of Geophysical Research: Atmospheres*, vol. 112, no. D3, Article ID D03203, 2007.
  - [30] T. W. Kirchstetter, T. Novakov, and P. V. Hobbs, “Evidence that the spectral dependence of light absorption by aerosols is affected by organic carbon,” *Journal of Geophysical Research: Atmospheres*, vol. 109, no. D21, Article ID D21208, 2004.
  - [31] T. C. Bond, “Spectral dependence of visible light absorption by carbonaceous particles emitted from coal combustion,”

- Geophysical Research Letters*, vol. 28, no. 21, pp. 4075–4078, 2001.
- [32] W. C. Keene, A. A. P. Pszenny, J. N. Galloway, and M. E. Hawley, “Sea-salt corrections and interpretation of constituent ratios in marine precipitation,” *Journal of Geophysical Research: Atmospheres*, vol. 91, no. D6, pp. 6647–6658, 1986.
- [33] M. O. Andreae and P. Merlet, “Emission of trace gases and aerosols from biomass burning,” *Global Biogeochemical Cycles*, vol. 15, no. 4, pp. 955–966, 2001.
- [34] F. Cavalli, M. Viana, K. E. Yttri, J. Genberg, and J.-P. Putaud, “Toward a standardised thermal-optical protocol for measuring atmospheric organic and elemental carbon: the EUSAAR protocol,” *Atmospheric Measurement Techniques*, vol. 3, no. 1, pp. 79–89, 2010.
- [35] A. Petzold, C. Kopp, and R. Niessner, “The dependence of the specific attenuation cross-section on black carbon mass fraction and particle size,” *Atmospheric Environment*, vol. 31, no. 5, pp. 661–672, 1997.
- [36] S. Sharma, J. R. Brook, H. Cachier, J. Chow, A. Gaudenzi, and G. Lu, “Light absorption and thermal measurements of black carbon in different regions of Canada,” *Journal of Geophysical Research: Atmospheres*, vol. 107, no. D24, p. 4771, 2002.
- [37] J. P. Schwarz, R. S. Gao, J. R. Spackman et al., “Measurement of the mixing state, mass, and optical size of individual black carbon particles in urban and biomass burning emissions,” *Geophysical Research Letters*, vol. 35, no. 13, Article ID L13810, 2008.
- [38] M. Pósfai, R. Simonics, J. Li, P. V. Hobbs, and P. R. Buseck, “Individual aerosol particles from biomass burning in southern Africa: 1. Compositions and size distributions of carbonaceous particles,” *Journal of Geophysical Research: Atmospheres*, vol. 108, no. D13, pp. 1–19, 2003.
- [39] M. Mallet, J. C. Roger, S. Despiou, P. Putaud, and O. Dubovik, “A study of the mixing state of black carbon in urban zone,” *Journal of Geophysical Research: Atmospheres*, vol. 109, no. D4, Article ID D04202, 2004.
- [40] R. W. Bergstrom, T. P. Ackerman, and L. W. Richards, “The optical properties of particulate elemental carbon,” in *Particulate Carbon: Atmospheric Life Cycle*, G. T. Wolff and R. L. Klimsch, Eds., Plenum Press, New York, NY, USA, 1982.
- [41] Y. Cheng, K.-B. He, M. Zheng et al., “Mass absorption efficiency of elemental carbon and water-soluble organic carbon in Beijing, China,” *Atmospheric Chemistry and Physics*, vol. 11, no. 22, pp. 11497–11510, 2011.

## Review Article

# Annual Patterns of Atmospheric Pollutions and Episodes over Cairo Egypt

**Y. Aboel Fetouh,<sup>1</sup> H. El Askary,<sup>2,3,4</sup> M. El Raey,<sup>1</sup> M. Allali,<sup>5</sup> W. A. Sprigg,<sup>3</sup> and M. Kafatos<sup>2</sup>**

<sup>1</sup> *Institute of Graduate Studies and Research (IGSR), Alexandria University, Alexandria, Egypt*

<sup>2</sup> *Center for Excellence in Earth Observing, Schmid College of Science and Technology, Chapman University, Orange, CA, USA*

<sup>3</sup> *School of Earth and Environmental Sciences, Schmid College of Science and Technology, Chapman University, Orange, CA 92866, USA*

<sup>4</sup> *Department of Environmental Sciences, Faculty of Science, Alexandria University, Moharem Bek, Alexandria 21522, Egypt*

<sup>5</sup> *School of Computational Sciences, Schmid College of Science and Technology, Chapman University, Orange, CA 92866, USA*

Correspondence should be addressed to H. El Askary; [elaskary@chapman.edu](mailto:elaskary@chapman.edu)

Received 28 March 2013; Revised 13 July 2013; Accepted 18 July 2013

Academic Editor: S. K. Satheesh

Copyright © 2013 Y. Aboel Fetouh et al. This is an open access article distributed under the Creative Commons Attribution License, which permits unrestricted use, distribution, and reproduction in any medium, provided the original work is properly cited.

The Nile Delta major cities, particularly Cairo, experienced stagnant air pollution episodes, known as Black Cloud, every year over the past decade during autumn. Low-elevated thermal inversion layers play a crucial role in intensifying pollution impacts. Carbon monoxide, ozone, atmospheric temperature, water vapor, and methane measurements from the tropospheric emission spectrometer (TES) on board the Aura have been used to assess the dominant component below the inversion layer. In this study, time series analysis, autocorrelations, and cross correlations are performed to gain a better understanding of the connections between those parameters and their local effect. Satellite-based data were obtained for the years 2005–2010. The parameters mentioned were investigated throughout the whole year in order to study the possible episodes that take place in addition to their change from year to year. Ozone and carbon monoxide were the two major indicators to the most basic episodes that occur over Cairo and the Delta region.

## 1. Introduction

Identifying the origin (natural versus anthropogenic) and dynamics of aerosols over different regions at varying temporal and spatial scales will provide more knowledge on impacts of aerosols on the regional climate and the ultimate connections to the Earth's global climate system [1]. Over the last decade, aerosols have been studied quantitatively regionally and globally using satellite remote sensing and modeling. Such studies proved to be very useful in climate studies [2, 3]. The Mediterranean basin aerosols originate from a variety of sources, which are either natural (sea salts, desert dust) or anthropogenic (local sources) due to the increasing urbanization and industrialization, as well as long-range transport [4–6]. At regional scale, the Mediterranean is exposed to air pollution with levels exceeding the typical air-quality standards. This is particularly true for the Delta region, being at the crossroads of different aerosol species

originating from local urban-industrial and biomass-burning activities, regional dust sources, and European pollution from the north [7–9].

Over the past decade Cairo, Egypt, located at a longitude of 31°13 and latitude of 30.2°, the largest city of Africa and one of the world's megacities with a population of more than 20 million people and more than one third of the national industry, has been suffering from major air pollution problems. Cairo and the Greater Delta region have recorded much higher air pollution episodes as compared to the past few decades. As a result, it is also one of the most air-polluted megacities in the world [10]. This is a normal consequence of Egypt's accelerated economic growth over the past three decades. A growing population has increased the polluting human activities that include fuel combustion, and polluting factories such as in the cement industry that tries to keep up with the needs of the growing population. In addition to the city's economic growth, Cairo's location,

topography, and complex climate systems play vital roles in the presence of these episodes [11–13]. Its location subjects it to blown sand and dust from the western desert (since Egypt is 90% desert), air pollutants transported from Europe, emissions of atmospheric constituents from Africa, and the effect of trade winds that diminish over the Mediterranean during the Black Cloud episodes. It is thought that “black cloud” pollution episodes occur only over Cairo and are due to local emissions. However, it was found that emissions from the surrounding cities and regions are contributing to Cairo’s pollution [14]. The low topography of Cairo, bounded by Giza (western highlands) and Mokattam (eastern highlands), confines the pollutants and suppresses the motion of suspended particulates, especially in September through November when wind currents are weak [15]. Hence, wind patterns and humidity influence the behavior of air pollutants and must be considered [12].

Aerosol sources, types, and trajectories over the Nile Delta are complex and so is its meteorology. The worst air quality conditions over Cairo and its environs occur in the fall season [12, 16]. This high-pollution season is locally referred to as the “black cloud” phenomenon, during which the region suffers from high ambient concentrations of atmospheric pollutants including particulates (PM), carbon monoxide, nitrogen oxides, ozone, and sulfur dioxide [17–20]. During winter, the climate is generally cold and rainy while hot and dry in the summer; hence, the city witnesses significant climatological impacts on the public health [21]. On the other hand, Alexandria, a Mediterranean city, has a more appealing climate but is the largest industrial city, with ~55% of the total Egyptian industry. Alexandria suffers from pollution episodes, which are, however, still not as intense as those usually observed over Cairo. It was revealed that Cairo’s and Alexandria’s aerosols include “background pollution,” “pollution-like,” and “dust-like” components [19, 20]. Generally speaking, Egypt is influenced by the regional-scale trade wind system which is enhanced during the warm season and results in winds over Egypt from the North supported by sea breezes along the Mediterranean coastline [5, 6, 20]. During autumn, aerosols originating from biomass burning from agricultural fields within the Nile Delta add to the area’s anthropogenic aerosols and to bigger pollution events.

The published literature attributes the increased pollution levels over Cairo and the Nile Delta region during the black cloud season to emissions from biomass or open burning of agricultural waste and from vehicles, industries, and formation of secondary aerosols [12, 13, 16–19, 22–28]. Major contributors to PM<sub>10</sub> over Cairo include, mobile source emissions, and open burning, while the PM<sub>2.5</sub> tended to be dominated by mobile source emission, open burning, and secondary species [18]. Such episodes of pollution over densely populated cities such as Cairo severely impact public health [21], with potential adverse consequences, not only for the residents but also for the millions of visitors that tour this region annually, particularly from Europe, North America, and Japan. Identifying correct sources of aerosols is important not only for public health reasons but also for assessing their effect on the regional climate.

It is noteworthy that transport processes on a seasonal scale in the African upper troposphere are driven by Hadley meridional circulation which is strong during winter. In the summer, the pollutant transport is from the east, a result of the Asian monsoon anticyclone in April and May. During Africa’s Northern Hemisphere monsoon season, ozone precursors generated from biomass burning in the south are transported to the Intertropical Convergence Zone and they change the composition of Africa’s upper troposphere [29]. Smoke or air pollution concentrations are the highest with low wind speeds, low vertical turbulence, temperature inversions, and high humidity [30]. Therefore, it can be seen that the North African/East Mediterranean troposphere is a crossroad to various transport processes both on regional and intercontinental scales. A study on this pollution crossroad showed that pollution generated by Asia can be transported towards Africa by the anticyclone flow of the Asian summer monsoon [29].

## 2. Data and Methodology

Monitoring by new tropospheric satellite sensors is playing an increasingly important role in explaining chemistry and transport processes in the lower atmosphere [31]. Data from the Tropospheric Emission Spectroradiometer (TES) aboard the NASA satellite Aura, have been used in scientific analysis since 2006. The TES was found to be unique in providing multiyear coincident tropospheric profiles of CO, O<sub>3</sub>, and H<sub>2</sub>O. TES retrievals of ozone, temperature, and water vapor were compared to model fields from Global Modeling and Assimilation Office (GMAO). Temperature retrievals from the Atmospheric Infrared Sounder (AIRS), tropospheric ozone columns from Goddard Earth Observing System (GEOS), and ozone retrievals from Total Ozone Monitoring System (TOMS) were also compared and the results showed no biases [32]. In 2007, TES nadir observations were compared with nearly coincident spectral radiance measurements from AIRS on Aqua, and special scanning high-resolution interferometer sounder (SHIS) positively validated these TES measurements [33]. TES data have also been used in studying the effect of the 2006 El Niño over Indonesia [34, 35]. The Atmospheric Chemistry Experiment (ACE) measurements were used, and it was found that the vertical profiles agree with those from the TES [34]. TES transect observations were applied in addition to the TES standard products to study low tropospheric ammonia and methanol over and near Beijing in northeast China [36]. This was the first time that these molecules were detected in space-based nadir viewing measurements penetrating in the lower atmosphere. Ozone concentrations from TES were used to examine the migration of high ozone over the western North Atlantic [37].

The objective of this paper is to report the results of a study investigating satellite-based TES observations of indicators contributing to air pollution episodes in Cairo, Egypt. TES and the Aura satellite are part of the Earth Observing System (EOS), a coordinated series of polar-orbiting and low-inclination satellites [37]. Aura, launched on July 15, 2004, was designed to record lower stratosphere and

upper troposphere compositions to study the atmosphere's chemistry and dynamics [38]. Data from the Aura mission are useful when studying ozone trends, air quality, and links to climate change [39]. The TES, an infrared, high-resolution, Fourier Transform spectrometer with a spectral range of 650–3050  $\text{cm}^{-1}$  (3.3–15.4  $\mu$ ) and a spatial resolution of 0.1  $\text{cm}^{-1}$  nadir viewing and 0.025  $\text{cm}^{-1}$  limb, is designed to measure the global, vertical distribution of tropospheric ozone and its precursors, such as carbon monoxide, with high precision [34]. In cloud-free conditions, the vertical resolution of TES nadir ozone estimates is about 6 km with sensitivity to both the lower and upper tropospheres [40].

The TES parameters considered in this study are atmospheric temperature (TATM), ozone ( $\text{O}_3$ ), carbon monoxide (CO), methane ( $\text{CH}_4$ ), and water vapor ( $\text{H}_2\text{O}$ ). CO and ozone are two pollutants used by the US Environmental Protection Agency (EPA) to monitor air quality and are measured globally and simultaneously by the TES instrument [34]. TES data for CO, methane, ozone, atmospheric temperature, and water vapor were collected for study from 2005 to 2010 using the Giovanni website. These unique data sets of vertical estimates of ozone and the key signature of pollution, carbon monoxide are available from TES. Vertical profiles can help in unraveling the processes that have a role in the redistribution of ozone [41]. A time series is first done to see when the highest values of CO, ozone, and methane occur. Data for these specific days corresponding to the high values are then presented in vertical profiles. Units for the values below are in volume mixing ratio (VMR).

### 3. TES Data Analysis

**3.1. Vertical Profiles.** The vertical distribution of ozone is crucial in Earth's atmosphere since the ozone filters out biodamaging ultraviolet (UV) light (wavelength  $<280$  nm) in the stratosphere, acts as a greenhouse gas in the upper troposphere, regulates the oxidation capacity of the lower atmosphere, and affects the air quality for humans and vegetation near the Earth's surface [42]. On the other hand, atmospheric carbon monoxide (CO) distributions are controlled by anthropogenic emissions, biomass burning, transport, and oxidation by reaction with the hydroxyl radical (OH). Hence, vertical profile distributions of CO are important for understanding changes related to all of these contributions [43]. Figure 1 shows three graphs for the five parameters during the summer June-July season during 3 different years 2005, 2006, and 2007.

In Figure 1, the gradient of atmospheric temperature is small. Ozone increases with altitude, perhaps an indication of abnormal conditions or the presence of abrupt temperature changes. In short, there is an absence of the "normal" situation during the summer season. Vertical Profiles for chosen dates, during the Black Cloud episode (October-November), are shown in Figure 2.

During the black cloud episode, CO levels indicate the presence of pollution. Levels of CO were also high in the dust season, March through April. The presence of methane, water vapor, and other greenhouse gases such as carbon

dioxide in the Cairo atmosphere heat, the air creates an inversion aloft and conspire to trap pollutants below. Aerosols were found to peak during March and June due to mineral dust, part of the mix transported into Cairo [27] from the Sahara desert.

It is clear from this evidence that meteorological factors, coinciding with Cairo's pollution and heat-island conditions make the analysis a complicated process. However, the available literature leads us into profitable directions: increase in Ozone during the summer is mostly a result of trans-boundary transport from Europe [44]; carbon monoxide increases are a result of pollution and the effect of Sahara cyclones (Khamsin) or the Saharan depression that increases dust and aerosols during the same time period [16].

**3.2. CO and Ozone Time Series.** Figures 3 and 4 show the trend of ozone and carbon monoxide levels at four different pressure levels: 100 hPa, 908 hPa, 825 hPa, and 749 hPa over the year 2007.

Many peaks can be observed throughout the year. Oscillations are clear during February, July-August, and October-November. Ozone is at its highest levels during the summer season. This is mainly attributed to long range transport from Europe [44]. Recent studies in 3D atmospheric chemistry and transport models suggest that the photochemical ozone formation from biomass burning may be less important than it was indicated in previous studies and that biomass burning may not be the main cause for an increase in tropospheric ozone [45, 46].

Studying the tropospheric ozone using aerosol index and tropospheric column ozone (TCO) time series, a TCO peak was noted over North Africa in the September through November time period and a minimum during early spring (February and March) [45, 46]. It was found that the photochemical smog occurs during the summer season and VOCs play an important role in the formation of ground level ozone, photochemical oxidants, and smog episodes [47]. In our case, October-November period in Egypt represents the black cloud season when the burning of rice straw increases Cairo's pollution; however, a high aerosol peak is found during March 2007 at the pressure level of 825 hPa.

Pollution peaks are clearly present in February, March, and April, 2007, reaching as high as 2.08E-7 vmr in March. Oscillations in concentration occurred throughout 2007 and were typical in 2006 as well (not shown here). High levels of carbon monoxide in March and April coincide with the presence of the dust season or Khamsin coming from the western desert. The high levels appearing during October and December of 2007 could be a cause of the Black Cloud episode.

Using trajectory analysis and satellite observations from MOPITT CO over the East/Japan Sea (level 2 data with 10% precision for April 2000) for a case study in northeast Asia, it was shown that regional pollution and biomass burning play important roles in raising carbon monoxide concentrations [48].

Figure 5 shows the Aerosol Optical Depth (AOD) obtained from MODIS and the atmospheric temperature

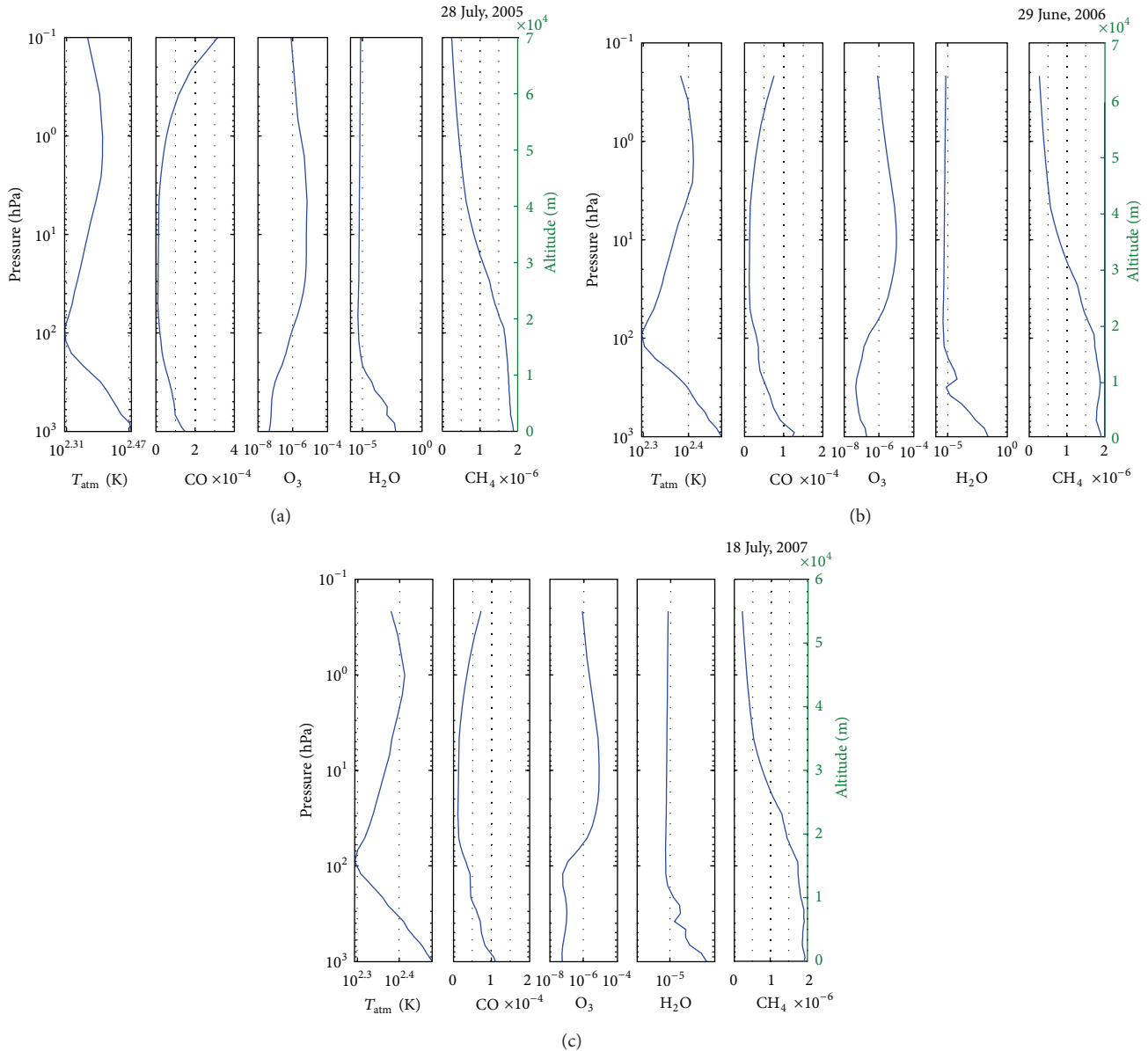


FIGURE 1: Vertical profiles of TES-derived parameters for selected summer months and days during 2005, 2006, and 2007.

observations from TES at 908 hPa. High AOD values were found on 14/9/05, 25/3/06, 31/7/06, 16/8/06, 13/4/07, and 6/10/07 indicating about two highs per year with about 5 months between each maximum value. Maximum values correspond to the three major pollution periods of the year. Yet the bimodal distributions indicate two seasonal effects that correspond with the dust season in Feb-March and black episode in Sept-Oct. Low AOD values were observed on 19/12/05, 28/5/06, 23/1/07, 19/8/07, and 9/12/07 which occur either before or after an episode (dust storm, summer pollution, and black cloud). On the other hand, high temperature values were observed on 13/8/05, 13/6/06, 17/9/06, 3/8/07, and 22/10/07 where low values were noted for 21/2/06, 8/2/07, and 25/12/07. It is noteworthy that low temperature values occur during February where a relatively high AOD is observed.

**3.3. Cross Correlations.** Data used in this study was obtained from the TES Giovanni website between the years 2005 and 2010 for an area bordering latitude (29.595, 30.12) and longitude (30.113, 31.425). A 175-day lag was done for 705 observations recorded almost every two days and undergoing quadratic trend removal with a 95% confidence level.

Figure 6 shows cross correlations for water vapor and carbon monoxide against ozone, respectively. The cross correlation between ozone and water vapor has 22 out of 351 significant coefficients at a 95% confidence level. The crosscorrelation for ozone and water vapor revealed an anti correlation agreeing with the previous time series analysis of tropospheric ozone and water vapor that are negatively correlated throughout most of the tropics [49]. The rising of the tropospheric air masses associated with convection

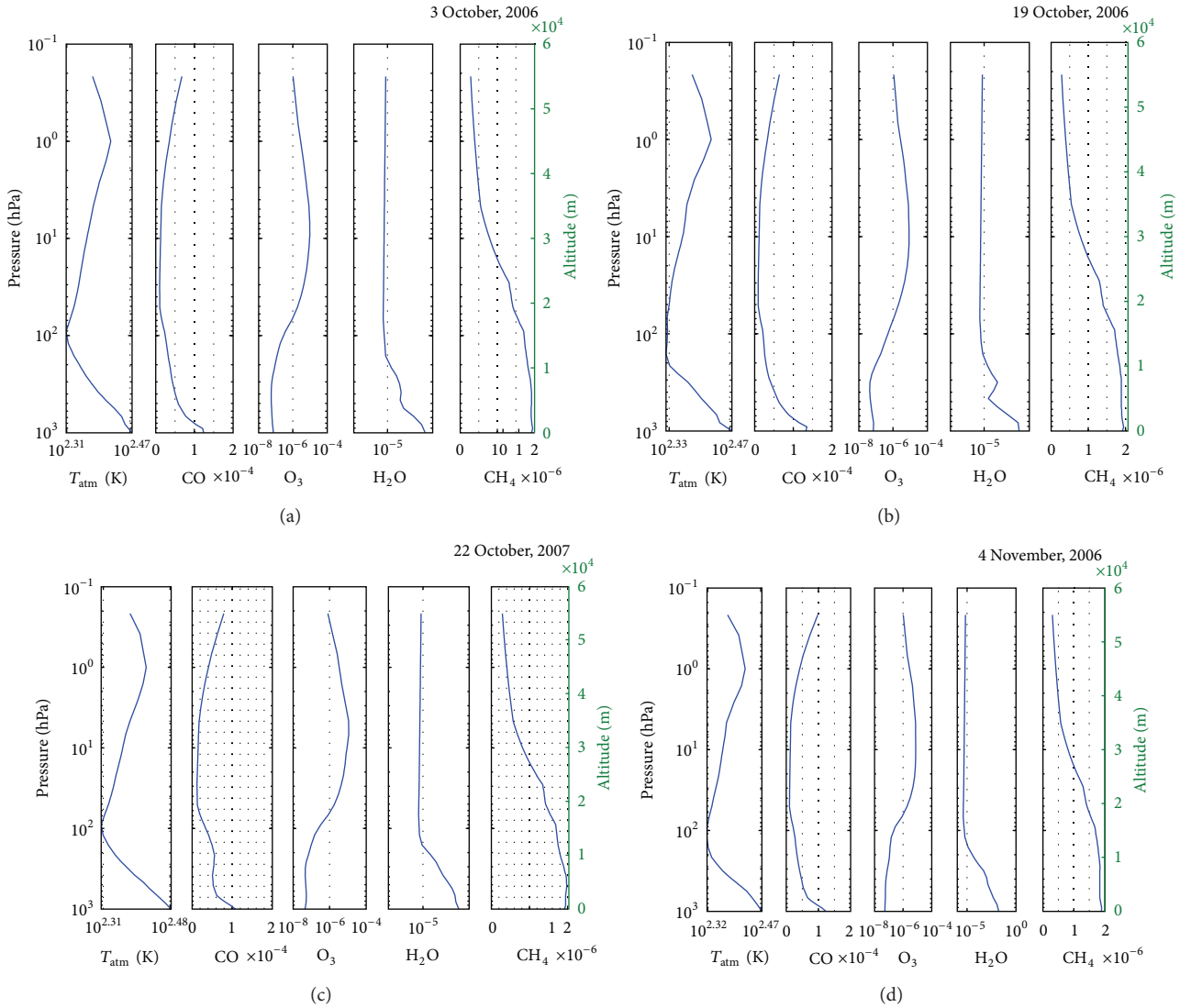


FIGURE 2: Vertical profiles of TES-derived parameters for selected dates experiencing the black cloud pollution episode during 2006 and 2007.

is a source for the large intertropical seasonal oscillation amplitudes and the anticorrelation measured between tropospheric ozone and water vapor in the tropics. This negative correlation can also be attributed to cloud-lightning  $\text{NO}_x$  (which generates ozone) together with transport effects, in addition to the movement of the tropopause as well as to the transport of low water vapor into a region that may increase the lifetime and abundance of ozone [49]. On the other hand, the cross-correlation between carbon monoxide and ozone shows somewhat symmetrical pattern of oscillations occurring approximately every 85 days. Previous studies have shown a significant correlation of carbon monoxide with ozone [48]. However, CO measurements were used to explore the correlation between biomass burning and ozone profiles and it was found that these correlations are rather complicated [50].

Figure 7 shows the cross correlations of night atmospheric temperatures with various measured parameters at

a lag of 175 days for the years 2005–2010. Day atmospheric temperature measurements did not coincide with the rest of the parameters, so they were disregarded. Figure 7(a), shows a time delay between temperature and carbon monoxide (measured from minimum to maximum) of about 100 days and a strong anticorrelation exists at zero lag. There are statistically 35 significant coefficients out of 351 at a 95% confidence level. On the other hand, the relation between atmospheric temperature and ozone shows a more defined pattern than with carbon monoxide, indicating a higher degree of dependence (Figure 7(b)). This time the significant coefficients are 24 with a 95% confidence level. The concentration of ozone increases to the maximum with an increase in temperature after 40 days. However, the cross correlation between atmospheric temperature and water vapor highlighted that small amounts of water vapor can result in great variations of air temperature [51]. Here, there are 33 significant coefficients at a 95% confidence level.

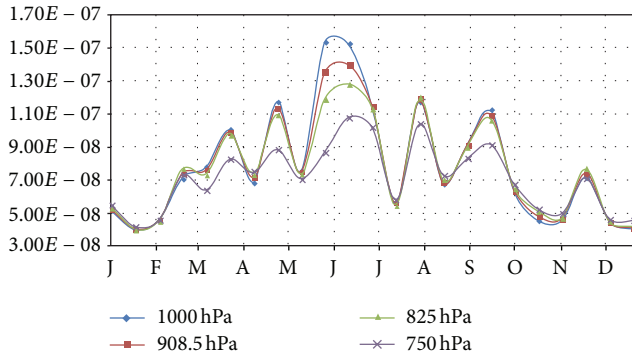


FIGURE 3: Time series for ozone measurements during 2007 concentrating on four different pressure levels, 749 hPa, 825 hPa, 908 hPa, and 1000 hPa, generated from TES, Aura.

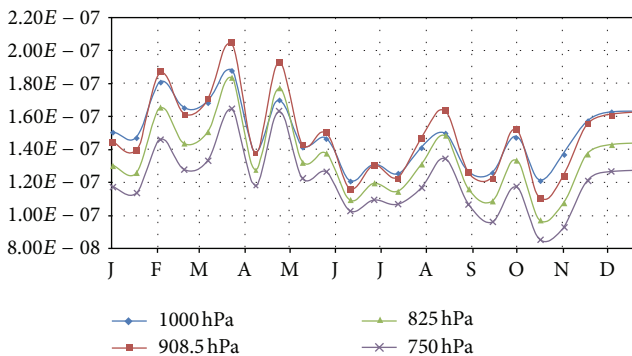


FIGURE 4: Time series for carbon monoxide measurements during 2007 concentrating on four pressure levels at 749 hPa, 825 hPa, 908 hPa, and 1000 hPa.

Previous figures showed that water vapor displays a strong oscillation and a seasonal pattern which could be the effect of temperature changes. We found that monthly AOD means are anticorrelated with monthly precipitation, which suggests that precipitation is not only vital in winter aerosol removal processes but also in the accumulation of particles during summer [2, 16]. This is confirmed through a study where the seasonality of surface temperature and of convection, as well as seasonal variations in monsoon circulation, produce associated seasonal changes in water vapor in the troposphere [51].

#### 4. HYSPLIT Back Trajectories and MODIS Fire Counts

We have used the NOAA Air Resources Laboratory (ARL) HYSPLIT model (HYbrid Single-Particle Lagrangian Integrated Trajectory) Model access via NOAA ARL READY Website (<http://www.arl.noaa.gov/HYSPLIT.php>) NOAA Air Resources Laboratory, College Park, MD. for computing trajectories over Cairo. Gridded meteorological data, at regular time intervals, are used in calculation of air mass trajectories. Data for the back trajectories are obtained from existing archives.

Four HYSPLIT back trajectories were generated, each representing a season. Three altitudes were considered, 500 m, 700 m, and 900 m. Low altitudes below 1 km were used because it was found that anthropogenic pollutants during September, October, and November are found at low altitudes [52]. A corresponding wind rose at 950 mb was added to show the dominant wind direction for 6 hours for further investigation.

The back trajectories of the major months having episodes occurring are studied using a one-day back trajectory (Figure 8). The air mass back trajectories are done at three different heights to locate the vertical extent of the different contributions in the pollution during air pollution episodes [52]. We assume that at these heights an inversion layer may appear to take place since anthropogenic pollutants occurring especially in mid-October and November hang at low altitudes. The presence of inversion layers traps the pollutants at a low elevation causing them to increase in concentration [52]. This causes the haze that can be seen hovering over Cairo during the black cloud episode.

During the second half of the year, the wind speed is less as can be seen from the wind rose in July and November. Thus, weaker convection would favor aerosol accumulation. This coincides with the increase of ozone during the summer and the increase of CO during autumn. Fire counts from MODIS in Figure 9 show the highest values are during the months of the black cloud episode, September, October, and November over a period of 7 years. A closer look showed the highest activity to have occurred during the years 2006 and 2007 [26]. The timing was found to coincide with the practicing of burning open field wastes, during September till November. Details on this can be found in Marey et al., 2010 [26].

## 5. Results and Discussion

In addition to Cairo's economic growth, its location, topography, and complex climate systems play vital roles in the presence of black cloud episodes. Its location subjects it to blown sand and dust storms from the western desert (since Egypt is 90% desert), transformation of air pollutants from Europe, emissions of atmospheric constituents from Africa, and the effect of trade winds diminishing over the Mediterranean during black cloud periods. The topography of Cairo city, between the eastern and the western highlands, blocks the pollutants and suppresses the motion of the suspended particulates, especially from September through November when wind currents are weak. In winter, transport processes in the African upper troposphere are driven by the strong winter Hadley Meridional circulation. Wind and humidity are two factors that influence the behavior of air pollutants.

In summer, the effect of wind and humidity is from the east and the Asian monsoon anticyclone. During Africa's Northern Hemisphere April-May monsoon, ozone precursors generated from biomass burning in the south are transported to the Intertropical Convergence Zone and affect the composition of Africa's upper troposphere [29]. Smoke or air pollution concentrations are highest with low wind

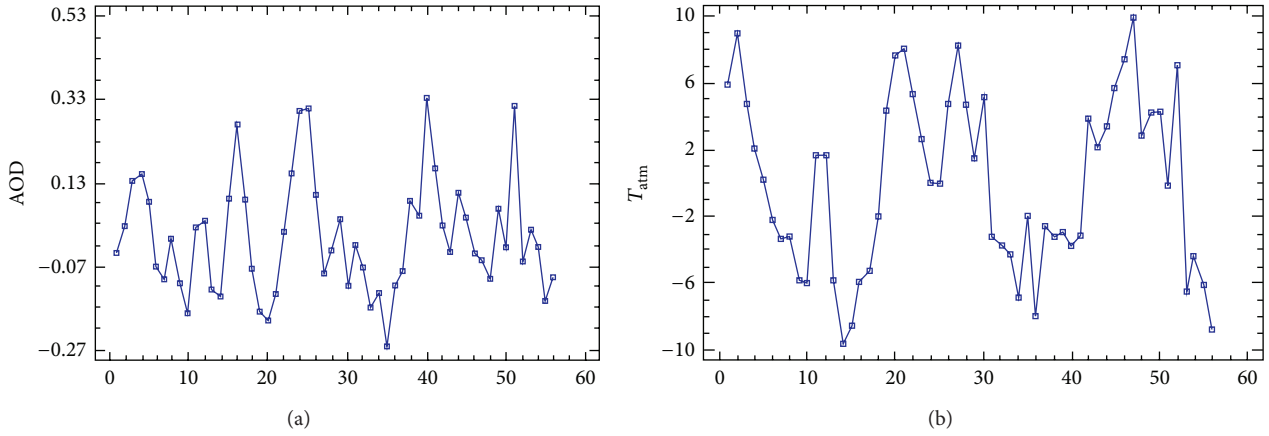


FIGURE 5: Time series for (a) aerosol optical depth measurements generated using MODIS data and (b) atmospheric temperature at 908 hPa generated using TES data.

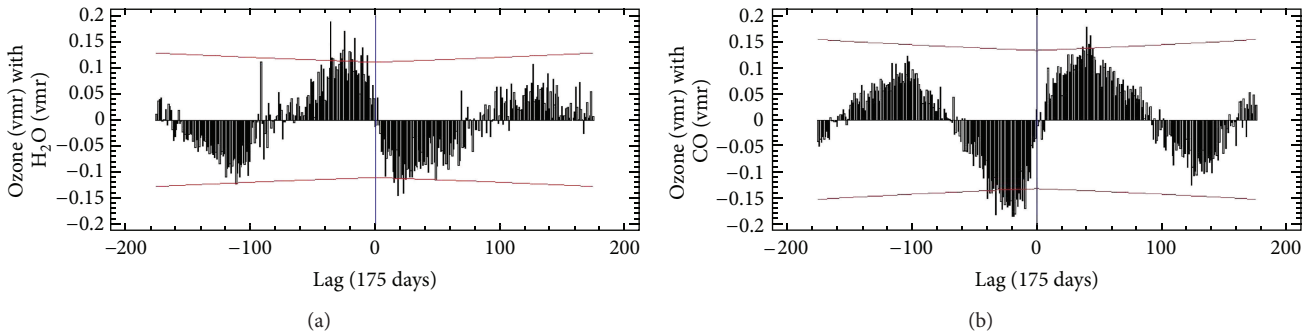


FIGURE 6: Cross correlation between ozone and (a) water vapor and (b) carbon monoxide for years 2005–2010.

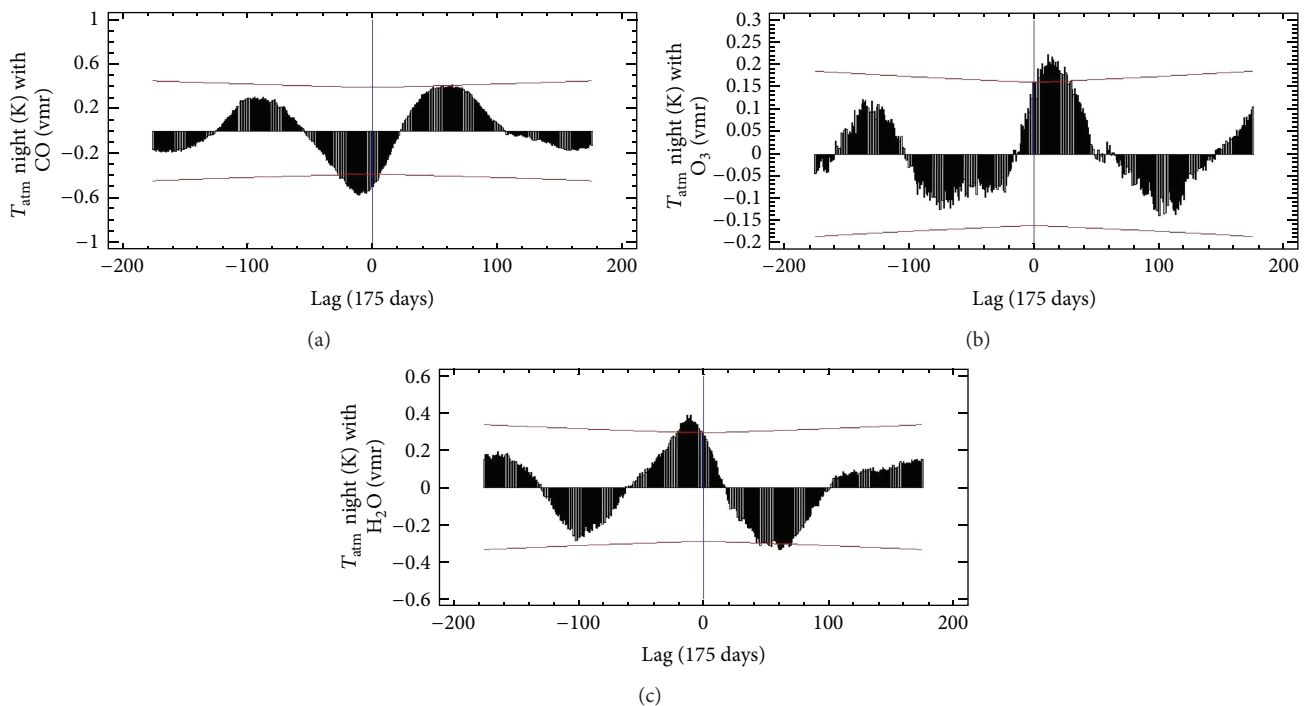


FIGURE 7: Cross correlation of night atmospheric temperature with CO, ozone, and water vapor, respectively.

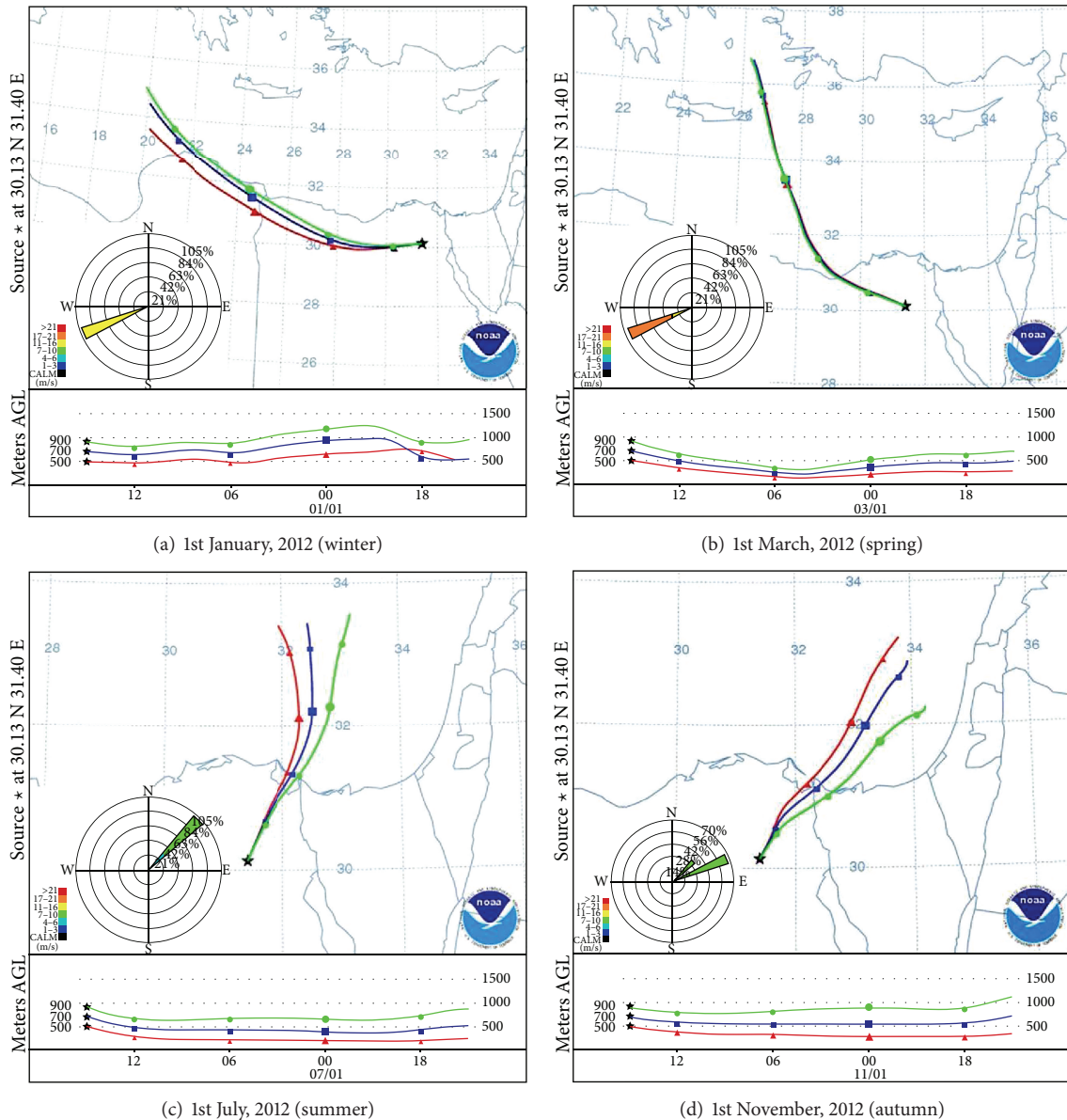


FIGURE 8: HYSPLIT and wind rose graphs for the four seasons in 2012. Three altitudes were considered: green 900 m, blue 700 m, and red 500 m. Win rose was generated at 950 mb.

speeds, low vertical turbulence, temperature inversions, and high humidity [30]. Therefore, it can be seen that the North African/East Mediterranean troposphere is a crossroad to various transport processes on both regional and intercontinental scales. A study on this pollution crossroad showed that pollution generated by Asia can be transported towards Africa by the anticyclone flow of the Asian summer monsoon [29].

During winter, and especially in the month of February, dust emissions have been linked to Saharan cyclones and may contribute to the total dust load over West and North Africa [53, 54]. It was also found that February is one of the months where dust observations are very high and oscillations in various parameters have been found [20]. Meteorological

data were used in the HYSPLIT model to identify the sources of the peak of these different parameters by performing back trajectories. Forward trajectories assessed the fate of this pollution for specific dates of interest.

The climatic origins of different black cloud episodes over Cairo are identified. Peaks of carbon monoxide occur during the March and April dust events from the western desert. However, AOD in the northern hemisphere is at a maximum from April to August and diminishes in December [55]. Perturbations such as these are usually the result of either wildfires or biomass burning confirming that biomass burning is a serious cause of these perturbations [55].

During summer, especially June, ozone concentrations are high where Europe's pollution contributes to Cairo's

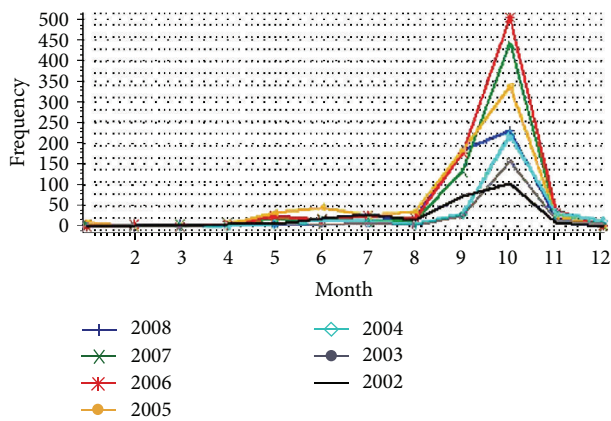


FIGURE 9: Monthly average fire counts over the Nile Delta during 2002–2009 courtesy of Marey et al., 2010 [26].

air pollution through global transport processes, most of which is transported south at low altitudes in the summer to the Mediterranean Sea, North Africa, and the Near East [44]. It was found that in 1994, the long-range or trans-boundary transport of ozone originating in Europe caused the ozone concentrations over the countries bordering the Mediterranean Sea to exceed the European standard and contributed to a monthly mean of 5–20 ppbv ozone [44]. The long range transported pollutants contributed to the pollution violations occurring from March to October in the Mediterranean region and at least 10 violations over Egypt, including the heavily populated Nile River Valley [42]. Additional pollution violations for health occur almost every day during the months of June, July, and August over heavily populated regions in North Africa and the near east.

Finally, during September and October, Cairo experiences black cloud peaks of ozone. Many local factors contribute to the deterioration of Cairo's air quality, including natural sources from inland deserts and anthropogenic sources such as vehicles, power plants, open air waste burning, and the cement industry [16]. It was argued that the main contributing factor to the black cloud pollution is the burning of agricultural waste during the fall season [16].

## 6. Conclusions

The following conclusions are made

- (1) Data on air pollution levels of various atmospheric pollutants, greenhouse gases and parameters are available at no cost through various atmospheric and air pollution satellites. Analysis and interpretation of these data can provide very useful information and conclusions regarding atmospheric dynamics and aerosols in the atmosphere.
- (2) Performing autocorrelations, cross correlations, and backward and forward trajectories helps clarify the weather pattern of a specific location.
- (3) Cairo's topography of the Delta region contributes to the stagnant air that enhances air pollution episodes.

- (4) Dust levels are high during the month of February, forced by Saharan cyclones.
- (5) Dust storms emerging from the western desert result in peaks of carbon monoxide concentrations during March and April.
- (6) During summer, especially June, high concentrations of ozone are a result of trans-boundary transportation of ozone from Europe.
- (7) September and October are well known for the appearance of the "black cloud" episode. Most researchers argue that the primary source of these episodes is biomass burning caused specifically from the burning of rice straw after the rice harvesting season.

## References

- [1] P. Ginoux, D. Garbuzov, and N. C. Hsu, "Identification of anthropogenic and natural dust sources using moderate resolution imaging spectroradiometer (MODIS) deep blue level 2 data," *Journal of Geophysical Research D*, vol. 115, no. 5, Article ID D05204, 2010.
- [2] Y. J. Kaufman, D. Tanrè, and O. Boucher, "A satellite view of aerosols in the climate system," *Nature*, vol. 419, pp. 215–223, 2002.
- [3] M. D. King, Y. J. Kaufman, D. Tanrè, and T. Nakajima, "Remote sensing of tropospheric aerosols from space: past, present, and future," *Bulletin of American Meteorological Society*, vol. 80, no. 11, pp. 2229–2260, 1999.
- [4] M. Astitha, G. Kallos, and P. Katsafados, "Air pollution modeling in the Mediterranean region: analysis and forecasting of episodes," *Atmospheric Research*, vol. 89, no. 4, pp. 358–364, 2008.
- [5] G. Kallos, V. Kotroni, K. Lagouvardos, and A. Papadopoulos, "On the long-range transport of air pollutants from Europe to Africa," *Geophysical Research Letters*, vol. 25, no. 5, pp. 619–622, 1998.
- [6] G. Kallos, M. Astitha, P. Katsafados, and C. Spyrou, "Long-range transport of anthropogenically and naturally produced particulate matter in the Mediterranean and North Atlantic: current state of knowledge," *Journal of Applied Meteorology and Climatology*, vol. 46, no. 8, pp. 1230–1251, 2007.
- [7] J. Lelieveld, H. Berresheim, S. Borrmann et al., "Global air pollution crossroads over the Mediterranean," *Science*, vol. 298, no. 5594, pp. 794–799, 2002.
- [8] E. Gerasopoulos, P. Kokkalis, V. Amiridis et al., "Dust specific extinction cross-sections over the Eastern Mediterranean using the BSC-DREAM model and sun photometer data: the case of urban environments," *Annales Geophysicae*, vol. 27, no. 7, pp. 2903–2912, 2009.
- [9] E. Gerasopoulos, V. Amiridis, S. Kazadzis et al., "Three-year ground based measurements of aerosol optical depth over the Eastern Mediterranean: the urban environment of Athens," *Atmospheric Chemistry and Physics*, vol. 11, no. 5, pp. 2145–2159, 2011.
- [10] M. J. Molina and L. T. Molina, "Megacities and atmospheric pollution," *Journal of the Air and Waste Management Association*, vol. 54, no. 6, pp. 644–680, 2004.
- [11] *Egypt State of the Environment Report 2005*, Ministry of State of Environmental Affairs, Cairo, Egypt, 2006.

- [12] H. El-Askary and M. Kafatos, "Dust storm and black cloud influence on aerosol optical properties over Cairo and the Greater Delta region, Egypt," *International Journal of Remote Sensing*, vol. 29, no. 24, pp. 7199–7211, 2008.
- [13] O. Favez, H. Cachier, J. Sciare et al., "Seasonality of major aerosol species and their transformations in Cairo megacity," *Atmospheric Environment*, vol. 42, no. 7, pp. 1503–1516, 2008.
- [14] H. El-Askary, A. K. Prasad, G. Kallos, M. El-Raey, and M. Kafatos, "Analyzing black cloud dynamics over Cairo, Nile Delta region and Alexandria using aerosols and water vapor data," in *Air Quality-Models and Applications*, chapter 12, pp. 211–232, InTECH, 2011.
- [15] H. El-Askary, "Air pollution impact on aerosol variability over mega cities using remote sensing technology: case study, Cairo, Egypt," *Egyptian Journal of Remote Sensing & Space Science*, vol. 9, pp. 31–40, 2006.
- [16] A. S. Zakey, M. M. Abdelwahab, and P. A. Makar, "Atmospheric turbidity over Egypt," *Atmospheric Environment*, vol. 38, no. 11, pp. 1579–1591, 2004.
- [17] M. Abu-Allaban, A. W. Gertler, and D. H. Lowenthal, "A preliminary apportionment of the sources of ambient PM<sub>10</sub>, PM<sub>2.5</sub>, and VOCs in Cairo," *Atmospheric Environment*, vol. 36, no. 35, pp. 5549–5557, 2002.
- [18] M. Abu-Allaban, D. H. Lowenthal, A. W. Gertler, and M. Labib, "Sources of PM<sub>10</sub> and PM<sub>2.5</sub> in Cairo's ambient air," *Environmental Monitoring and Assessment*, vol. 133, no. 1–3, pp. 417–425, 2007.
- [19] M. El-Metwally, S. C. Alfaro, M. Abdel Wahab, and B. Chatenet, "Aerosol characteristics over urban Cairo: seasonal variations as retrieved from Sun photometer measurements," *Journal of Geophysical Research D*, vol. 113, no. 14, Article ID D14219, 2008.
- [20] H. El-Askary, R. Farouk, C. Ichoku, and M. Kafatos, "Transport of dust and anthropogenic aerosols across Alexandria, Egypt," *Annales Geophysicae*, vol. 27, no. 7, pp. 2869–2879, 2009.
- [21] E. Hossny, G. Mokhtar, M. El-Awady, I. Ali, M. Morsy, and A. Dawood, "Environmental exposure of the pediatric age groups in Cairo City and its suburbs to cadmium pollution," *Science of the Total Environment*, vol. 273, no. 1–3, pp. 135–146, 2001.
- [22] M. Abu-Allaban, D. H. Lowenthal, A. W. Gertler, and M. Labib, "Sources of volatile organic compounds in Cairo's ambient air," *Environmental Monitoring and Assessment*, vol. 157, no. 1–4, pp. 179–189, 2009.
- [23] S. C. Alfaro and M. Abdel Wahab, "Extreme variability of aerosol optical properties: the cairo aerosol characterization experiment case study," in *Remote Sensing of the Atmosphere for Environmental Security*, NATO Security through Science Series, pp. 285–299, 2006.
- [24] M. Kanakidou, N. Mihalopoulos, T. Kindap et al., "Megacities as hot spots of air pollution in the East Mediterranean," *Atmospheric Environment*, vol. 45, no. 6, pp. 1223–1235, 2011.
- [25] K. F. Mahmoud, S. C. Alfaro, O. Favez, M. M. Abdel Wahab, and J. Sciare, "Origin of black carbon concentration peaks in Cairo (Egypt)," *Atmospheric Research*, vol. 89, no. 1–2, pp. 161–169, 2008.
- [26] H. S. Marey, J. C. Gille, H. M. El-Askary, E. A. Shalaby, and M. E. El-Raey, "Study of the formation of the 'black cloud' and its dynamics over Cairo, Egypt, using MODIS and MISR sensors," *Journal of Geophysical Research D*, vol. 115, no. 21, Article ID D21206, 2010.
- [27] H. S. Marey, J. C. Gille, H. M. El-Askary, E. A. Shalaby, and M. E. El-Raey, "Aerosol climatology over Nile Delta based on MODIS, MISR and OMI satellite data," *Atmospheric Chemistry and Physics*, vol. 11, no. 20, pp. 10637–10648, 2011.
- [28] A. K. Prasad, H. El-Askary, and M. Kafatos, "Implications of high altitude desert dust transport from Western Sahara to Nile Delta during biomass burning season," *Environmental Pollution*, vol. 158, no. 11, pp. 3385–3391, 2010.
- [29] B. Barret, P. Ricaud, C. Mari et al., "Transport pathways of CO in the African upper troposphere during the monsoon season: a study based upon the assimilation of spaceborne observations," *Atmospheric Chemistry and Physics*, vol. 8, no. 12, pp. 3231–3246, 2008.
- [30] R. G. Barry, *Mountain Weather and Climate*, Routledge, 1992.
- [31] D. P. Edwards, L. K. Emmons, D. A. Hauglustaine et al., "Observations of carbon monoxide and aerosols from the Terra satellite: northern hemisphere variability," *Journal of Geophysical Research D*, vol. 109, no. 24, pp. 1–17, 2004.
- [32] S. S. Kulawik, J. Worden, A. Eldering et al., "Implementation of cloud retrievals for Tropospheric Emission Spectrometer (TES) atmospheric retrievals: part I. Description and characterization of errors on trace gas retrievals," *Journal of Geophysical Research D*, vol. 111, no. 24, Article ID D24204, 2006.
- [33] M. W. Shephard, H. M. Worden, K. E. Cady-Pereira et al., "Tropospheric Emission Spectrometer nadir spectral radiance comparisons," *Journal of Geophysical Research*, vol. 113, no. D115, Article ID D15S05, 2008.
- [34] C. P. Rinsland, M. Luo, M. W. Shephard et al., "Tropospheric emission spectrometer (TES) and atmospheric chemistry experiment (ACE) measurements of tropospheric chemistry in tropical southeast Asia during a moderate El Niño in 2006," *Journal of Quantitative Spectroscopy and Radiative Transfer*, vol. 109, no. 10, pp. 1931–1942, 2008.
- [35] J. A. Logan, I. Megretskaya, R. Nassar et al., "Effects of the 2006 El Niño on tropospheric composition as revealed by data from the Tropospheric Emission Spectrometer (TES)," *Geophysical Research Letters*, vol. 35, no. 3, Article ID L03816, 2008.
- [36] R. Beer, M. W. Shephard, S. S. Kulawik et al., "First satellite observations of lower tropospheric ammonia and methanol," *Geophysical Research Letters*, vol. 35, no. 9, Article ID L09801, 2008.
- [37] Y. Choi, Y. Wang, Q. Yang et al., "Spring to summer northward migration of high O<sub>3</sub> over the western North Atlantic," *Geophysical Research Letters*, vol. 35, no. 4, Article ID L04818, 2008.
- [38] R. Beer, "TES on the aura mission: scientific objectives, measurements, and analysis overview," *IEEE Transactions on Geoscience and Remote Sensing*, vol. 44, no. 5, pp. 1102–1105, 2006.
- [39] M. R. Schoeberl, A. R. Douglass, and E. Hilsenrath, "Foreword to the special issue on the EOS aura mission," *IEEE Transactions on Geoscience and Remote Sensing*, vol. 44, no. 5, p. 1063, 2006.
- [40] H. M. Worden, J. A. Logan, J. R. Worden et al., "Comparisons of Tropospheric Emission Spectrometer (TES) ozone profiles to ozonesondes: methods and initial results," *Journal of Geophysical Research D*, vol. 112, no. 3, Article ID D03309, 2007.
- [41] K. W. Bowman, D. Jones, J. Logan et al., "Impact of surface emissions to the zonal variability of tropical tropospheric ozone and carbon monoxide for november 2004," *Atmospheric Chemistry and Physics Discussions*, vol. 8, no. 1, pp. 1505–1548, 2008.
- [42] D. Fu, J. R. Worden, X. Liu, S. S. Kulawik, K. W. Bowman, and V. Natraj, "Characterization of ozone profiles derived from Aura TES and OMI radiances," *Atmospheric Chemistry and Physics*, vol. 13, no. 6, pp. 3445–3462, 2013.

- [43] H. M. Worden, M. N. Deeter, C. Frankenberg et al., “Decadal record of satellite carbon monoxide observations,” *Atmospheric Chemistry and Physics*, vol. 13, pp. 837–850, 2013.
- [44] B. N. Duncan, J. J. West, Y. Yoshida, A. M. Fiore, and J. R. Ziemke, “The influence of European pollution on ozone in the Near East and northern Africa,” *Atmospheric Chemistry and Physics*, vol. 8, no. 8, pp. 2267–2283, 2008.
- [45] S. Chandra, J. R. Ziemke, P. K. Bhartia, and R. V. Martin, “Tropical tropospheric ozone: implications for dynamics and biomass burning,” *Journal of Geophysical Research D*, vol. 107, no. 14, pp. 1–17, 2002.
- [46] A. M. Thompson, J. C. Witte, R. D. Hudson, H. Guo, J. R. Herman, and M. Fujiwara, “Tropical tropospheric ozone and biomass burning,” *Science*, vol. 291, no. 5511, pp. 2128–2132, 2001.
- [47] M. I. Khoder, “Ambient levels of volatile organic compounds in the atmosphere of Greater Cairo,” *Atmospheric Environment*, vol. 41, no. 3, pp. 554–566, 2007.
- [48] S. D. Choi and Y. S. Chang, “Carbon monoxide monitoring in Northeast Asia using MOPITT: effects of biomass burning and regional pollution in April 2000,” *Atmospheric Environment*, vol. 40, no. 4, pp. 686–697, 2006.
- [49] J. R. Ziemke, S. Chandra, M. R. Schoeberl et al., “Intra-seasonal variability in tropospheric ozone and water vapor in the tropics,” *Geophysical Research Letters*, vol. 34, no. 17, Article ID L17804, 2007.
- [50] H. Bremer, J. Kar, J. R. Drummond et al., “Spatial and temporal variation of MOPITT CO in Africa and South America: a comparison with SHADOZ ozone and MODIS aerosol,” *Journal of Geophysical Research D*, vol. 109, no. 12, pp. D12304–10, 2004.
- [51] K. Mohanakumar, *Stratosphere Troposphere Interactions: An Introduction*, Springer, 2008.
- [52] H. El-Askary, A. K. Prasad, G. Kallos, M. El-Raey, and M. Kafatos, “Analyzing black cloud dynamics over Cairo, Nile Delta region and Alexandria using aerosols and water vapor data,” in *Air Quality-Models and Applications*, chapter 12, pp. 211–232, InTECH, 2011.
- [53] A. S. Goudie and N. J. Middleton, “Saharan dust storms: nature and consequences,” *Earth-Science Reviews*, vol. 56, no. 1–4, pp. 179–204, 2001.
- [54] D. B. Karam, C. Flamant, J. Cuesta, J. Pelon, and E. Williams, “Dust emission and transport associated with a Saharan depression: February 2007 case,” *Journal of Geophysical Research D*, vol. 115, no. 13, Article ID D00H27, 2010.
- [55] V. Naik, D. L. Mauzerall, L. W. Horowitz, M. D. Schwarzkopf, V. Ramaswamy, and M. Oppenheimer, “On the sensitivity of radiative forcing from biomass burning aerosols and ozone to emission location,” *Geophysical Research Letters*, vol. 34, no. 3, Article ID L03818, 2007.

## Research Article

# Spatial and Temporal Trends in PM<sub>2.5</sub> Organic and Elemental Carbon across the United States

J. L. Hand,<sup>1</sup> B. A. Schichtel,<sup>2</sup> W. C. Malm,<sup>1</sup> and N. H. Frank<sup>3</sup>

<sup>1</sup> Cooperative Institute for Research in the Atmosphere, Colorado State University, Fort Collins, CO 80523, USA

<sup>2</sup> National Park Service, Cooperative Institute for Research in the Atmosphere, Colorado State University, Fort Collins, CO 80523, USA

<sup>3</sup> Air Quality Assessment Division, U.S. Environmental Protection Agency, Research Triangle Park, NC 27711, USA

Correspondence should be addressed to J. L. Hand; [jlhand@colostate.edu](mailto:jlhand@colostate.edu)

Received 21 February 2013; Accepted 26 July 2013

Academic Editor: Junji Cao

Copyright © 2013 J. L. Hand et al. This is an open access article distributed under the Creative Commons Attribution License, which permits unrestricted use, distribution, and reproduction in any medium, provided the original work is properly cited.

The rural/remote IMPROVE network (Interagency Monitoring of Protected Visual Environments) and the Environmental Protection Agency's urban Chemical Speciation Network have measured PM<sub>2.5</sub> organic (OC) and elemental carbon (EC) since 1989 and 2000, respectively. We aggregated OC and EC data from 2007 to 2010 at over 300 sites from both networks in order to characterize the spatial and seasonal patterns in rural and urban carbonaceous aerosols. The spatial extent of OC and EC was more regional in the eastern United States relative to more localized concentrations in the West. The highest urban impacts of OC and EC relative to background concentrations occurred in the West during fall and winter. Urban and rural carbonaceous aerosols experienced a large (although opposite) range in seasonality in the West compared to a much lower seasonal variability in the East. Long-term (1990–2010) trend analyses indicated a widespread decrease in rural TC (TC = OC + EC) across the country, with positive, though insignificant, trends in the summer and fall in the West. Short-term trends indicated that urban and rural TC concentrations have both decreased since 2000, with the strongest and more spatially homogeneous urban and rural trends in the West relative to the East.

## 1. Introduction

Carbonaceous aerosols, including organic (OC) and elemental (EC) carbon, are ubiquitous in the atmosphere and therefore contribute significantly to particulate matter, both the PM<sub>2.5</sub> fraction [1] and coarse (PM<sub>10</sub>–PM<sub>2.5</sub>) fraction [2, 3], and they contribute to visibility degradation [4, 5] and climate forcing due to their ability to scatter and absorb solar radiation [6, 7]. Carbonaceous aerosols also adversely affect health [8, 9]. Organic carbon can be emitted directly from combustion activities or produced from secondary processes such as gas-to-particle formation. Elemental carbon, also known as light absorbing carbon or black carbon depending on the measurement method, is emitted directly from combustion sources. EC plays a significant role in climate forcing, and a recent review [10] suggests that the climate warming effects of EC are greater than previously thought, although large uncertainties still exist. Characterizing and predicting the complex nature of OC and EC are challenging from both a measurement and modeling framework. However, this

characterization is necessary given the importance of OC and EC to many atmospheric processes and climate impacts.

Comprehensive speciation of carbonaceous aerosols is expensive and time-consuming and therefore usually possible only at a small number of sites for shorter-duration periods, such as the recent CARES study in California [11]. While these types of studies provide extremely useful data on the composition, properties, and sources of carbonaceous aerosols, they are limited in space and time. Large spatial-scale and long-term monitoring networks can provide this information but at the expense of detailed speciated data. An alternative is to measure bulk carbonaceous aerosol properties with methods that are suitable for routine monitoring programs. Such methods include thermal/optical techniques used to analyze particulate matter samples for OC and EC. Two major networks in the United States, the Interagency Monitoring of Protected Visual Environments network (IMPROVE) [12] and the Environmental Protection Agency's (EPA) Chemical Speciation Network (CSN) [13], are responsible for regularly

collecting samples at hundreds of rural and urban sites across the country, respectively, and conducting speciated aerosol analyses that characterize carbonaceous, ionic, and elemental species. In addition, the Southeastern Aerosol Research and Characterization (SEARCH) network collects data from several urban and rural sites in the southeastern United States, from which spatial and temporal trends in inorganic and carbonaceous aerosols in that region have been derived [14–16]. Integrating carbonaceous aerosol data from independent monitoring networks requires reconciliation of data obtained with different samplers, analytical techniques, and artifact corrections that can result in biases in OC and EC concentrations [17–20]. Several studies have reported on the differences and described methods for reconciling IMPROVE and CSN carbon data [1, 21, 22]. Hand et al. [1] aggregated IMPROVE and CSN data to examine the differences in urban and rural aerosols for data from 2005 to 2008. This work focused on the regional and seasonal trends in major aerosol species, including OC and EC.

Many studies have incorporated data from these large-scale networks to understand the sources of carbon aerosols. Jaffe et al. [23] examined interannual variations in IMPROVE  $PM_{2.5}$  mass and OC concentrations in the western United States and attributed it to wildfire impacts. Malm et al. [24] used ratios of OC to EC to deduce source contributions from wildfire and mobile sources using IMPROVE data. Schichtel et al. [25] incorporated IMPROVE OC and EC data with radiocarbon data to estimate fossil and contemporary contributions to total carbon, and Schichtel et al. [26] further apportioned IMPROVE total carbon to major source types, including biomass burning, mobile, and vegetation. A source apportionment study [27] examined IMPROVE and CSN data across sites in Minnesota to determine mobile source contributions and local and regional pollution events. Buzcu-Guven et al. [28] used source apportionment of CSN data at Midwestern sites to determine mobile sources as a major contributor to OC mass. Yu et al. [29] used IMPROVE and SEARCH data to determine contributions from primary and secondary sources to measured OC. In addition to the IMPROVE and CSN, archived filters from the EPA Federal Reference Method (FRM) network from sites across three southeastern U.S. states have been used to determine the spatial and seasonal variability in water-soluble OC [30, 31]. In addition to these analyses, data from large-scale networks are very useful for model evaluation and studies of aerosol transport and processing [32–38] and constrain the role of carbonaceous aerosols in global climate models [39, 40].

The long-term availability of datasets such as those from IMPROVE, CSN, or SEARCH provides the opportunity to study the changes in carbonaceous aerosols over time and assess the success of regulatory efforts in reducing emissions. Trend studies are sensitive to changes in analytical techniques, so an evaluation of long-term trends in EC [41] focused on IMPROVE data from 1990 through 2004, before a hardware upgrade occurred for the carbon analysis. EC has decreased considerably (25%) across the rural United States, with higher rates of decrease in winter compared to summer due to increased EC in the West/Southwest, most likely due to impacts from biomass burning. Chen et al.

[42] also reported on decreased EC concentrations from the IMPROVE network. From the SEARCH network in the southeastern United States, Blanchard et al. [16] reported that the annual mean organic matter and EC concentrations decreased by 3.3 to 6.5%  $yr^{-1}$  and 4.0 to 7.8%  $yr^{-1}$ , respectively, from 1999 through 2010. The greatest decrease in EC concentrations occurred at urban sites.

The contributions provided by this study include a recent analysis (2007–2010) and integration of IMPROVE and CSN OC and EC data, with specific focus on the integrated spatial and seasonal trends in absolute and relative concentrations. In addition, long-term (1990–2010) and short-term (2000–2010) trends in seasonal mean total carbon ( $TC = OC + EC$ ) from integrated urban and rural sites are also examined.

## 2. Data and Methods

The IMPROVE network has been collecting samples for speciated aerosol analysis since 1989 [12] and currently operates 165 sites. IMPROVE sites are primarily in remote and rural areas, and the network's main purposes include tracking and characterizing aerosol composition and visibility in class I areas (federal visibility-protected areas), and determining trends in aerosol concentrations. Much of the monitoring performed by the network is in support of the EPA's Regional Haze Rule, and therefore considerable effort has been invested in maintaining consistency and data quality for the more than two decades the network has been operating. The network collects 24-hr samples every third day from midnight to midnight local time and reports concentrations at ambient conditions.  $PM_{2.5}$  and  $PM_{10}$  samples are collected, and speciated analysis is performed only on the  $PM_{2.5}$  filters. Characterization of anions is determined by IC analysis on nylon filters. Gravimetric  $PM_{2.5}$  and  $PM_{10}$  mass are determined from the weighing of Teflon filters. Concentrations of  $PM_{2.5}$  elemental species are characterized by X-ray fluorescence. Carbon species (OC and EC) are determined from quartz fiber filters analyzed by thermal optical reflectance [43]. OC concentrations reported by IMPROVE are corrected for a positive additive artifact [18, 44, 45] but not a multiplicative negative artifact [22]. We refer to the refractory carbon fraction as EC to reflect its operational definition while recognizing that the fraction contains nongraphitic carbon that absorbs light and complicates the split between EC and OC [46]. Additional details regarding IMPROVE instrumentation, sampling, analysis, artifact correction, and site information are available elsewhere [5, 12]. All IMPROVE data, metadata, and detailed descriptions of the network operations and data analysis and visualization results are available for download [47].

EPA's CSN urban network was deployed in 2000 [13] and currently operates over 200 sites. The objectives of the CSN are to track progress of emission reduction strategies through trend analyses, evaluate air quality models, support regulatory efforts for visibility, and for source apportionment and health effects studies. The CSN collects 24-h samples every third day on the same sampling schedule as the IMPROVE network. Its monitoring and analysis methods are similar to the IMPROVE network with the exception

that the CSN cold ships their filters and the IMPROVE network does not. The carbon analysis for the CSN was historically performed using thermal optical transmittance and the National Institute of Occupational Health (NIOSH) protocol. With the recognition that different IMPROVE and CSN samplers, as well as different analytical protocols, resulted in different OC and EC concentrations [21, 22, 44], CSN transitioned to an URG-3000N sampler to be more consistent with the IMPROVE sampler, as well as TOR and IMPROVE protocol analysis. The transition began in May 2007 and continued through 2010. Data during the period before transition were adjusted based on the method of Malm et al. [22] to agree with IMPROVE collocated data. Comparisons of adjusted collocated data from 2005 to 2008 showed close agreement [1], and comparisons for 2007–2010 data were similar. The CSN data are available for download [48].

We analyzed data from 2007 to 2010 and required 50% completeness of the data, resulting in 162 IMPROVE and 181 CSN “complete” sites. Seasonal means refer to winter (DJF), spring (MMA), summer (JJA), and fall (SON). The percent contributions of OC and EC to  $PM_{2.5}$  reconstructed fine mass (RCFM) were determined by assuming the aerosols were comprised of ammonium sulfate, ammonium nitrate, particulate organic matter ( $POM = 1.8 \cdot OC$ ), EC, soil, and sea salt. A similar organic multiplier was used for urban and rural POM, although lower values may be more appropriate for urban OC [22, 49]. We combined and interpolated data from both networks using a Kriging algorithm. The resulting fields are not intended for strict interpretation but rather serve to guide the eye for spatial patterns. Interpolations are affected by site density, and the CSN has greater site density in the East, whereas the site density for the IMPROVE network is the highest in the West.

Linear Theil regression [50–52] was performed on total carbon ( $TC = OC + EC$ ) data from “complete” sites, and 70% of “complete” years were required for a trend calculation over a given time period. Trend ( $\% \text{ yr}^{-1}$ ) is defined as the slope from the Theil regression divided by the median concentration over the time period of the trend, multiplied by 100%. Total carbon was used to avoid possible biases in the OC and EC split due to the hardware upgrade in 2005 mentioned previously [41]. Trends were considered significant at the 90th percent significance level ( $p < 0.10$ ) using Kendall tau statistics. Trends were computed for seasonal means for long-term IMPROVE sites over the time period from 1990 to 2010. In 2000, the IMPROVE network expanded, and the CSN began operation, therefore short-term trends were computed from 2000 to 2010.

### 3. Results and Discussion

#### 3.1. Spatial and Seasonal Trends

3.1.1. *POM*. Isopleths of IMPROVE and CSN 2007–2010 seasonal mean POM concentrations for winter, spring, summer, and fall are provided in Figures 1(a)–1(d), respectively. The mean percent contribution of POM to RCFM is shown for the same seasons in Figures 2(a)–2(d). In the western

United States, the regional POM (remote/rural) background was typically less than  $1 \mu\text{g m}^{-3}$ , depending on season, with lower winter and spring concentrations (Figures 1(a) and 1(b), resp.). During summer, the western background concentration increased to  $2\text{--}3 \mu\text{g m}^{-3}$  (Figure 1(c)), and fall concentrations were closer to  $2 \mu\text{g m}^{-3}$  (Figure 1(d)). The increased summer background concentrations were likely due to the influence of biomass burning emissions and perhaps biogenic emissions [23, 53, 54], as the impacts were more regional in extent. In contrast, more localized high urban concentrations ( $>5 \mu\text{g m}^{-3}$ ) in the West in winter occurred at a range of sites along the coast, and individual sites in Colorado, Utah, Montana, and Arizona. Winter urban sources included residential wood burning, although meteorological effects, such as low ventilation, likely contributed [55]. The fall season in the West appeared to be a transition season with influences from both the summer and winter sources. Contributions to RCFM were significant in the western United States (Figure 2), with values ranging from 40% to over 80% depending on season. The regional impacts in summer and fall were considerable due to the influence of biomass burning (Figures 2(c) and 2(d), resp.). Winter contributions in the West were fairly localized around urban sites and reached 75% or higher (Figure 2(a)), in contrast to spring time contributions of 20%–30% (Figure 2(b)).

In the eastern United States, the background POM concentrations were higher than in the West year-round ( $3\text{--}4 \mu\text{g m}^{-3}$ ), due in part to regionally distributed sources of OC, including secondary organic aerosols from vegetation and wild and prescribed fires [7, 31]. Springtime concentrations were high in the Southeast (Figure 1(b)), most likely associated with biomass burning and a high fire year in 2007 [30, 56, 57]. Summer concentrations were the lowest, although more regional in extent (Figure 1(c)). Secondary organic aerosols from biogenic emissions are known to be important contributors to POM concentrations in the Southeast especially in summer [15, 25, 58, 59], and the higher background concentrations and large regional extent reflects this source. Residential wood burning was likely an important source in fall and winter [30, 57]. The contribution of POM to RCFM in the East was significantly lower than in the West ( $<50\%$ ) year-round. This difference mainly was due to the prevalence of other species, such as sulfate, which has abundant sources in the East and dominates RCFM, especially in summer [1].

3.1.2. *EC*. Seasonal mean EC isopleths are shown in Figures 3(a)–3(d), and seasonal mean percent contributions of EC to RCFM are shown in Figures 4(a)–4(d). Rural background EC concentrations ranged from 0.1 to  $0.3 \mu\text{g m}^{-3}$ , with lower values in the West. In the West, especially winter and fall, localized impacts from individual urban sites produced higher concentrations (up to a factor of 10 higher) with steep spatial gradients, suggesting a limited spatial extent. Urban EC sources likely included residential heating and other urban combustion sources, including mobile sources [25, 58] that were most likely trapped due to low ventilation. EC hotspots did not occur necessarily at the same location

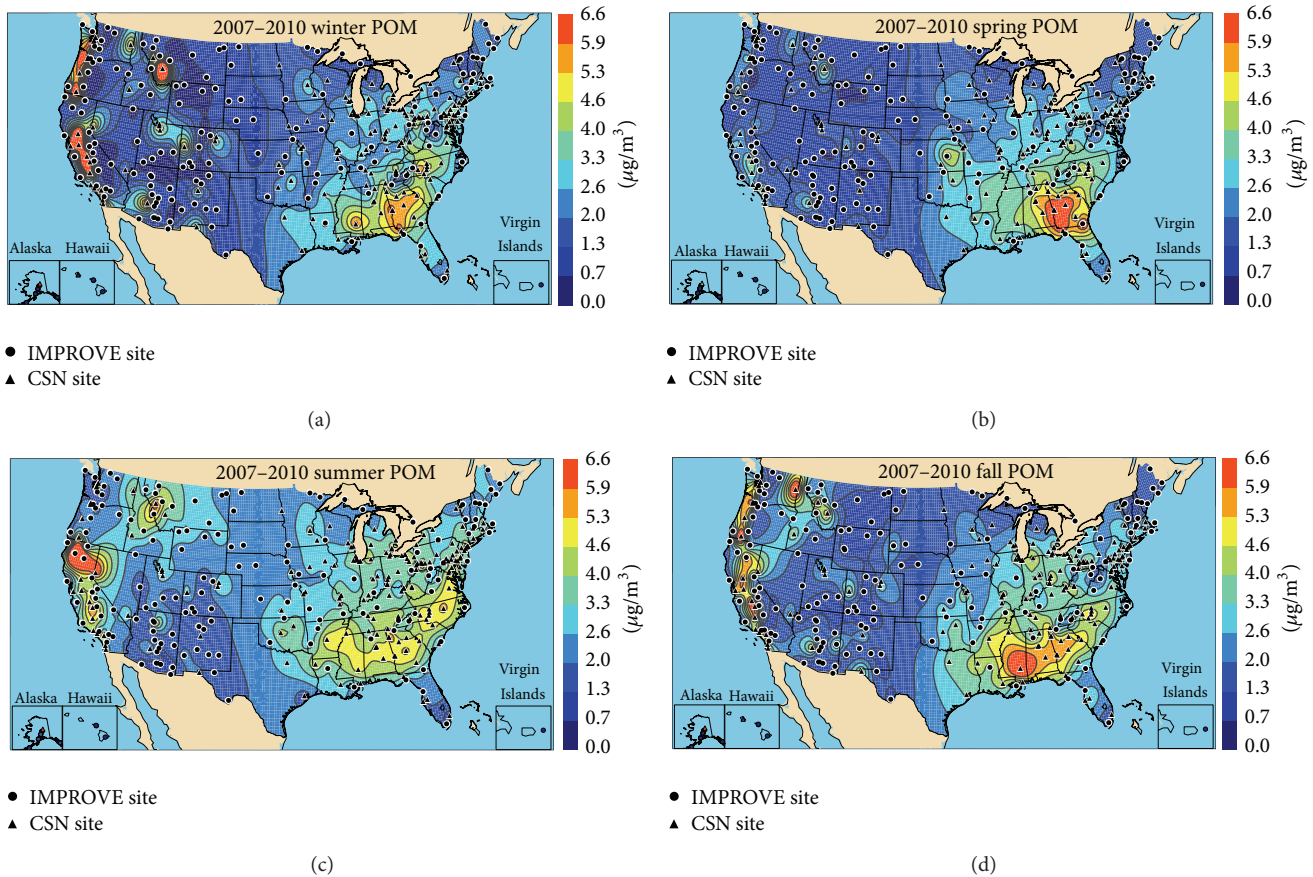


FIGURE 1: IMPROVE and CSN 2007–2010 seasonal mean  $PM_{2.5}$  particulate organic matter (POM) ( $\mu\text{g}/\text{m}^3$ ) for (a) winter (DJF), (b) spring (MAM), (c) summer (JJA), and (d) fall (SON). IMPROVE sites are shown as circles, and CSN sites are shown as triangles.

as high POM concentrations. The impacts from EC emitted from biomass burning in summer were not as great as the impacts from urban sources during fall and winter, probably because of meteorological effects. The contribution of EC to RCFM was quite low (Figure 4); generally the background EC contribution was less than 5%. However, at urban sites in the West, EC contributions were doubled relative to background contributions, with estimates greater than 10%, especially in winter and fall. Background summer contributions in the West reached 7%–9% in some locations, probably due to regional impacts of biomass burning (Figure 4(c)).

The EC influence in the eastern United States appeared to be more regional in extent relative to the West, with a somewhat higher rural background EC concentration of  $0.5 \mu\text{g}/\text{m}^3$  or less. Hecobian et al. [30] reported that biomass burning was the most significant source of brown carbon in the Southeast during colder months, and brown carbon would most likely be characterized as EC by the TOR method [60]. Urban impacts were not as significant in the East, especially compared to winter in the West, except for a few sites in the Southeast and Northeast in the fall. In fact, EC was the highest in general across the eastern United States in the fall. Meteorological effects, such as lower effective transport winds in the West in winter, may play a role in the differences seen between urban and rural EC (and POM) in the East

and West [61]. EC contributions in the eastern United States were typically less than 10%, with its highest contributions in fall across most of the East (Figure 4(d)) and winter in the Southeast (Figure 4(a)). Although relative to other species EC contributions to fine mass were quite low; however, its optical effects were still important given its relatively high optical efficiency [6]. Hand et al. [5] showed that EC contributed as much as 10%–15% annually to reconstructed light extinction coefficients from 2005 to 2008 in the rural West, and 15%–20% or higher at western urban sites.

**3.2. Seasonality.** The seasonality of POM and EC was summarized by aggregating normalized monthly mean data (by annual mean) into broad regions. Regions were defined by separating the country into four large quadrants (Northeast, Southeast, Northwest, and Southwest) at roughly  $-100^\circ$  longitude and  $38^\circ$  latitude based on the spatial patterns presented in the previous section. Normalized monthly mean POM is shown in Figures 5(a) and 5(b). Rural POM seasonality is characterized by maximum and minimum concentrations in warm and cold months, respectively, with timing and range of seasonality varying per region (Figure 5(a)). The largest range of seasonality occurred in the northwestern United States where the highest normalized concentrations in July and August were likely associated with biomass burning

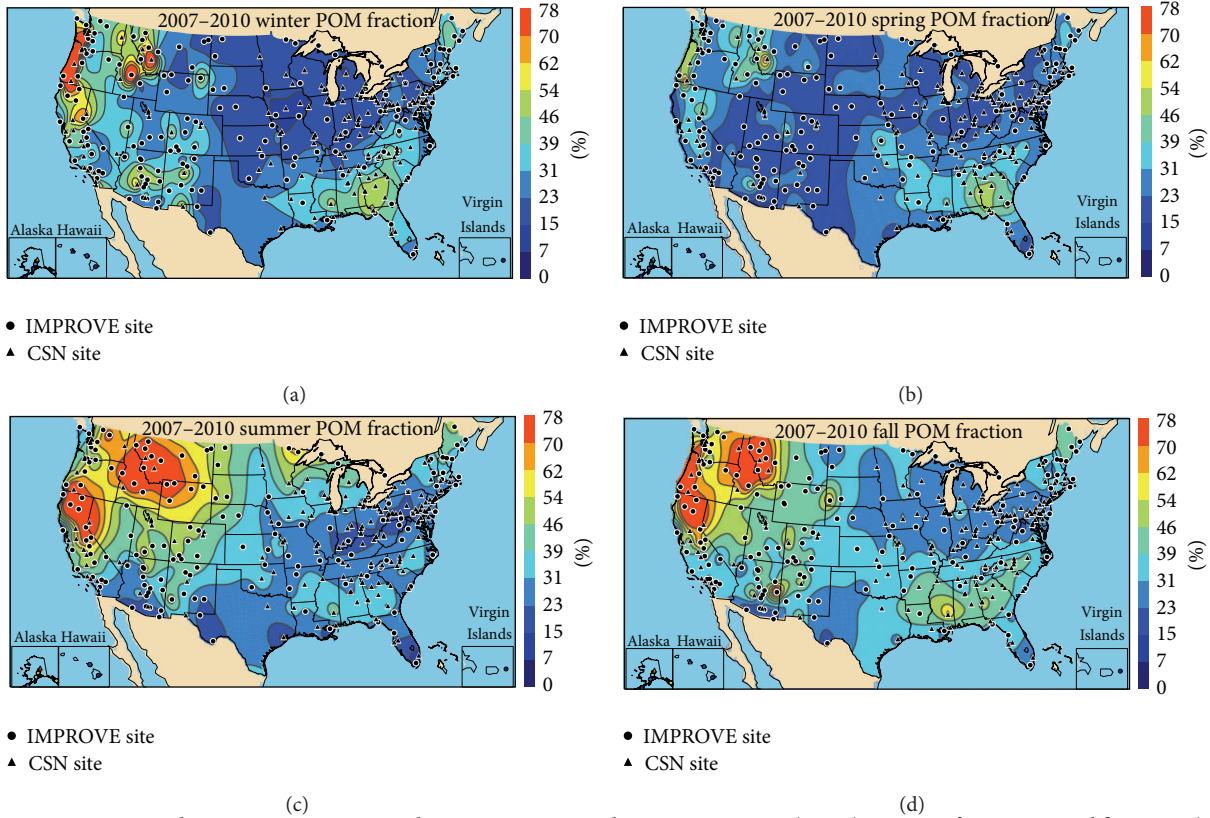


FIGURE 2: IMPROVE and CSN 2007–2010 seasonal mean PM<sub>2.5</sub> particulate organic matter (POM) percent of reconstructed fine mass (RCFM) for (a) winter (DJF), (b) spring (MAM), (c) summer (JJA), and (d) fall (SON). IMPROVE sites are shown as circles, and CSN sites are shown as triangles.

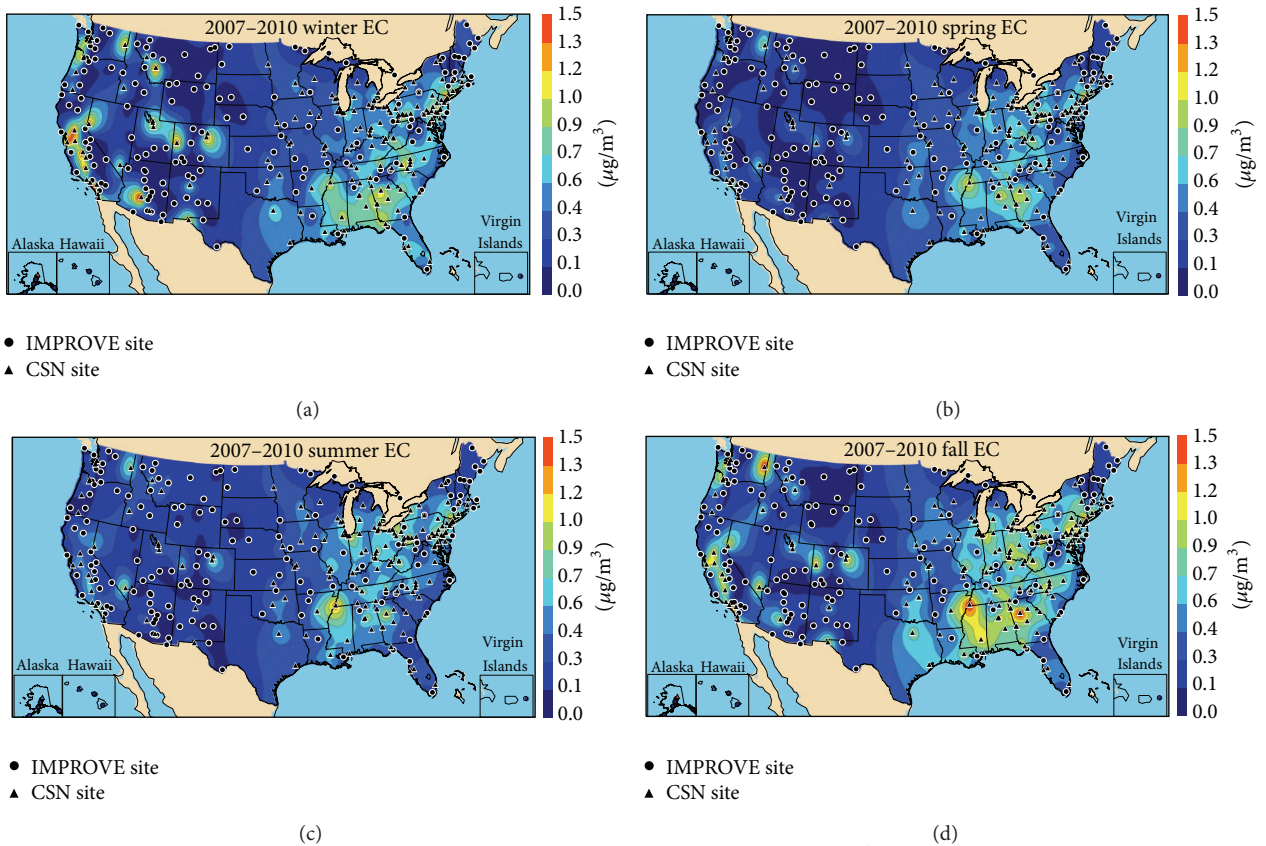


FIGURE 3: IMPROVE and CSN 2007–2010 seasonal mean PM<sub>2.5</sub> elemental carbon (EC) ( $\mu\text{g}/\text{m}^3$ ) for (a) winter (DJF), (b) spring (MAM), (c) summer (JJA), and (d) fall (SON). IMPROVE sites are shown as circles, and CSN sites are shown as triangles.

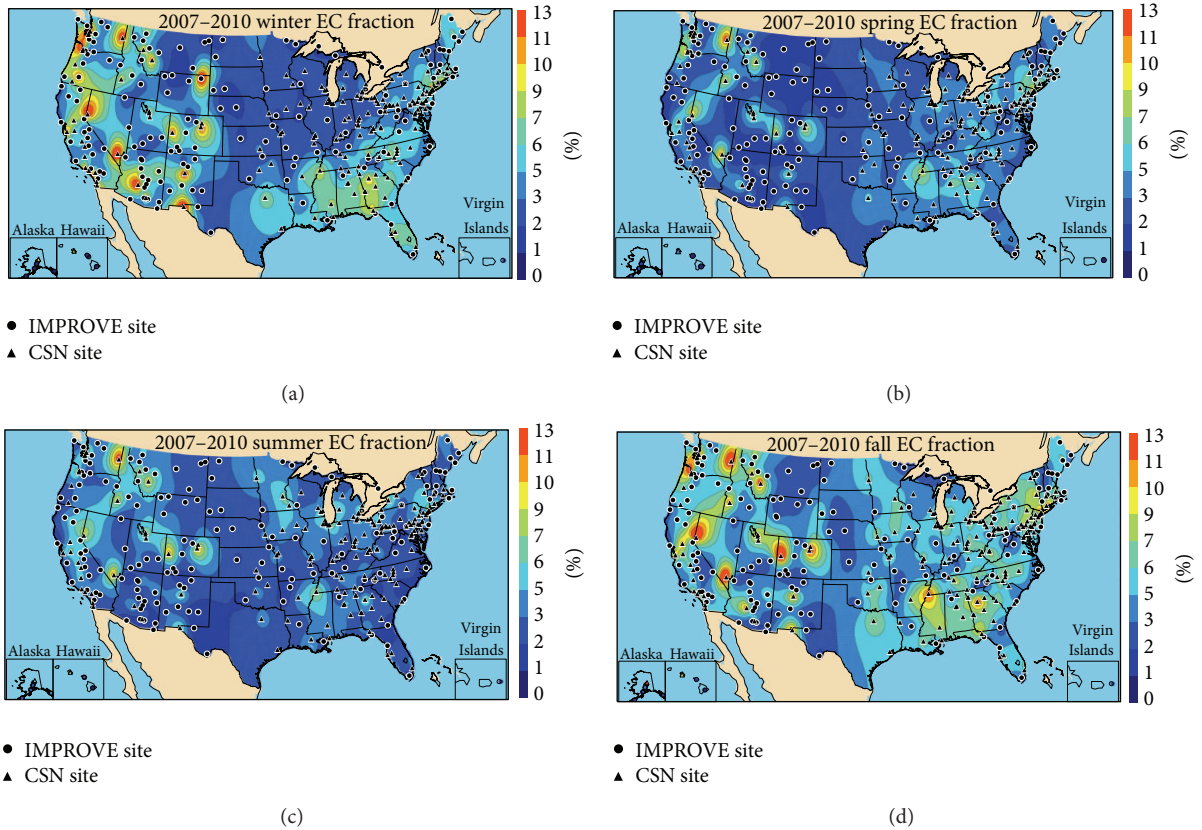


FIGURE 4: IMPROVE and CSN 2007–2010 seasonal mean  $PM_{2.5}$  elemental carbon (EC) percent of reconstructed fine mass (RCFM) for (a) winter (DJF), (b) spring (MAM), (c) summer (JJA), and (d) fall (SON). IMPROVE sites are shown as circles, and CSN sites are shown as triangles.

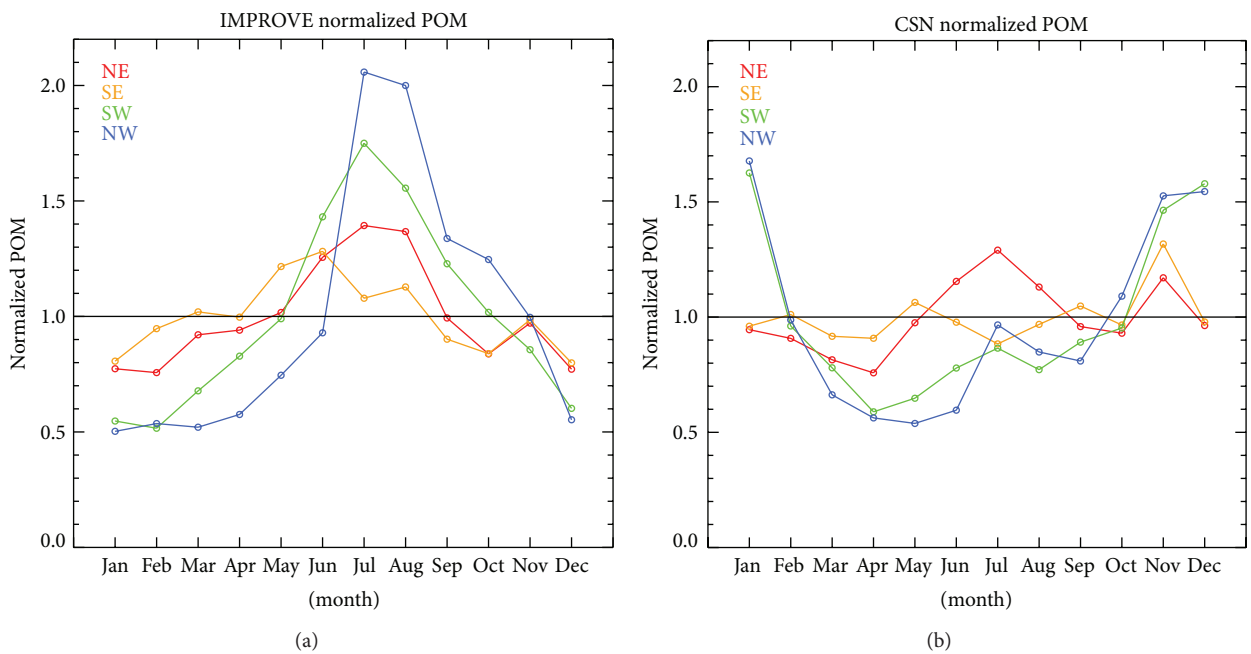


FIGURE 5: 2007–2010 regional monthly mean normalized (by annual mean)  $PM_{2.5}$  particulate organic matter (POM) for (a) IMPROVE and (b) CSN. Regions correspond to the Northeast (NE), Southeast (SE), Southwest (SW), and Northwest (NW).

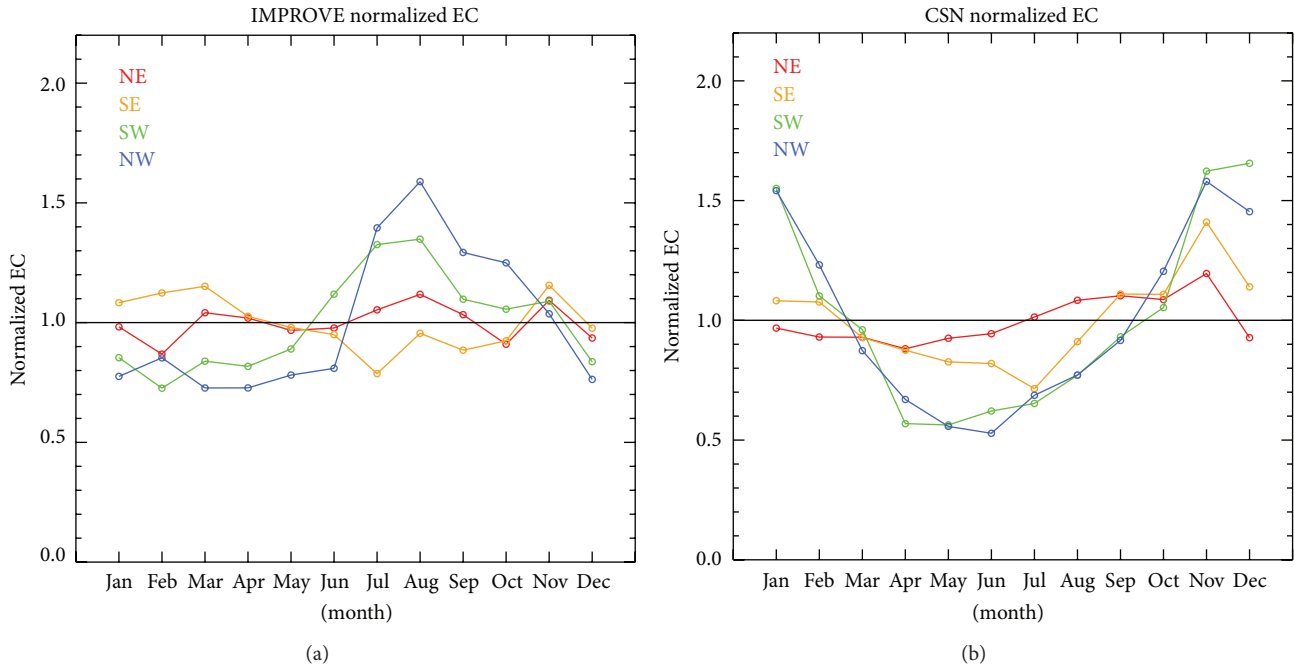


FIGURE 6: 2007–2010 regional monthly mean normalized (by annual mean)  $PM_{2.5}$  elemental carbon (EC) for (a) IMPROVE and (b) CSN. Regions correspond to the Northeast (NE), Southeast (SE), Southwest (SW), and Northwest (NW).

impacts that extended into fall [25, 54]. The second largest range in seasonality occurred in the Southwest where spring relative contributions were more important and summer impacts began somewhat earlier than in the Northwest. In contrast to the West, the eastern United States experienced a much lower range in seasonality in rural POM, although still characterized by a winter minima and spring/summer maxima. In the southeastern United States, higher relative contributions occurred in the spring, particularly May, when prescribed burning occurs. Summer contributions peaked in June and extended through the summer when formation of secondary organic aerosol from vegetation is the highest. Summer relative maxima in the northeastern US region were higher than in the Southeast and encompassed the summer months, most likely due to biogenic emissions. A small increase in rural relative POM in November occurred at both eastern regions.

The opposite seasonality in urban and rural POM in the West is demonstrated clearly in Figure 5(b). The Northwest and Southwest regions had very similar behavior, with urban fall/winter maxima three times higher than spring/summer minima. Relative concentrations increased in summer but not to the extent of the fall/winter maxima. However, in the East, the range of seasonality was much lower, similar to rural regions. Seasonality in the Southeast was nearly flat with a slight increase in May when prescribed burning occurs. Urban POM contributions in the Northeast were highest in summer, similar to the rural region, indicating the regional impacts of biogenic sources of POM in the East. Both eastern regions experienced a peak in November, similar to but larger in magnitude to the rural regions. In addition to different sources, some of the differences in western and eastern POM seasonality were likely due to meteorological effects, with

lower winter ventilation in the West, and higher dilution in the East [61].

Western rural EC seasonality patterns followed that of POM with a higher range in seasonality in the West (greater in the Northwest) likely associated with biomass burning (see Figure 6(a)). In the East the rural EC seasonality was fairly flat, although opposite for both eastern regions. In the Southeast, rural EC peaked in winter and was lowest in summer, while in the Northeast it was fairly flat but somewhat higher in summer. The peak in relative concentration of POM in May was not observed for EC. An increase in rural normalized EC in November in the East also occurred for urban sites (Figure 6(b)); in fact the maximum relative concentrations for both eastern urban regions occurred in November. Otherwise, the seasonality of urban EC was fairly flat in the Northeast, and somewhat greater in the Southeast with a pronounced summer minima. The seasonality of western urban EC relative concentrations followed urban POM closely, with strong winter maxima and summer minima.

**3.3. EC to OC Ratios.** Ratios of EC and OC concentrations provide some indication of source contributions, with higher ratios corresponding to combustion sources that directly emit both primary OC and EC, and relatively lower ratios reflecting the addition of EC from secondary formation processes. Mobile sources have EC/OC ratios around 1 [62], while rural [20, 24, 25] and biomass burning aerosols [63, 64] have much lower ratios ( $\sim 0.1$ ). Organic aerosols with significant secondary contributions are around 0.1–0.2 [65]. In contrast, EC/OC ratios of urban aerosols are relatively high depending on primary and secondary sources ( $\sim 0.47$ – $1.5$ ) [15, 20]. EC/OC ratios are obviously sensitive to and can vary considerably depending on the analytical technique used,

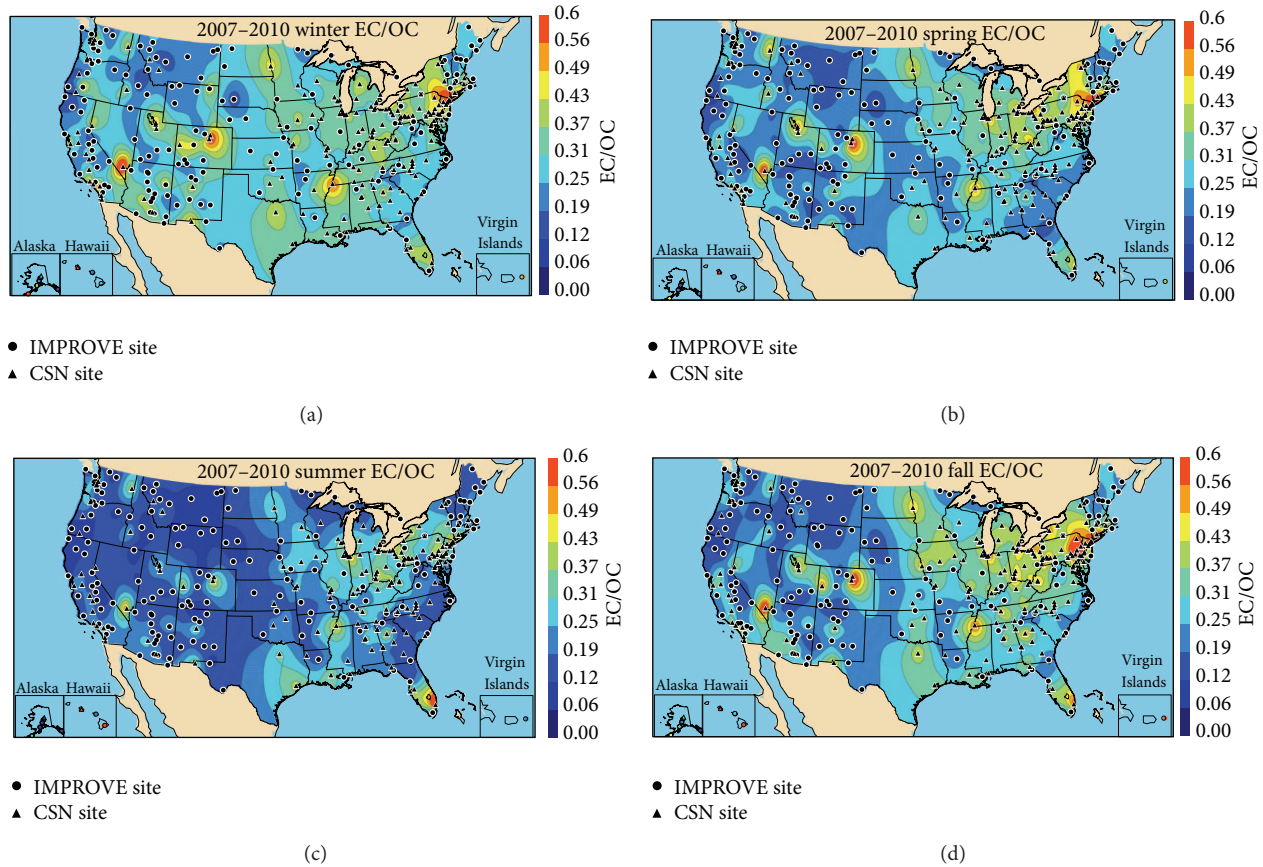


FIGURE 7: IMPROVE and CSN 2007–2010 seasonal mean  $PM_{2.5}$  elemental carbon (EC) to organic carbon (OC) ratios for (a) winter (DJF), (b) spring (MAM), (c) summer (JJA), and (d) fall (SON). IMPROVE sites are shown as circles, and CSN sites are shown as triangles.

such as different temperature protocols applied in thermal optical techniques [17, 19, 20], and could be seasonally dependent due to different aerosol types [60]. This variability should be kept in mind when interpreting EC/OC ratios and comparing estimates from different studies.

The 2007–2010 seasonal mean EC/OC ratios are shown in Figures 7(a)–7(d). Urban “hot spots” in EC/OC ( $>0.6$ ) in winter, spring, and fall emphasized the impact of urban and mobile sources on significantly lower ratios in surrounding regions. Locations with high EC/OC ( $\sim 0.6$ ) were coincident with locations corresponding to high EC concentrations, especially in Colorado and Utah (winter, spring, and fall; see Figures 3(a)–3(d)), but not in locations with high POM, such as along the West coast and the San Joaquin valley (winter and fall; see Figures 1(a) and 1(d)), suggesting secondary sources to urban POM. The high EC/OC hotspots in the West were fairly local in extent and surrounded by background EC/OC ratios of 0.1–0.2 that were the lowest in summer, likely due to high biogenic contributions and possibly biomass burning influences. Similar results were reported by Schichtel et al. [25] for rural sites in summer and for ratios at urban sites that had somewhat higher ratios (0.24–0.28); both urban and rural ratios increased in winter.

In the eastern United States, EC/OC ratios were the lowest (0.1–0.2) in regions and seasons that corresponded to high POM, such as the Southeast in summer, suggesting secondary

sources. EC/OC ratios of 0.3–0.4 across the north-central and eastern United States year-round (with the exception of summer) suggested urban influences and were consistent with the higher EC/OC ratios corresponding to fossil carbon (0.54–0.85) [25]. The least seasonal variability in EC/OC ratios occurred in the Midwest, similar to the results reported by Zeng and Wang [64].

**3.4. Trends in Total Carbon (TC).** IMPROVE long-term trends (1990–2010) in seasonal mean TC are shown in Figures 8(a)–8(d). Sites with statistically significant trends ( $p < 0.10$ ) are represented with a filled triangle pointing upward or downward depending on whether TC concentrations increased or decreased, respectively. Sites with insignificant trends are represented by unfilled triangles. Trends in TC, and not EC and OC separately, are shown to avoid possible biases due to hardware upgrades, as discussed previously; however, trends in TC are driven predominantly by OC. Since 1990, seasonal mean rural TC concentrations decreased across the country in winter and spring (Figures 8(a) and 8(b), resp.), with the strongest decrease along the West coast. However, in summer and to a lesser degree in fall, trends in the West were positive at many sites, although insignificant. This is the season when wildfires are most active, and wildfire activity has increased in the West [53] and most likely contributed to the positive trends. A similar conclusion was suggested by

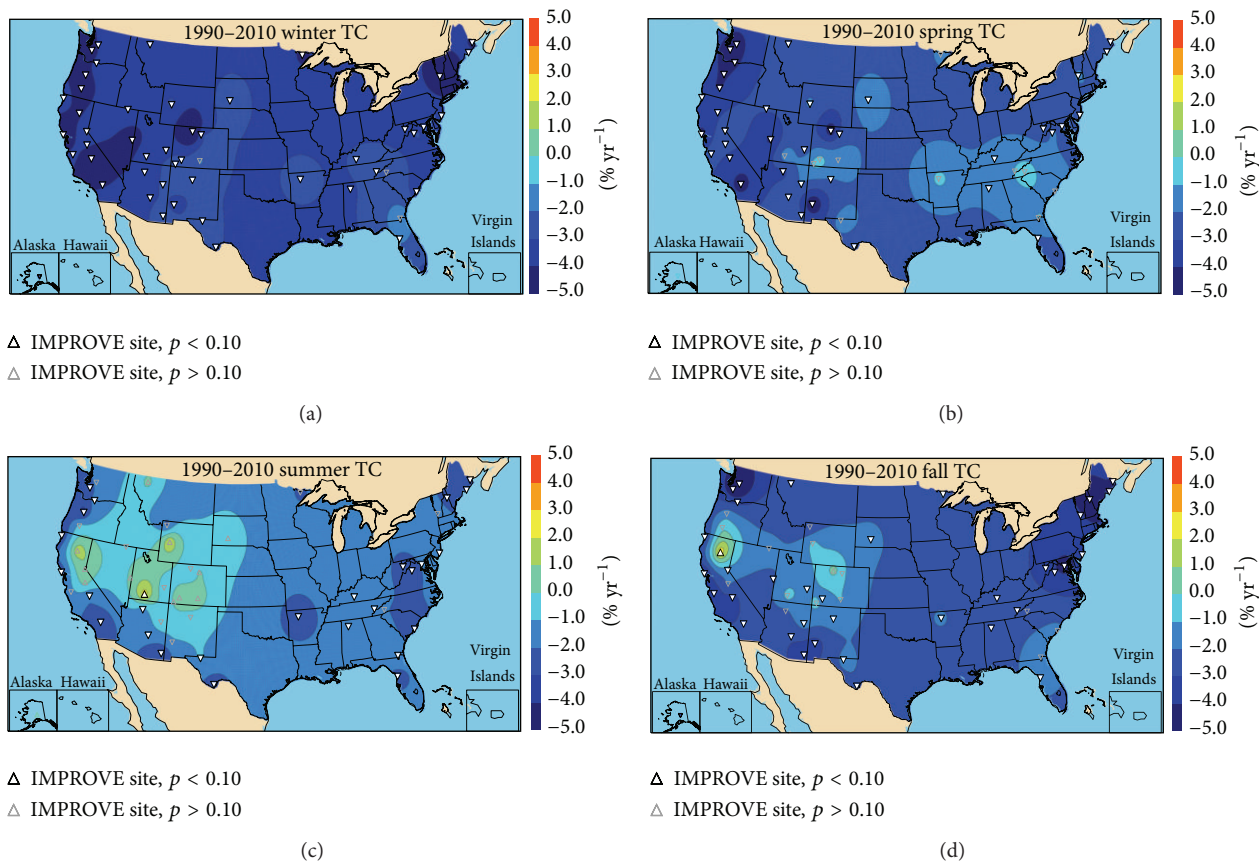


FIGURE 8: Long-term (1990–2010) trends ( $\% \text{ yr}^{-1}$ ) in IMPROVE seasonal mean  $PM_{2.5}$  total carbon (TC = OC + EC) for (a) winter (DJF), (b) spring (MAM), (c) summer (JJA), and (d) fall (SON). White triangles correspond to IMPROVE sites. Upward pointing triangles correspond to increased concentrations and vice versa. Trends with significance levels ( $p$ ) less than 0.10 were considered significant. (filled triangles). Unfilled triangles correspond to insignificant trends.

Murphy et al. [41] who reported positive trends in summer time EC concentrations at IMPROVE sites in the West.

Combining trends from urban and rural sites over a shorter time period (2000–2010) resulted in greater spatial variability relative to the long-term trends. Short-term trends in urban and rural seasonal mean TC are shown in Figures 9(a)–9(d). In general, TC decreased more strongly in the West ( $-4\%$  to  $-5\% \text{ yr}^{-1}$ ), with winter and spring seasons corresponding to the highest rates of decrease (Figures 9(a) and 9(b), resp.). The long-term positive trends in TC in the West in summer did not occur for the shorter time period, although most of the summer trends in the West were insignificant (Figure 9(c)). The least negative trends in the West occurred during the fall (Figure 9(d)), although many were insignificant. Although the rural site density in the West is greater than that for urban sites, it still appears that urban and rural TC short-term trends in the West are fairly spatially consistent.

In contrast, in the eastern United States, trends were generally more spatially inhomogeneous, with rural sites having statistically significant negative trends nearby urban sites with insignificant positive or negative trends depending on the season. Overall, TC did not decrease as strongly in the East relative to the West ( $-1\%$  to  $-2\% \text{ yr}^{-1}$ ), and a number of

urban sites experienced increased TC concentrations, such as in Iowa in winter, spring, and fall, and sites in New York year-round for reasons unknown. TC concentrations in winter and fall decreased at the strongest rates of all the seasons. Blanchard et al. [16] reported similar trends for annual mean OC and EC in the Southeast from sites in the SEARCH network. A thorough analysis of TC emission trends would help to reveal the cause of the spatial variability in urban and rural trends in the East; however, it is beyond the scope of this paper.

#### 4. Summary and Conclusions

We presented an overview of the spatial and temporal variability in organic and elemental carbon concentrations and their contribution to  $PM_{2.5}$  reconstructed fine mass from the rural IMPROVE network and the urban CSN for data aggregated from 2007 to 2010. Interpolating these data together provides large spatial patterns from which local and regional impacts of carbonaceous aerosols across the United States can be inferred.

Background rural/remote POM ( $= 1.8 * \text{OC}$ ) concentrations ranged from less than  $1 \mu\text{g m}^{-3}$  in the West to around  $2 \mu\text{g m}^{-3}$  in the East. High POM concentrations and

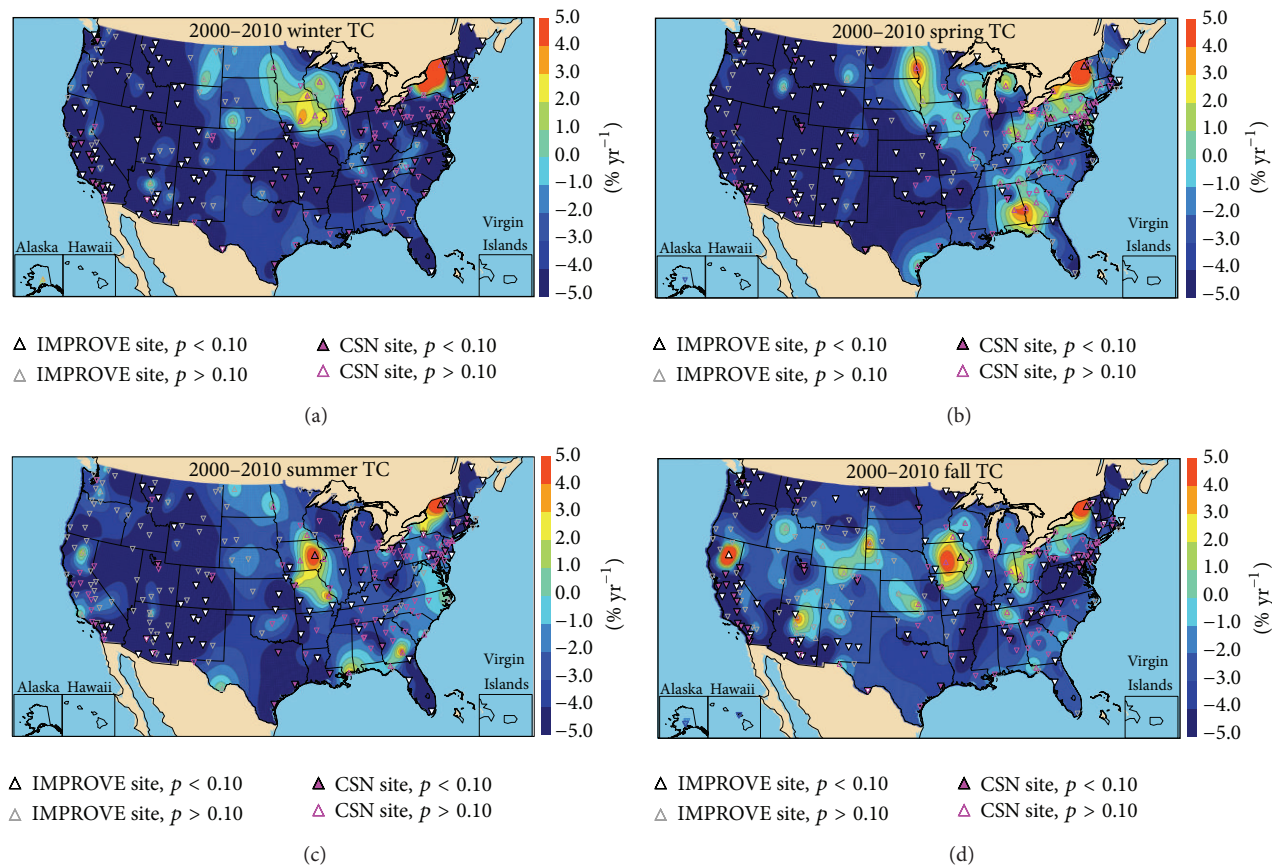


FIGURE 9: Short-term (2000–2010) trends ( $\% \text{ yr}^{-1}$ ) in IMPROVE and CSN seasonal mean PM<sub>2.5</sub> total carbon (TC = OC + EC) for (a) winter (DJF), (b) spring (MAM), (c) summer (JJA), and (d) fall (SON). White and magenta triangles correspond to IMPROVE and CSN sites, respectively. Upward pointing triangles correspond to increased concentrations and vice versa. Trends with significance levels ( $p$ ) less than 0.10 were considered significant. (filled triangles). Unfilled triangles correspond to insignificant trends.

contributions to RCFM up to 80% at both western urban and rural sites occurred during summer and fall when wildfires are most active. Urban impacts were the highest and more localized in the West in winter. Eastern POM concentrations were the highest in the Southeast in spring when prescribed fires occur, but less regional in extent compared to summer concentrations that were most likely influenced by secondary sources. Contributions in the East were typically less than 50% year-round.

Background EC concentrations were  $0.1\text{--}0.3 \mu\text{g m}^{-3}$  with lower values in the West. The influence of urban sources was significant ( $>10\times$  higher) but fairly localized with high concentrations and tight spatial gradients around individual cities (especially in the West in winter). A more regional influence was observed in the East, although this could be due in part to site density. The highest eastern concentrations occurred in the Southeast in fall. Contributions from EC were typically 10% or less at rural sites and somewhat higher at urban sites.

Normalized monthly mean POM and EC concentrations were examined as a function of broad urban and rural regions. Rural POM in the West was characterized by a large range in seasonality, with a summer maximum that was most likely influenced by biomass burning and biogenic

contributions. In contrast, urban POM in the West was characterized by winter maxima, although the influence of biomass burning in the summer can still be observed. Much of the western urban seasonality was probably due to meteorological effects such as low ventilation. In contrast, the seasonality in eastern rural and urban POM was fairly flat, with spring/summer maxima in the rural Southeast, likely associated with biomass burning and biogenic aerosols. The influence of secondary organic aerosols was inferred from the summer maxima in the urban and rural Northeast. Both urban and rural eastern regions experienced a peak in November. EC rural and urban seasonality in the East was also fairly flat, and demonstrated somewhat different seasonality to POM, with a rural minimum in summer and maximum in winter in the Southeast. EC rural and urban seasonality in the West followed that of POM, reflecting different primary sources and influence of meteorological conditions, such as winter temperature inversions that trap urban sources.

Rural TC (OC + EC) concentrations have decreased across the country from 1990 through 2010 for most seasons except for positive summer trends in the West that may be associated with biomass burning impacts. Short-term (2000–2010) trends in rural and urban concentrations were

associated with greater spatial inhomogeneity, with higher rates of decrease in TC in the West for all seasons and variable trends at nearby urban and rural sites in the East.

## Acknowledgments

This work was funded by the National Park Service under Contract no. H2370094000. The assumptions, findings, conclusions, judgments, and views presented herein are those of the authors and should not be interpreted as necessarily representing the National Park Service policies.

## References

- [1] J. L. Hand, B. A. Schichtel, M. Pitchford, W. C. Malm, and N. H. Frank, "Seasonal composition of remote and urban fine particulate matter in the United States," *Journal of Geophysical Research*, vol. 117, no. 5, Article ID D05209, 2012.
- [2] W. C. Malm, M. L. Pitchford, C. McDade, and L. L. Ashbaugh, "Coarse particle speciation at selected locations in the rural continental United States," *Atmospheric Environment*, vol. 41, no. 10, pp. 2225–2239, 2007.
- [3] E. S. Edgerton, G. S. Casuccio, R. D. Saylor et al., "Measurements of OC and EC in coarse particulate matter in the southeastern United States," *Journal of the Air & Waste Management Association*, vol. 59, no. 1, pp. 78–90, 2009.
- [4] G. R. McMeeking, S. M. Kreidenweis, M. Lunden et al., "Smoke-impacted regional haze in California during the summer of 2002," *Agricultural and Forest Meteorology*, vol. 137, no. 1–2, pp. 25–42, 2006.
- [5] J. L. Hand, S. A. Copeland, D. E. Day et al., "IMPROVE (Interagency Monitoring of Protected Visual Environments): spatial and seasonal patterns and temporal variability of haze and its constituents in the United States," CIRA Report 5, 2011, <http://vista.cira.colostate.edu/improve/Publications/Reports/2011/2011.htm>.
- [6] T. C. Bond and R. W. Bergstrom, "Light absorption by carbonaceous particles: an investigative review," *Aerosol Science and Technology*, vol. 40, no. 1, pp. 27–67, 2006.
- [7] A. H. Goldstein, C. D. Koven, C. L. Heald, and I. Y. Fung, "Biogenic carbon and anthropogenic pollutants combine to form a cooling haze over the southeastern United States," *Proceedings of the National Academy of Sciences of the United States of America*, vol. 106, no. 22, pp. 8835–8840, 2009.
- [8] J. L. Mauderly and J. C. Chow, "Health effects of organic aerosols," *Inhalation Toxicology*, vol. 20, no. 3, pp. 257–288, 2008.
- [9] A. C. Rohr and R. E. Wyzga, "Attributing health effects to individual particulate matter constituents," *Atmospheric Environment*, vol. 62, pp. 130–152, 2012.
- [10] T. C. Bond, S. J. Doherty, D. W. Fahey et al., "Bounding the role of black carbon in the climate system: a scientific assessment," *Journal of Geophysical Research*, vol. 118, no. 11, pp. 5380–5552, 2013.
- [11] R. A. Zaveri, W. J. Shaw, D. J. Cziczo et al., "Overview of the 2010 Carbonaceous Aerosols and Radiative Effects Study (CARES)," *Atmospheric Chemistry and Physics*, vol. 12, pp. 7647–7687, 2012.
- [12] W. C. Malm, J. F. Sisler, D. Huffman, R. A. Eldred, and T. A. Cahill, "Spatial and seasonal trends in particle concentration and optical extinction in the United States," *Journal of Geophysical Research*, vol. 99, no. 1, pp. 1347–1370, 1994.
- [13] U.S. Environmental Protection Agency, "PM<sub>2.5</sub> speciation network newsletter," Vol. 1, no. 1, 2004, <http://www.epa.gov/ttn/amtic/files/ambient/pm25/spec/spnews1.pdf>.
- [14] D. A. Hansen, E. S. Edgerton, B. E. Hartsell et al., "The Southeastern Aerosol Research and Characterization Study: part 1—overview," *Journal of the Air & Waste Management Association*, vol. 53, no. 12, pp. 1460–1471, 2003.
- [15] C. L. Blanchard, G. M. Hidy, S. Tanenbaum, and E. S. Edgerton, "NMOOC, ozone, and organic aerosol in the southeastern United States, 1999–2007: 3. Origins of organic aerosol in Atlanta, Georgia, and surrounding areas," *Atmospheric Environment*, vol. 45, no. 6, pp. 1291–1302, 2011.
- [16] C. L. Blanchard, G. M. Hidy, S. Tanenbaum, E. S. Edgerton, and B. E. Hartsell, "The Southeastern Aerosol Research and Characterization (SEARCH) Study: temporal trends in gas and PM concentrations and composition, 1999–2010," *Journal of the Air & Waste Management Association*, vol. 63, no. 3, pp. 247–259, 2013.
- [17] J. C. Chow, J. G. Watson, L. W. A. Chen, W. P. Arnott, H. Moosmüller, and K. Fung, "Equivalence of elemental carbon by thermal/optical reflectance and transmittance with different temperature protocols," *Environmental Science and Technology*, vol. 38, no. 16, pp. 4414–4422, 2004.
- [18] J. C. Chow, J. G. Watson, L.-W. A. Chen, J. Rice, and N. H. Frank, "Quantification of PM<sub>2.5</sub> organic carbon sampling artifacts in US networks," *Atmospheric Chemistry and Physics*, vol. 10, no. 12, pp. 5223–5239, 2010.
- [19] Y. Cheng, K.-B. He, F.-K. Duan et al., "Ambient organic carbon to elemental carbon ratios: influences of the measurement methods and implications," *Atmospheric Environment*, vol. 45, no. 12, pp. 2060–2066, 2011.
- [20] B. Khan, M. D. Hays, C. Geron, and J. Jetter, "Differences in the OC/EC ratios that characterize ambient and source aerosols due to thermal-optical analysis," *Aerosol Science and Technology*, vol. 46, no. 2, pp. 127–137, 2012.
- [21] O. V. Rattigan, H. D. Felton, M.-S. Bae, J. J. Schwab, and K. L. Demerjian, "Comparison of long-term PM<sub>2.5</sub> carbon measurements at an urban and rural location in New York," *Atmospheric Environment*, vol. 45, no. 19, pp. 3228–3236, 2011.
- [22] W. C. Malm, B. A. Schichtel, and M. L. Pitchford, "Uncertainties in PM<sub>2.5</sub> gravimetric and speciation measurements and what we can learn from them," *Journal of the Air & Waste Management Association*, vol. 61, no. 11, pp. 1131–1149, 2011.
- [23] D. Jaffe, W. Hafner, D. Chand, A. Westerling, and D. Spracklen, "Interannual variations in PM<sub>2.5</sub> due to wildfires in the western United States," *Environmental Science and Technology*, vol. 42, no. 8, pp. 2812–2818, 2008.
- [24] W. C. Malm, B. A. Schichtel, M. L. Pitchford, L. L. Ashbaugh, and R. A. Eldred, "Spatial and monthly trends in speciated fine particle concentration in the United States," *Journal of Geophysical Research*, vol. 109, no. 3, Article ID D03306, 2004.
- [25] B. A. Schichtel, W. C. Malm, G. Bench et al., "Fossil and contemporary fine particulate carbon fractions at 12 rural and urban sites in the United States," *Journal of Geophysical Research*, vol. 113, no. 2, Article ID D02311, 2008.
- [26] B. A. Schichtel, M. A. Rodriguez, M. G. Barna, K. A. Gebhart, M. L. Pitchford, and W. C. Malm, "A semi-empirical, receptor-oriented Lagrangian model for simulating fine particulate carbon at rural sites," *Atmospheric Environment*, vol. 61, pp. 361–370, 2012.
- [27] L.-W. A. Chen, J. G. Watson, J. C. Chow, D. W. DuBois, and L. Herschberger, "Chemical mass balance source apportionment

- for combined PM<sub>2.5</sub> measurements from U.S. non-urban and urban long-term networks,” *Atmospheric Environment*, vol. 44, no. 38, pp. 4908–4918, 2010.
- [28] B. Buzcu-Guven, S. G. Brown, A. Frankel, H. R. Hafner, and P. T. Roberts, “Analysis and apportionment of organic carbon and fine particulate matter sources at multiple sites in the mid-western United States,” *Journal of the Air & Waste Management Association*, vol. 57, no. 5, pp. 606–619, 2007.
- [29] S. Yu, R. L. Dennis, P. V. Bhawe, and B. K. Eder, “Primary and secondary organic aerosols over the United States: estimates on the basis of observed organic carbon (OC) and elemental carbon (EC), and air quality modeled primary OC/EC ratios,” *Atmospheric Environment*, vol. 38, no. 31, pp. 5257–5268, 2004.
- [30] A. Hecobian, X. Zhang, M. Zheng, N. Frank, E. S. Edgerton, and R. J. Weber, “Water-soluble organic aerosol material and the light-absorption characteristics of aqueous extracts measured over the southeastern United States,” *Atmospheric Chemistry and Physics*, vol. 10, no. 13, pp. 5965–5977, 2010.
- [31] X. Zhang, Z. Liu, A. Hecobian et al., “Spatial and seasonal variations of fine particulate water-soluble organic carbon (WSOC) over the southeastern United States: implications for secondary organic aerosol formation,” *Atmospheric Chemistry and Physics*, vol. 12, pp. 6593–6607, 2012.
- [32] M. Chin, T. Diehl, P. Ginoux, and W. Malm, “Intercontinental transport of pollution and dust aerosols: implications for regional air quality,” *Atmospheric Chemistry and Physics*, vol. 7, no. 21, pp. 5501–5517, 2007.
- [33] R. J. Park, D. J. Jacob, M. Chin, and R. V. Martin, “Sources of carbonaceous aerosols over the United States and implications for natural visibility,” *Journal of Geophysical Research*, vol. 108, no. 12, article 4355, 2003.
- [34] R. J. Park, D. J. Jacob, N. Kumar, and R. M. Yantosca, “Regional visibility statistics in the United States: natural and transboundary pollution influences, and implications for the Regional Haze Rule,” *Atmospheric Environment*, vol. 40, no. 28, pp. 5405–5423, 2006.
- [35] H. Liao, D. K. Henze, J. H. Seinfeld, S. Wu, and L. J. Mickley, “Biogenic secondary organic aerosol over the United States: comparison of climatological simulations with observations,” *Journal of Geophysical Research*, vol. 112, no. 6, Article ID D06201, 2007.
- [36] E. Drury, D. J. Jacob, R. J. D. Spurr et al., “Synthesis of satellite (MODIS), aircraft (ICARTT), and surface (IMPROVE, EPA-AQS, AERONET) aerosol observations over eastern North America to improve MODIS aerosol retrievals and constrain surface aerosol concentrations and sources,” *Journal of Geophysical Research*, vol. 115, no. 14, Article ID D14204, 2010.
- [37] Y. H. Mao, Q. B. Li, L. Zhang et al., “Biomass burning contribution to black carbon in the western United States mountain ranges,” *Atmospheric Chemistry and Physics*, vol. 11, no. 21, pp. 11253–11266, 2011.
- [38] M. Huang, G. R. Carmichael, S. Kulkarni et al., “Sectoral and geographical contributions to summertime continental United States (CONUS) black carbon spatial distributions,” *Atmospheric Environment*, vol. 51, pp. 165–174, 2012.
- [39] M. Kanakidou, J. H. Seinfeld, S. N. Pandis et al., “Organic aerosol and global climate modelling: a review,” *Atmospheric Chemistry and Physics*, vol. 5, no. 4, pp. 1053–1123, 2005.
- [40] X. Liu, R. C. Easter, S. J. Ghan et al., “Toward a minimal representation of aerosols in climate models: description and evaluation in the Community Atmosphere Model CAM5,” *Geoscientific Model Development*, vol. 5, pp. 709–739, 2012.
- [41] D. M. Murphy, J. C. Chow, E. M. Leibensperger et al., “Decreases in elemental carbon and fine particle mass in the United States,” *Atmospheric Chemistry and Physics*, vol. 11, no. 10, pp. 4679–4686, 2011.
- [42] L. W. A. Chen, J. C. Chow, J. G. Watson, and B. A. Schichtel, “Consistency of long-term elemental carbon trends from thermal and optical measurements in the IMPROVE network,” *Atmospheric Measurement Techniques*, vol. 5, pp. 2329–2338, 2012.
- [43] J. C. Chow, J. G. Watson, L. C. Pritchett, W. R. Pierson, C. A. Frazier, and R. G. Purcell, “The DRI thermal/optical reflectance carbon analysis system: description, evaluation and applications in U.S. Air quality studies,” *Atmospheric Environment*, vol. 27A, no. 8, pp. 1185–1201, 1993.
- [44] J. G. Watson, J. C. Chow, L.-W. A. Chen, and N. H. Frank, “Methods to assess carbonaceous aerosol sampling artifacts for IMPROVE and other long-term networks,” *Journal of the Air & Waste Management Association*, vol. 59, no. 8, pp. 898–911, 2009.
- [45] A. M. Dillner, C. H. Phuah, and J. R. Turner, “Effects of post-sampling conditions on ambient carbon aerosol filter measurements,” *Atmospheric Environment*, vol. 43, no. 37, pp. 5937–5943, 2009.
- [46] J. L. Hand, W. C. Malm, A. Laskin et al., “Optical, physical, and chemical properties of tar balls observed during the Yosemite Aerosol Characterization Study,” *Journal of Geophysical Research*, vol. 110, no. 21, Article ID D21210, pp. 1–14, 2005.
- [47] “IMPROVE data,” <http://vista.cira.colostate.edu/improve/>.
- [48] “CSN data,” <http://views.cira.colostate.edu/fed/> or <http://www.epa.gov/ttn/airs/airsaqs/>.
- [49] B. J. Turpin and H.-J. Lim, “Species contributions to PM<sub>2.5</sub> mass concentrations: revisiting common assumptions for estimating organic mass,” *Aerosol Science and Technology*, vol. 35, no. 1, pp. 602–610, 2001.
- [50] H. Theil, “A rank-invariant method of linear and polynomial regression analysis I,” in *Proceedings of the Koninklijke Nederlandse Akademie van Wetenschappen*, vol. A53, pp. 386–392, 1950.
- [51] H. Theil, “A rank-invariant method of linear and polynomial regression analysis II,” in *Proceedings of the Koninklijke Nederlandse Akademie van Wetenschappen*, vol. A53, pp. 521–525, 1950.
- [52] H. Theil, “A rank-invariant method of linear and polynomial regression analysis III,” in *Proceedings of the Koninklijke Nederlandse Akademie van Wetenschappen*, vol. A53, pp. 1397–1412, 1950.
- [53] D. V. Spracklen, J. A. Logan, L. J. Mickley et al., “Wildfires drive interannual variability of organic carbon aerosol in the western U.S. in summer,” *Geophysical Research Letters*, vol. 34, no. 16, Article ID L16816, 2007.
- [54] A. S. Holden, A. P. Sullivan, L. A. Munchak et al., “Determining contributions of biomass burning and other sources to fine particle contemporary carbon in the western United States,” *Atmospheric Environment*, vol. 45, no. 11, pp. 1986–1993, 2011.
- [55] J. C. Chow, L.-W. A. Chen, J. G. Watson et al., “PM<sub>2.5</sub> chemical composition and spatiotemporal variability during the California Regional PM<sub>10</sub>/PM<sub>2.5</sub> Air Quality Study (CRPAQS),” *Journal of Geophysical Research*, vol. 111, no. 10, Article ID D10S04, 2006.
- [56] S. A. Christopher, P. Gupta, U. Nair et al., “Satellite remote sensing and mesoscale modeling of the 2007 Georgia/Florida fires,” *IEEE Journal of Selected Topics in Applied Earth Observations and Remote Sensing*, vol. 2, no. 3, pp. 163–175, 2009.

- [57] X. Zhang, A. Hecobian, M. Zheng, N. H. Frank, and R. J. Weber, "Biomass burning impact on  $PM_{2.5}$  over the southeastern US during 2007: integrating chemically speciated FRM filter measurements, MODIS fire counts and PMF analysis," *Atmospheric Chemistry and Physics*, vol. 10, no. 14, pp. 6839–6853, 2010.
- [58] G. Bench, S. Fallon, B. Schichtel, W. Malm, and C. McDade, "Relative contributions of fossil and contemporary carbon sources to  $PM_{2.5}$  aerosols at nine Interagency Monitoring for Protection of Visual Environments (IMPROVE) network sites," *Journal of Geophysical Research*, vol. 112, no. 10, Article ID D10205, 2007.
- [59] L. Ke, X. Ding, R. L. Tanner, J. J. Schauer, and M. Zheng, "Source contributions to carbonaceous aerosols in the Tennessee valley region," *Atmospheric Environment*, vol. 41, no. 39, pp. 8898–8923, 2007.
- [60] Y. Cheng, M. Zheng, K.-B. He et al., "Comparison of two thermal-optical methods for the determination of organic carbon and elemental carbon: results from the southeastern United States," *Atmospheric Environment*, vol. 45, no. 11, pp. 1913–1918, 2011.
- [61] G. C. Holzworth, "Mixing heights, wind speeds, and potential for urban air pollution throughout the contiguous United States," Tech. Rep. AP-101, Environmental Protection Agency, Office of Air Programs Publication, 1972.
- [62] J. A. Gillies and A. W. Gertler, "Comparison and evaluation of chemically speciated mobile source  $PM_{2.5}$  particulate matter profiles," *Journal of the Air & Waste Management Association*, vol. 50, no. 8, pp. 1459–1480, 2000.
- [63] J. D. McDonald, B. Zielinska, E. M. Fujita, J. C. Sagebiel, J. C. Chow, and J. G. Watson, "Fine particle and gaseous emission rates from residential wood combustion," *Environmental Science and Technology*, vol. 34, no. 11, pp. 2080–2091, 2000.
- [64] T. Zeng and Y. Wang, "Nationwide summer peaks of OC/EC ratios in the contiguous United States," *Atmospheric Environment*, vol. 45, no. 3, pp. 578–586, 2011.
- [65] B. J. Turpin and J. J. Huntzicker, "Secondary formation of organic aerosol in the Los Angeles basin: a descriptive analysis of organic and elemental carbon concentrations," *Atmospheric Environment*, vol. 25A, no. 2, pp. 207–215, 1991.

## Research Article

# Comparison of Spheroidal Carbonaceous Particle Data with Modelled Atmospheric Black Carbon Concentration and Deposition and Air Mass Sources in Northern Europe, 1850–2010

Meri Ruppel,<sup>1,2</sup> Marianne T. Lund,<sup>3</sup> Henrik Grythe,<sup>4,5</sup> Neil L. Rose,<sup>6</sup>  
Jan Weckström,<sup>1</sup> and Atte Korhola<sup>1</sup>

<sup>1</sup> Department of Environmental Sciences, Environmental Change Research Unit (ECRU), P.O. Box 65, University of Helsinki FIN-00014, Helsinki, Finland

<sup>2</sup> Arctic Centre, University of Lapland, P.O. Box 122, 96101 Rovaniemi, Finland

<sup>3</sup> Center for International Climate and Environmental Research-Oslo (CICERO), P.O. Box 1129, Blindern, 0318 Oslo, Norway

<sup>4</sup> Department of Applied Environmental Science, Atmospheric Science Unit (ITM), Stockholm University, Svante Arrhenius Väg 8, 11418 Stockholm, Sweden

<sup>5</sup> NILU-Norwegian Institute for Air Research, P.O. Box 100, 2027 Kjeller, Norway

<sup>6</sup> Environmental Change Research Centre, Department of Geography, University College London, WC1E 6BT, UK

Correspondence should be addressed to Meri Ruppel; [meri.ruppel@helsinki.fi](mailto:meri.ruppel@helsinki.fi)

Received 8 March 2013; Accepted 9 July 2013

Academic Editor: Junji Cao

Copyright © 2013 Meri Ruppel et al. This is an open access article distributed under the Creative Commons Attribution License, which permits unrestricted use, distribution, and reproduction in any medium, provided the original work is properly cited.

Spheroidal carbonaceous particles (SCP) are a well-defined fraction of black carbon (BC), produced only by the incomplete combustion of fossil fuels such as coal and oil. Their past concentrations have been studied using environmental archives, but, additionally, historical trends of BC concentration and deposition can be estimated by modelling. These models are based on BC emission inventories, but actual measurements of BC concentration and deposition play an essential role in their evaluation and validation. We use the chemistry transport model OsloCTM2 to model historical time series of BC concentration and deposition from energy and industrial sources and compare these to sedimentary measurements of SCPs obtained from lake sediments in Northern Europe from 1850 to 2010. To determine the origin of SCPs we generated back trajectories of air masses to the study sites. Generally, trends of SCP deposition and modelled results agree reasonably well, showing rapidly increasing values from 1950, to a peak in 1980, and a decrease towards the present. Empirical SCP data show differences in deposition magnitude between the sites that are not captured by the model but which may be explained by different air mass transport patterns. The results highlight the need for numerous observational records to reliably validate model results.

## 1. Introduction

The term black carbon (BC) was first introduced by Novakov [1] and incorporates a wide spectrum of charred material formed by incomplete combustion of biomass and fossil fuels [2]. Generally, BC can be grouped into larger chars, which are aromatic residues reflecting the structure of the burned material or the nature of the burning process, and smaller particles, soots, which are combustion condensates formed in the vapour phase [1–5]. The precise definition of BC depends

on the method used for its quantification [6]; therefore, no single definition has been widely accepted, especially across disciplines.

However, within this imprecise myriad of carbonaceous particles, spheroidal carbonaceous particles (SCPs) are a clearly identifiable component of BC. SCPs are a component of fly ash and result only from the incomplete combustion of fossil fuels, mainly coal and oil, at high temperatures (greater than 1000°C) in heavy industry and energy production. They have no natural sources [7] and consist mainly of elemental

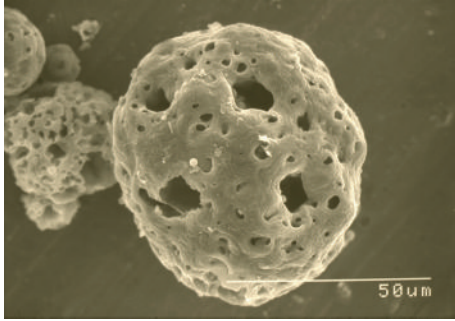


FIGURE 1: Scanning electron microscope picture of a spheroidal carbonaceous particle (picture by Neil Rose).

carbon making them chemically inert. Morphologically they are the spheroidal “skeletons” left by the incomplete combustion of fuel particles (coal) and droplets (oil) (see Figure 1). They thereby physically resemble char BC although their other characteristics are more typical of soot BC (highly refractory, chemically inert, and hydrophobic). The usual size range of SCPs in the environment is 2–20  $\mu\text{m}$  (diameter), but the largest particles can reach  $>50 \mu\text{m}$ . In remote areas only particles smaller than 10  $\mu\text{m}$  are found [8].

The atmospheric lifetime of BC particles smaller than 2.5  $\mu\text{m}$  is around a week [9], which should also be the case for the smallest SCPs, whereas particles of the size range of  $\geq 10 \mu\text{m}$  are probably transported only on a regional scale [10]. SCPs are removed from the atmosphere by wet or dry deposition and are abundant in urban areas close to industrial sources [11, 12]. However, they have been recorded even in remote areas such as Svalbard [13, 14], Greenland [15], the Canadian High Arctic [16], and Antarctica [17, 18] far removed from any local or regional emission sources. SCPs have been used for decades as a tracer for industrial combustion and pollution deposited from the atmosphere (e.g., [13]) and their spatial distribution is in good agreement with patterns of sulphur deposition [11, 12] as well as polycyclic aromatic hydrocarbon (PAH) distribution [19].

Examples of long-term monitoring of SCPs in the atmosphere are very few [20]. In the absence of long-term monitoring data, environmental archives, such as glacial ice, peat deposits, and lake and marine sediments, are the only means by which long-term trends of contaminant deposition can be ascertained. Accumulating sediments store direct evidence of atmospheric deposition of pollutants in chronological and conformable order thereby providing an *in situ* record of atmospheric contamination. Furthermore, SCPs strongly resist decomposition and therefore their sediment record is both robust and reliable [21].

In addition to sedimentary records of SCPs and BC, historical trends can also be estimated using models. Much of the understanding about the present and future impact of BC is based on modelling studies but, to be credible, models need to be evaluated and validated against historical data. Sedimentary records can supplement modeled data by providing spatial and temporal information on atmospheric contamination patterns. A few modelling studies

have explored the historical concentration of BC in the atmosphere using estimates of historical emissions [22–24]. These studies compare modelled BC concentrations to ice core records from Greenland [25–27] and show very good agreement with both temporal trends and magnitudes of the BC concentrations. In addition, Lee et al. [24] compare results of eight models [28] to eight ice cores from the Alps, Tibetan Plateau, and Antarctica. While models are able to capture the relative increase in BC from preindustrial times to the present in the Antarctic ice cores, they fail to reproduce the temporal trends from Tibetan Plateau records. This shows that good agreement between modelled and empirical data in one location cannot necessarily be expected in others for the same model. Hence, comparisons of models with observational data require large spatial coverage. Records from single locations may also include characteristics that prohibit upscaling. For example, McConnell et al. [25] recognized that their Greenland ice cores mainly represented emissions from North America and, located in the free troposphere (ca. at 2500 m asl), did not reflect BC deposition at sea level altitudes.

Current estimates rank BC as the second most important contributor to climate warming with a total climate forcing of  $+1.1 \text{ W m}^{-2}$  ( $+0.17$  to  $+2.1 \text{ W m}^{-2}$ ). It has an especially strong climate warming efficiency in the Arctic where BC aerosols can significantly reduce the albedo when deposited on snow covered surfaces (see [29] and references therein). Until recently, measurements of past BC concentrations and deposition have been scarce, and with the exception of the ice core records of McConnell et al. [25, 26] no long-term records of total BC or EC (elemental carbon) exist from the Arctic. However, historical SCP records have been studied in Arctic regions [13–16, 30].

This paper focuses on arctic Europe since a number of SCP records were available within a small geographical area, and although remote, the area is of special interest due to the nearby industrialized area on the Kola Peninsula, Russia. Also, the European sector is clearly the area with highest elemental carbon (EC) concentrations measured from modern snow in the Arctic [31] and is therefore an important area with respect to Arctic climate change.

The ultimate objective of this paper is to use direct sedimentary records to provide support for models reconstructing historical BC concentrations. Accurate measurements of SCP trends in remote locations, enabled by the sedimentary records, will help improve models to better capture the large spatial and temporal variations in BC, informing climate science, health, and policy. We use the chemistry transport model OsloCTM2 (e.g., [22, 32, 33]) to model historical time series of BC concentration and deposition from energy and industrial sources and compare these to sedimentary measurements of SCPs to show the usefulness of sedimentary data in the validation and possible improvement of models. In addition to the evolution of industrial and energy emissions, the SCP record is also a manifestation of variation in precipitation and wind direction patterns. We therefore generate back trajectories of air masses from the study sites. This information may provide data on the origin

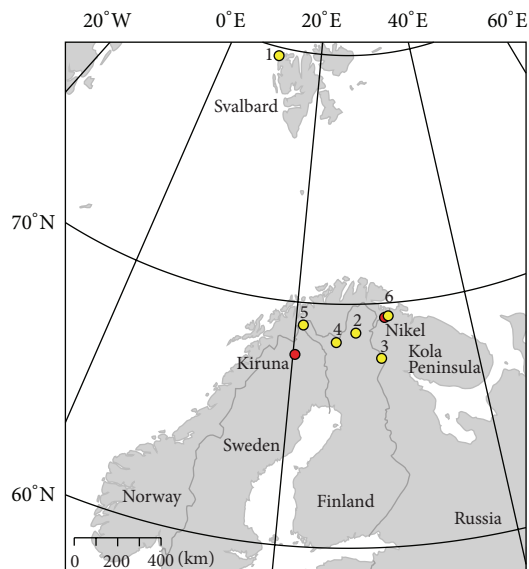


FIGURE 2: Location of lake coring sites and nearby large emission sources, Kiruna (Sweden) and Nikel (Kola Peninsula, Russia). The numbers refer to the study lakes listed in Table 1.

of the deposited material at each site and the likely sources of SCPs. In addition, analysis of transport patterns over time may disentangle whether changes in SCP deposition could have been caused by possible trends in transport.

## 2. Material and Methods

### 2.1. SCP Data

**2.1.1. Study Sites and Sample Collection.** In order to determine the past concentration and deposition of SCPs in the European Arctic, lake sediments were collected from six sites in arctic and subarctic Europe (Figure 2 and Table 1). The four lakes in Finland and one on Svalbard were chosen because they are remote from sources and have no direct human impact and therefore their SCP records are not dominated by local sources. By contrast, the lake on the Kola Peninsula was selected in order to provide a site near major emission sources in the Arctic. This lake is situated ~20 km northeast of Nikel, a small town supporting a large nickel, palladium, and copper mine and smelter. In addition to Nikel, only an iron mine in Kiruna, Sweden, presents a possibly significant emission source for SCPs in the region.

In general the lakes are small and have simple bathymetries. The sediments were collected from the deepest part of the sediment accumulation area. The uppermost 10–20 cm of sediment representing ca. the last two centuries were collected with an HTH gravity corer [34] or a Glew corer [35]. The sediments from three sites in Finland were retrieved in 2009 and 2010 (Kuutsjärvi, Puoltsajärvi, and Karipääjärvi), whereas the other sediments were collected in 1992 (Stapanovichjarvi), 1993 (Arresjøen), and 1995 (Saanajärvi). The sediments were subsampled at high-resolution intervals: 0.2 cm for Saanajärvi; 0.25 for the other

Finnish lakes, and Arresjøen and 0.5 cm for Stepanovichjarvi, and stored in plastic bags. The sediments were freeze-dried prior to analysis.

**2.1.2. Radiometric Dating.** Sediment cores were dated radiometrically. Lead-210 (half-life 22.3 years) is a naturally produced radionuclide, derived from atmospheric fallout (termed unsupported  $^{210}\text{Pb}$ ). Cesium-137 (half-life 30 years) and  $^{241}\text{Am}$  are artificially produced radionuclides, introduced to the study areas by atmospheric fallout from nuclear weapons testing and nuclear reactor accidents. Dried sediment samples were analysed for  $^{210}\text{Pb}$ ,  $^{226}\text{Ra}$ ,  $^{137}\text{Cs}$ , and  $^{241}\text{Am}$  by direct gamma assay using ORTEC HPGe GWL series well-type coaxial low background intrinsic germanium detectors. Lead-210 was determined via its gamma emissions at 46.5 keV, and  $^{226}\text{Ra}$  by the 295 keV, and 352 keV gamma rays emitted by its daughter isotope  $^{214}\text{Pb}$  following three weeks storage in sealed containers to allow radioactive equilibration. Cesium-137 and  $^{241}\text{Am}$  were measured by their emissions at 662 keV and 59.5 keV, respectively [36]. The absolute efficiencies of the detector were determined using calibrated sources and sediment samples of known activity. Corrections were made for the effect of self-absorption of low energy gamma rays within the sample [37]. This method allows sediment chronologies to be produced for the most recent ca. 150 years. The sediment of Saanajärvi, Kuutsjärvi, Karipääjärvi, and Arresjøen was analysed in the Liverpool University Environmental Radioactivity Laboratory and the sediment of Puoltsajärvi in the Environmental Radiometric Facility at University College London. The sediment of Stepanovichjarvi on the Kola Peninsula was not dated.

**2.1.3. SCP Analysis.** SCPs were extracted following the method developed by Rose [38]. The sediments were subjected to sequential chemical attack using  $\text{HNO}_3$ , HF, and HCl to remove organic material, silicates, and carbonates, respectively. Microscope slides with a known fraction of the resulting concentrated suspension of mainly carbonaceous material were made. The number of SCPs was counted under a light microscope at 400 times magnification. The detection limit of the method is 50–80 SCPs per gram dry mass ( $\text{g DM}^{-1}$ ) with a mean recovery of 95.2% [38]. Identification criteria for SCP counting are described in Rose [39].

The concentrations of SCPs in the sediment were calculated as “number of particles per gram dry mass of sediment” ( $\text{g DM}^{-1}$ ). The flux of SCPs to the sediment was calculated as “number of SCPs per square metre per year” ( $\text{SCP m}^{-2} \text{yr}^{-1}$ ) for all lakes that were dated and the sediment accumulation rate known. The weight of a medium sized (20  $\mu\text{m}$ ) SCP has been estimated to be  $1.96 \times 10^{-9} \text{g}$  [21]. This estimation was used to calculate the flux of the SCPs as “gram per square metre per year” ( $\text{g m}^{-2} \text{yr}^{-1}$ ).

### 2.2. Modeling Experiments

**2.2.1. The OsloCTM2.** OsloCTM2 is a global off-line 3-dimensional chemistry transport model with transport

TABLE 1: Details on the study lakes.

| Number (in Figure 2) | 1                   | 2                   | 3                   | 4                   | 5                   | 6                   |
|----------------------|---------------------|---------------------|---------------------|---------------------|---------------------|---------------------|
| Lake                 | Arresjøen           | Karipääjärvi        | Kuutsjärvi          | Puoltsajärvi        | Saanajärvi          | Stepanovichjarvi    |
| Location             | 79°40'N,<br>10°45'E | 68°49'N,<br>26°52'E | 67°45'N,<br>29°37'E | 68°26'N,<br>24°41'E | 69°05'N,<br>20°52'E | 69°28'N,<br>30°40'E |
| Altitude (m a.s.l.)  | 15                  | 265                 | 341                 | 355                 | 679                 | 200                 |
| Size (ha)            | 34                  | 32                  | 0.67                | 17                  | 70                  | Unknown             |
| Maximum depth (m)    | 31                  | 6.7                 | 8.6                 | 7                   | 24                  | 14                  |
| Coring year          | 1993                | 2010                | 2009                | 2010                | 1995                | 1992                |

driven by meteorological data generated by the Integrated Forecast System (IFS) model at the European Center for Medium Range Weather Forecast (ECMWF). The horizontal resolution is  $2.8^\circ \times 2.8^\circ$  and there are 60 vertical layers from the surface to 0.1 hPa. The advection of tracers in the model is calculated by the second order moment method [40]. Vertical mixing is based on Tiedtke [41] and the turbulent mixing in the boundary layer is treated following the Holtslag K-profile scheme [42].

Time-slice simulations for 1850 and for every 10th year from 1900 to 2010 are performed using meteorological data for 2006. For the purpose of our study we focused only on BC in the model runs. Historical anthropogenic and biomass burning emissions are from Lamarque et al. [23], while anthropogenic emissions for 2010 are from the Representative Concentration Pathway 4.5 [43]. These emissions are consistent with the historical inventory by Lamarque et al. [23]. Biomass burning emissions for 2000 are used for 2010. SCPs have limited emission sources and for the best possible comparison of modelled BC and measured SCP, we perform additional simulations where all BC emissions other than those from energy and industrial sectors are switched off.

The carbonaceous aerosols are parameterized using a bulk scheme based on Cooke et al. [44]. BC particles are assumed to be 20% hydrophilic and 80% hydrophobic upon emission. Conversion from hydrophobic to hydrophilic mode, where particles are assumed to be hygroscopic and available for wet removal, is given by constant aging times depending on latitude and season [22]. This aerosol aging scheme is based on results using the full tropospheric chemistry version of the OsloCTM2 with the microphysical aerosol module M7 [32] and is an improvement on the traditional approach of using one constant exponential lifetime to represent aging. The M7 [45] allows for a more realistic representation of aerosols than the bulk scheme by including size distribution and mixing state and allowing for aging and growth by particle interaction. BC aerosols are aged through coating by condensation and coagulation of sulfate and aging thus varies seasonally and regionally depending on the availability of sulfate. Using M7 leads to significant differences in BC distribution and lifetime [32] compared to the bulk scheme. However, simulations with the M7 in the OsloCTM2 are very demanding in terms of computing resources and do not allow separation of energy/industry BC from the total and are hence not used in this study.

Particles are removed by dry deposition and large-scale and convective precipitation. The dry deposition velocity for hydrophilic particles is  $0.025 \text{ cm s}^{-1}$  over land and  $0.2 \text{ cm s}^{-1}$  over ocean [44]. For hydrophobic aerosols a velocity of  $0.025 \text{ cm s}^{-1}$  is applied over all surfaces. Hydrophilic aerosols are removed according to the fraction of liquid plus ice water content of a cloud that is removed by precipitation. Aerosols are assumed to be 100% absorbed in cloud droplets for convective precipitation. For large-scale precipitation, 100% scavenging is assumed for liquid clouds and 12% for ice clouds [22].

*2.2.2. Back Trajectories.* To further explore the major source areas for SCPs and potential changes in the dominant transport patterns over the past decades, we calculated back trajectories of air masses to the study sites. Back trajectories were used to investigate air mass histories at all study sites, except Stepanovichjarvi, for which there is no information on depositional fluxes of SCP. The back trajectories were made with FLEXPART [46], a Lagrangian Particle Dispersion Model (LPDM). Trajectories tracing the air were run from each of the study sites. The model computes trajectories of particles in the atmosphere following the mean flow and random motion in order to take turbulence into account. Turbulence is parameterized as Gaussian and solved using the Langevin equations [47]. The model has been applied and validated in a wide range of aerosol studies on several scales, including volcanic ash [48], power plant plumes [49], and arctic transport [50].

For the period from January 2000, the model was driven by operational reanalysis of wind fields from ECMWF, with analyses at 00, 06, 12, and 18 UTC and three-hour intermediate forecasts. The horizontal resolution of the fields used was  $1^\circ$  by  $1^\circ$  with 91 vertical levels [51]. For the period 1983–2000, ECMWF ERA-40 reanalysis [52] data with the same horizontal and temporal resolution and 61 vertical levels were used to drive the model.

At each study site 25,000 trajectories were started in the boundary layer each day in the period 1983–2007, each trajectory running back in time for seven days. The years 1990 and 1999 missed input data from wind fields and are therefore excluded from the analysis. The model has daily output with a spatial resolution of  $1^\circ$  by  $1^\circ$  and is a count of the time spent in each grid cell by the tracer trajectories. This provides sufficient statistics on movements of the air

masses before reaching the study sites, thereby providing a 25-year record of transport to each site. The trajectories were run as air tracers and thus no atmospheric loss processes were taken into account, since such specific information is not available for SCPs. The wide spread in sizes for the SCPs makes different loss processes important. For the larger SCPs ( $r_d = 10\text{--}50\ \mu\text{m}$ ) gravitational settling is increasingly important with size and weight, while for smaller particles wet/dry deposition dominates.

Using air tracing trajectories will not provide information when, in the air mass history, emissions of SCP are significant. Losses during transport will deplete a source's importance relative to an air tracer with increasing transport time. Also, for SCPs that are relatively large particles, gravitation is influential and the path of a SCP in the atmosphere may deviate from that of an air tracer. Consequently, the air tracers will not give direct information on SCP sources but are rather a measure of where the air has been and thus where potential sources of SCPs may be located.

### 3. Results and Discussion

**3.1. The SCP Record in Lake Sediments.** SCP accumulation data has been previously published for Saanajärvi [53], Arresjøen, and Stepanovichjärvi [30], whereas the results for Kuutsjärvi, Karipääjärvi, and Puoltsajärvi are presented here for the first time (Figure 3). The older sediment records are used in this study for comparative purposes. The radiometric dating of the sediments provides chronologies with typical uncertainties of  $\pm 0\text{--}5$  years in recent decades, but uncertainties increase in older sediments reaching  $\pm 20$  years in the 19th century.

The SCP concentration profiles in the study lakes are generally in good agreement with previous trends across Europe (e.g., [54]). The first signs of SCP deposition in this study were recorded in Saanajärvi, Finland, in the 1870s, but not until the 1910s in the other Finnish lakes. These differences might be caused by analytical detection limits at low SCP concentrations and possible dating errors. On Svalbard SCP concentrations only exceeded the detection limit for the first time in the 1960s. With the exception of Saanajärvi the SCP concentrations initially increased quite moderately and more rapidly after the 1950s in common with many other European lakes. This trend is explained by a post-war expansion in the power generation industry in Europe and by the widespread usage of fuel-oil in power stations for the first time [54]. Coincidentally the smelter at Nikel also started operation in 1946 [55], suggesting that the earlier SCPs recorded in the study lakes may originate from either smaller scale regional activity or long-range transport. Peak values in SCP concentrations in all the dated sediment profiles were reached around the 1980s. Maximum concentrations for the Finnish lakes are 1400–3000 particles  $\text{g DM}^{-1}$ , and a little less for Arresjøen on Svalbard (ca. 1200 SCP  $\text{g (DM}^{-1})$ ). These concentrations are consistent with results from comparable sites, for example, Wik and Renberg [11] typically found concentrations of 100–2000 SCP  $\text{g (DM}^{-1})$  in northern Sweden in surface sediments in the late 1980s and Rose et al. [13] found

concentrations of 200–1000 SCP  $\text{g (DM}^{-1})$  in numerous surface sediments collected in Svalbard in 1995. In our study lakes SCP concentrations decreased from peak values, such that concentrations in 2010 were similar to those in the early 1950s. The peak in the 1980s and subsequent decrease of SCP concentration is most likely explained by clean air legislation and improved particle arrestor technology. In the Finnish lakes the start of the decrease of SCP concentrations seems to also coincide with the fall of the USSR in 1991.

Stepanovichjarvi on the Kola Peninsula shows significantly higher concentrations (up to 12000 SCP  $\text{g DM}^{-1}$ ). The overall shape of the SCP concentrations is similar to the other lakes. It is thus likely that the peak values of SCP concentrations were also reached in the 1980s. The prevailing wind patterns arrive at Stepanovichjarvi from the south west so it is situated downwind from the smelter in Nikel and received high contamination deposition. The high SCP concentrations for this region are supported by concentrations of  $>8000$  SCP  $\text{g DM}^{-1}$  in 1980 found in a northeastern Finnish lake ca. 40 km west of the Nikel smelter area [56].

SCP concentrations in lake sediments cannot be converted to concentrations for the atmosphere over the study area, since they are always influenced by sedimentary processes. However, converting SCP sediment concentrations to depositional fluxes facilitates a better comparison with modelled BC deposition.

**3.2. SCP Deposition and Comparison with Modelled BC Deposition.** Figure 4(a) shows the depositional fluxes of SCPs to the lakes and takes into account changes in the sediment accumulation rate. The sediment accumulation rates vary according to the input of both allochthonous organic and inorganic material and autochthonous biogenic material. SCP deposition is also shown on a decadal basis (Figure 4(b)) to provide similar results to the modelled time slices.

In general trends in SCP depositional fluxes differ from observed sediment concentrations due to higher sediment accumulation rates in some lakes. This is evident when comparing the SCP concentration (Figure 3) and flux profiles (Figure 4(a)) of Saanajärvi and Kuutsjärvi, respectively. In Saanajärvi (Figure 4(a)) conversion to depositional fluxes emphasises the 1980s peak with respect to concentration data (Figure 3). By contrast, in Kuutsjärvi SCP flux is higher in the late 1980s and 1990s (Figure 4(a)). In the other lakes trends in concentrations seem to show good agreement with flux rates which is explained by relatively constant sediment accumulation rates.

Although the SCP concentrations (Figure 3) were quite similar in the Finnish lakes some of the depositional flux values differ quite dramatically. In Karipääjärvi and Puoltsajärvi SCP fluxes were low and reached only ca.  $0.15\ \text{mg m}^{-2}\ \text{yr}^{-1}$ , whereas in Kuutsjärvi it was more than twice as high and in Saanajärvi almost an order of magnitude higher ( $0.9\ \text{mg m}^{-2}\ \text{yr}^{-1}$ ) (Figure 4(a)). In Arresjøen, on Svalbard, the SCP depositional flux was the lowest which is expected due to its remoteness. However despite these differences in scale of contaminant inputs to the lake sediments, temporal patterns are similar.

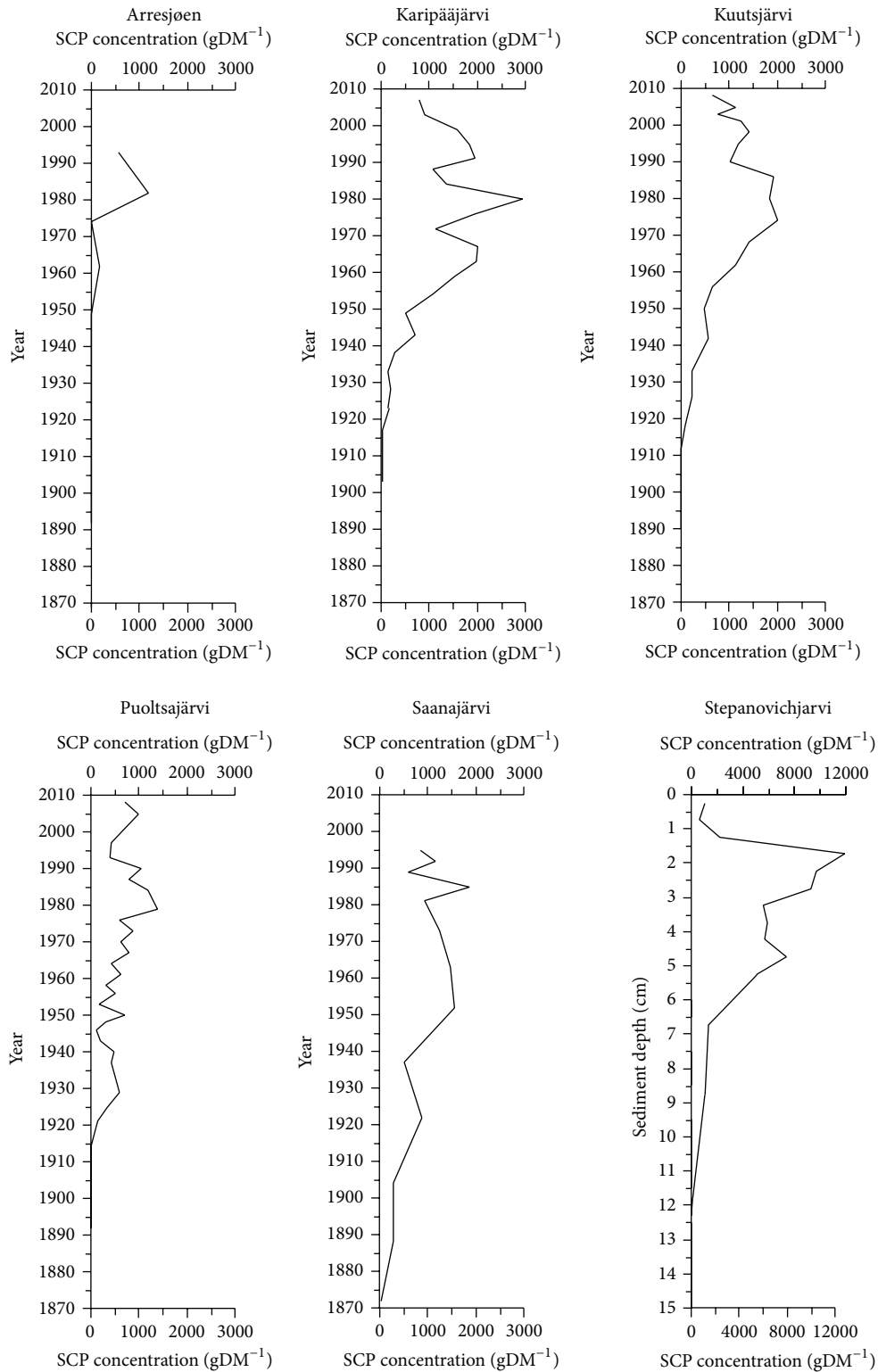


FIGURE 3: SCP concentration profiles for dated sediments taken from Arresjøen, Svalbard, Kuutsjärvi, Karipääjärvi, Puoltsajärvi, and Saanajärvi from Finland and Stepanovichjarvi on the Kola Peninsula. Note that the Stepanovichjarvi profile is given on a sediment depth axis since the core is not dated and that it has a larger scale on the x-axis than the other lakes.

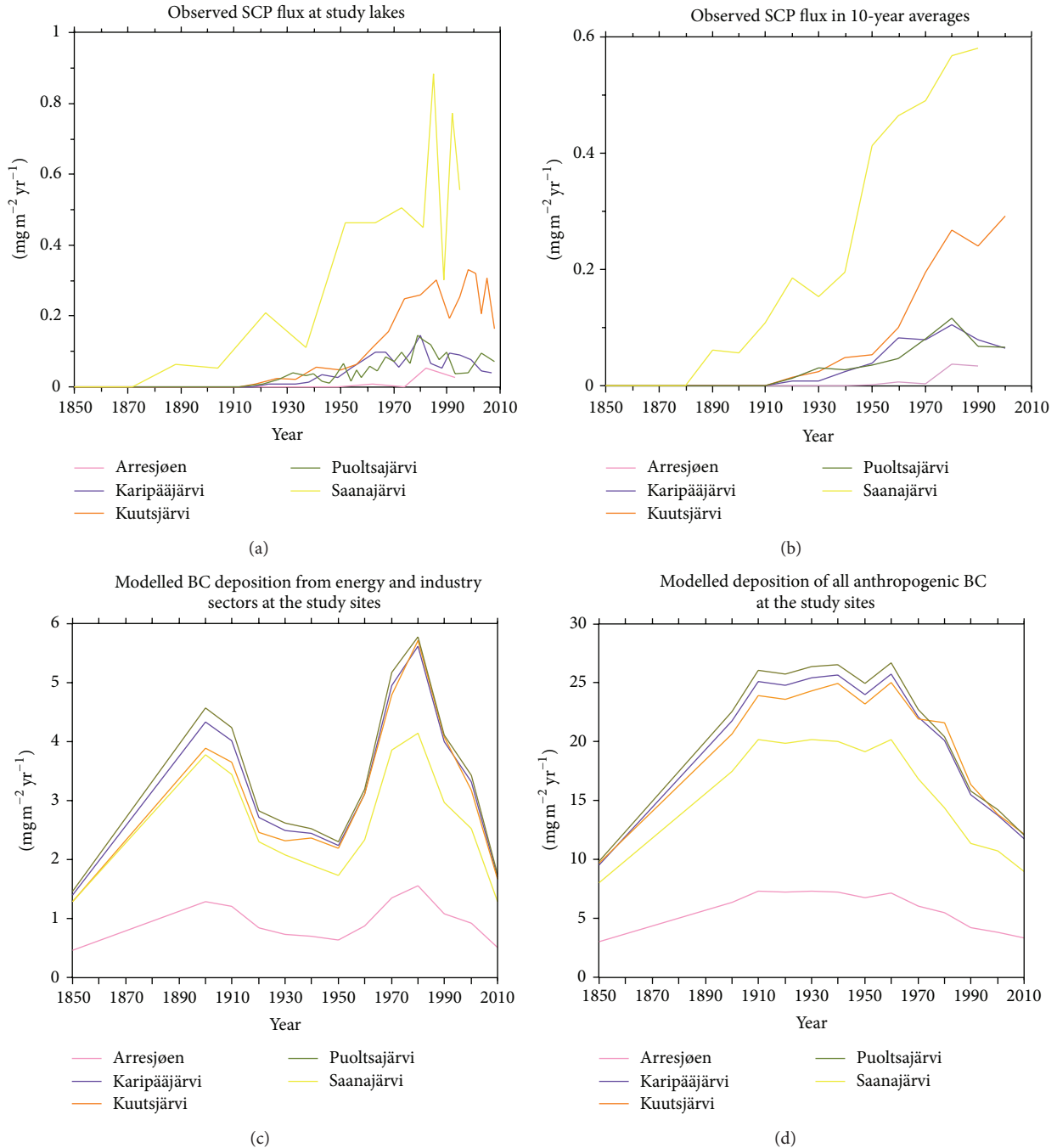


FIGURE 4: Observed depositional fluxes of SCP and modelled BC deposition at the study sites from 1850 to 2010. Results are given in milligrams per square meter per year ( $\text{mg m}^{-2} \text{ yr}^{-1}$ ). (a) SCP depositional flux for the five dated study lakes, (b) SCP depositional flux for the lakes in 10-year averages, (c) modelled time slice simulations of BC deposition from the industry and energy sectors at the study lakes, and (d) modelled time slice simulations of all anthropogenic BC deposition at the study lakes. The model results for 1850 to 1900 are linear interpolations. The SCP deposition results are also linear interpolations between dated observations. Note that the y-axes are not the same in all panels.

As with the concentration data, all lakes show a peak in SCP flux around 1980 and this peak is also clearly apparent in the 10-year averages (Figure 4(b)). Kuutsjärvi and Saanajärvi are an exception from the other lakes as they show no decline after 1980. This is apparently due to differences in coring date and the fact that in most cases the last available deposition

observation in the records falls outside the last full 10-year period used for averaging and thus the most recent trend is not seen in Figure 4(b).

Figure 4 also shows the modelled deposition of BC at each of the lakes. In Figure 4(c) the results are shown for BC deposition resulting from the industrial and energy sectors

whereas in Figure 4(d) deposition from all anthropogenic sources is shown. Model values are interpolated between the four grid boxes closest to each of the study lakes. Values of BC deposition resulting from the industrial and energy sectors (Figure 4(c)) are mostly of the order of 2 to 5 mg m<sup>-2</sup> yr<sup>-1</sup> for the four lakes in northern Finland. The model resolution is quite coarse (approx. 100 km × 100 km in the horizontal) and since the lakes are relatively close together the model is not capable of capturing significant variability between them. At Arresjøen, which is more remote, model values are around 0.50–1.5 mg m<sup>-2</sup> yr<sup>-1</sup> (Figure 4(c)).

Deposition rates for BC from industrial and energy sectors are much higher than the measured SCP depositional fluxes. SCPs make up only part of the emissions from energy and industry, while modelled BC is more representative of elemental carbon (EC). Comparing the magnitude of deposition is therefore not possible without an estimate of the fraction of SCPs in BC emissions. To the best of our knowledge, Muri et al. [57] is the only study to include both SCP and soot BC deposition in the same lakes. The soot BC was measured with the chemothermal oxidation method [58, 59], which probably represents EC measured in atmospheric studies quite well. Based on these results and assuming a mass of  $1.96 \times 10^{-9}$  g for a medium (20 μm) sized SCP, it can be estimated that SCPs make up 0.01–2.66% of total BC in these studied sediments. However, this value is highly variable in time and space and is based on only one study. Our study indicates that SCPs might represent approximately ≤5% of the modelled BC from the industrial and energy sectors and therefore, despite some assumptions, modelled and measured deposition would appear to agree quite well at several sites. Saanajärvi has a much higher measured depositional flux value than the other Finnish lakes, which may be explained by different transportation routes (see below).

Due to this limited knowledge about the fraction of SCP of total BC, we focus more on the temporal evolution in deposition rates than on their magnitudes. The general trends (Figures 4(a), 4(b) and 4(c)) seem to agree reasonably well. The measured peak in SCP deposition in 1980 (Figures 4(a) and 4(b)) is captured very well in the modelled time series of BC deposition (Figure 4(c)). After 1980, modelled deposition of BC from industrial and energy sectors declines significantly, to 1850 levels. Sediment data also show a decrease in this period but less significantly than the modelled data. The rapid increase leading up to the 1980 peak starts in 1950 in the model, which also agrees well with the SCP measurements. However, in the first part of the 20th century, modelled deposition of industrial and energy combustion derived BC reveals a local maximum around 1900 followed by a decrease until 1940 (Figure 4(c)). The increase from 1850 to the local maximum in 1900 is not seen in any of the lake sediments although they are analysed for SCP back to ca. 1850. This could suggest that the estimated energy and industrial emissions might be too high in the late 19th and early 20th centuries and uncertainties in regional BC emissions may be expected to be as large as a factor of two [23, 60, 61]. Furthermore, differences may arise due to the spatial distribution of emissions or

the transport from emission source to the study lakes in the model. However, the most plausible explanation for the divergence is that the BC peak in 1900 depicted by the model represents other forms of BC than SCP as combustion in the energy and industrial sector in the early 20th century did not always reach the temperatures required for SCP formation. This inference is supported by measurements of high refractory soot BC and pyrolysis-derived contaminant polycyclic aromatic hydrocarbons (PAH) in a lake sediment core from southern Sweden, ca. 1100 km southwest from the study area [62]. The 700-year record shows maximum soot BC and rapidly increasing PAH fluxes to the sediment in 1922–1928 in an area that might at least in part have same source areas for smaller, long-range transported particles as our Finnish study sites (see also Figure 6).

BC deposition from all anthropogenic emissions is shown in Figure 4(d). Both trends and magnitudes (values between 10 and 25 mg m<sup>-2</sup> yr<sup>-1</sup>, but lower for Arresjøen) are completely different than for the SCP and modelled industrial and energy sector derived BC deposition. This is probably mainly due to domestic combustion dominating the development of anthropogenic BC emissions, that is, much of the difference between total anthropogenic BC emissions and the industrial and energy sector seen in Figure 5(a) represents the domestic sector. The BC deposition for all anthropogenic BC (Figure 4(d)) seems to have increased at the study sites until 1900, stayed quite constant until 1960, and declined subsequently reaching almost preindustrial levels at present. This trend clearly illustrates the importance of choosing appropriate BC components when validating comparative studies between observed and modelled results.

As explained earlier, the changes in modelled deposition are governed by changes in emissions since we use constant meteorology in the model simulations. Figure 5(a) shows the time series of global annual BC emissions in the model from 1850 to 2010 for the energy and industrial sectors. For comparison we also show the total anthropogenic BC emissions. There is a continuous increase in emissions after 1950. However, the modelled deposition shows a significant decline in deposition at the measurement sites after 1980, despite the increase in emissions. This is explained by the geographical shift in major emission source regions. Figure 5(b) shows zonal mean distribution of energy and industrial emissions for selected years. There has been a significant southward shift in maximum emissions from 50–60°N towards 30°N during the industrial era. While emissions in Europe and North America have declined in the last decades of the 20th century, they have increased strongly in developing countries like China and India, although emissions from these regions are expected to have contributed little to the BC deposition in Finland and Svalbard [32, 63].

Modelled surface concentrations of BC at the study sites are shown in Figure 5(c) and exhibit the same trend as deposition. Concentrations range from 5 to 25 ng m<sup>-3</sup> during 1850–2010 at the Finnish lakes and 1–4 ng m<sup>-3</sup> at Arresjøen. Comparison of present-day surface concentrations of BC from the OsloCTM2 with observed data shows a reasonable agreement at Pallas (northern Finland, close to

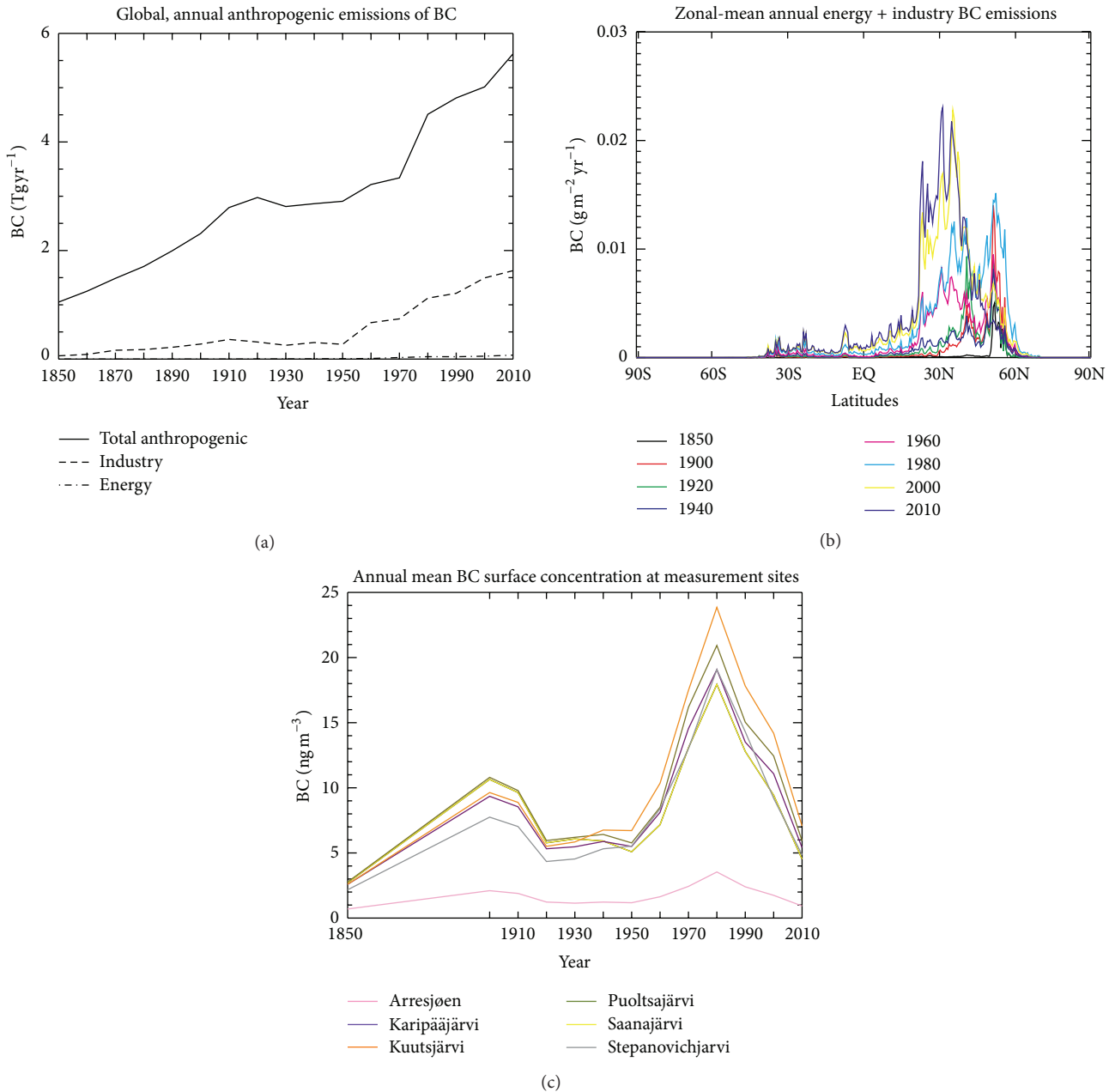


FIGURE 5: (a) Time series of annual energy and industrial emissions of BC used as input to the OsloCTM2. Also shown for comparison is the total anthropogenic emissions. (b) Zonal-mean annual BC emissions from the energy plus industrial sectors for selected years. (c) Time series of annual-mean surface concentration of BC from energy and industrial emissions at the six lakes.

Puoltsajärvi) and an underestimation at Zeppelin (Svalbard, close to Arresjøen), particularly during spring [22, 24, 32]. At Stepanovichjärvi, SCP deposition fluxes are not available because the sediment core was not dated. While the SCP concentrations at this site show much larger values than at the other sites, the model does not capture this. This might be due to the resolution of the model, but it is also probable that emissions from point sources such as the Nikel smelter, which is a likely source of pollution for the site, are underestimated or not captured in the model.

3.3. *Back Trajectories.* Figure 6 shows the direction and distance for which air, as a percentage, has spent time less than 100 m above the surface for 1983–2007. Only air below 100 m above the surface is considered because SCP and BC particles are produced only in this layer of air. The direction from each study lake to a grid cell centre was calculated using the Haversine formula and the distance is the great circle distance in kilometres. The area spanned by each segment in Figure 6 is thus the relative frequency that air has spent close to the surface in the direction of the segment. The colour scale

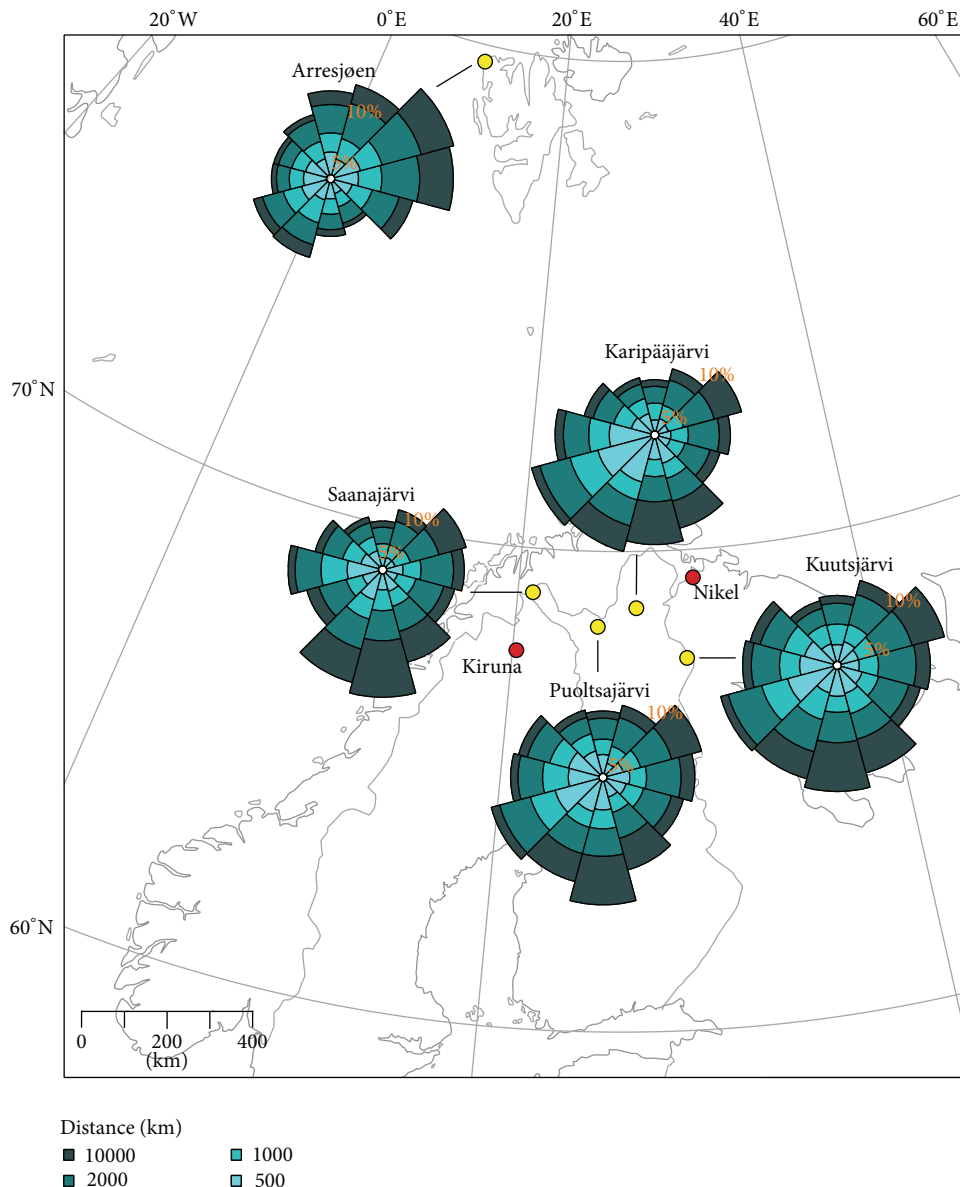


FIGURE 6: Frequency of direction and distance of trajectories for each of the study sites. Each segment size shows the frequency of air coming from the compass direction towards which it points. A light colouring indicates short distance (km) from the study site, whereas dark colours show a long travel distance. The yellow dots indicate the study lakes and the red dots the coal mine in Kiruna, Sweden, and the smelter in Nickel on the Kola Peninsula, Russia. The plotted data is based on the frequency of trajectories spending time near the surface within 7 days of arriving at the lakes in the interval 1983–2007.

of the segments reflects the distance the air has travelled over the previous seven days.

Karipääjärvi, Kuutsjärvi, and Puoltsajärvi seem to have quite similar transport patterns. Most air is transported from the south and east and from similar distances to the lakes. Saanajärvi on the other hand, while being geographically close to the other Finnish sites, has a somewhat different transport pattern. More of the air masses reaching it come from further away and more from the south and southwest compared to the other lakes in Finland. Arresjøen on Svalbard also has a diverging transport pattern. Much more of the

transport is coming from longer distances than to the other sites and mainly either from the southeast or northwest. This division between the lakes on the mainland and on Svalbard is probably due to the seasonal cycle of air circulation patterns and whether the lake is inside the polar dome or not.

The interannual or decadal variability of the source regions for the lakes can be calculated by subtracting a year/decade to that of another, and the absolute residual is then the variability in source regions for each lake coring site. The variability for all lakes is less than 10%, with Arresjøen displaying a somewhat larger variability than the other sites.

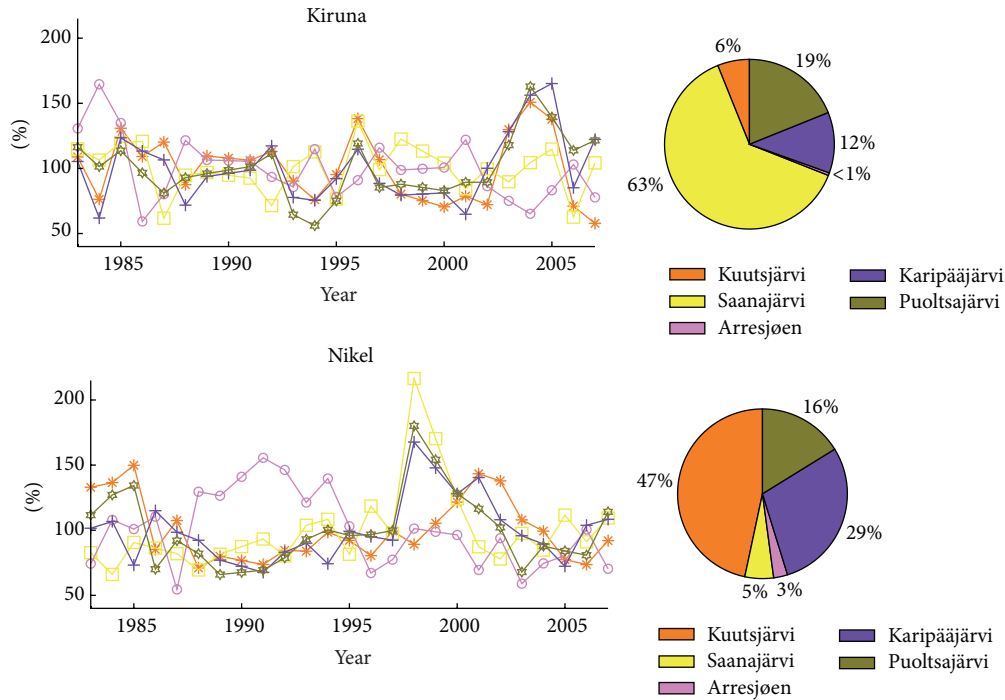


FIGURE 7: Left panel: time series of how transport to the coring sites changes over time from Kiruna (top) and Nikel (bottom). 100% is the 25-year average and years with higher % are years where there is more transport from Nikel/Kiruna to the lakes than on average. The years 1990 and 1999 have been linearly interpolated between neighbouring years. Right panel: pie charts showing the amount of transport from Kiruna (top) and Nikel (bottom) to the study lakes.

There has been no discernible trend pointing towards a change in transport to any of the study lakes during the period between 1983 and 2007.

Figure 7 relates the transport patterns of the five lakes to two expected significant emission sites in the region, Nikel and Kiruna. While the overall change in transport from year to year is small for all study sites, there is much stronger variability when looking at transport to the lakes from Nikel and Kiruna. As can be seen in Figure 7 (left panel), the transport to the lakes from Nikel and Kiruna vary annually by more than  $\pm 50\%$ . There are no significant signs of transport patterns changing over yearly or decadal time scales, from either Nikel or Kiruna. However, in terms of transport frequency, Kiruna is a more significant source area for the studied lakes since the total annual average time air masses spend before arriving at any study site is  $\sim 52000$  seconds above Kiruna compared to  $\sim 32000$  seconds above Nikel.

According to our results, the study lakes situated quite close to each other on the European mainland receive atmospheric transportation from relatively different sources. Figure 7 (right panel) compares the transport from Nikel and Kiruna to the study lakes. According to these results, Saanajärvi receives only about a third of the transport from Nikel compared to the other lakes on the mainland (Karipääjärvi, Kuutsjärvi, and Puoltsajärvi). Therefore, a more likely source for SCPs at Saanajärvi is the large iron mine in Kiruna, from where emissions are frequently transported towards Saanajärvi.

While the average transport patterns to Karipääjärvi, Kuutsjärvi, and Puoltsajärvi look quite similar (Figure 6), the lakes differ in both the direction and distance to strong sources. The distance seems to be the dominant factor determining air mass transport between Nikel and Kiruna and the study lakes. Arresjøen is located far from the polluting sources and receives very little transport from Northern Europe and transport from both Kiruna and Nikel is infrequent compared to the other lakes. Therefore, it seems that SCP deposition in Arresjøen could result from small local sources such as the power stations in Isfjorden as suggested in Rose et al. [13] while long-range transport from other sources in both Eurasia and North America is possibly contributing as well. For the remaining lakes both Nikel and Kiruna are probably the dominant sources since there is no other large scale fossil fuel based industrial activity in the area. Transport from Nikel has the strongest impact on SCP deposition in Kuutsjärvi and Karipääjärvi whereas Kiruna has the strongest impact on Saanajärvi.

Consequently it seems that variations in the magnitude of SCP deposition to the lakes (Figures 4(a) and 4(b)) can be mostly explained by Kuutsjärvi and especially Saanajärvi receiving greater amounts of polluted air masses from nearby large emission sources than the other study lakes. These lakes have two common features: they are located close to the pollution sources and are heavily impacted by prevailing winds coming from the direction of those sources. These are evident causes for the observed high deposition (Figures 4(a)

and 4(b)). The strong impact of Kiruna might also explain the earlier start of the SCP record in Saanajärvi than in the other study lakes (Figures 3, 4(a) and 4(b)) since mining started there in the 1870s. This analysis emphasises that even on a relatively small geographical scale, prevailing wind directions can be quite different and affect SCP and therefore also BC deposition to individual sites substantially.

*3.4. The Feasibility of Using SCPs and Lake Sediments in the Evaluation of BC Model Results.* Comparisons of observational measurements of BC with modelled results should be performed carefully since numerous methods to quantify BC and therefore BC definitions exist. Furthermore, studies investigating past concentrations, approximating to the complete BC spectrum from sedimentary records, are not yet available in large numbers, especially in the Arctic. Therefore, in order to get sufficient records, ice core data should additionally be used where available. With regard to comparisons with models, promising methods used for BC quantification from environmental records are variations of the thermal/optical methods which have been applied for soils and sediments by Han et al. [64, 65] and Husain et al. [66]. These Thermal Optical Transmittance/Reflectance (TOT and TOR) methods quantify EC in sediments and soils after chemical extraction and use the same instrument that measures EC from atmospheric samples. The application of this approach by Husain et al. [66] has shown consistency in EC measured from lake sediments and the atmosphere at the same site between 1978 and 2005. However, the application is very elaborate and time consuming and entails numerous known error sources [66]. Another promising method is the chemothermal oxidation method developed for soot BC quantification in sediments [58, 59] which can also be applied to atmospheric samples [67]. Unfortunately it is not known exactly how representative the soot BC concentrations retrieved with this method are of BC used in models, and this complicates any comparison. The emission factors used in the inventories of anthropogenic BC emissions represent a more EC-like carbonaceous compound than BC [68]. Several laboratory studies have shown EC and BC concentrations to differ significantly, up to a factor 7 between different methods (see [68] and references therein).

Our study, however, indicates the possibility of comparing historical observational data of a widely studied and clearly defined BC fraction, SCPs, with modelled BC trends albeit with the caveat that SCPs are only derived from industrial fossil-fuel combustion. Therefore, they cannot be used for comparison beyond the industrial era and neither for biomass burning reconstruction. However, reasonable comparisons are facilitated by the knowledge of the exact emission sources of SCP and emissions from these sectors can be selected for model runs. Since SCPs represent a well-defined fraction of BC, they could potentially be a useful tool for model evaluation. Currently, however, assessments of models based on SCP data alone are restricted as information on SCP source strength and the fraction of total BC represented by SCPs is unknown. Ideally, BC records from lake sediments would, in future consist of soot

BC or EC measurements (e.g., [64–66]), since these best represent EC measured in the atmosphere. However, until these measurements are readily available, SCP records may represent a useful tool for the validation and improvement of models. There are numerous SCP records available all around Europe and in some areas (e.g., UK) these exist in high numbers and distribution densities.

According to the recent specific definition of refractory black carbon in the atmosphere by Bond et al. [29], SCPs do not represent BC, since they are not an aggregate of small carbon spherules. Nonetheless, other properties (strong visible light absorption, refractoriness, and insolubility in water) are similar, although the exact mass absorption cross-section of SCPs is currently unknown. BC particles found in sediments are those that have been deposited from the atmosphere. Therefore, in order to facilitate BC model validation or to find natural background levels of contamination, it is crucial that a general definition of BC should also include particles readily studied in natural archives, such as SCPs.

## 4. Conclusions

In general we found a good agreement between the temporal records of SCP in lake sediments and modelled industrial and energy sector derived BC deposition. Discrepancies in the results are most likely explained by SCPs not representing all BC formed by these sectors but only a relatively small fraction. This explains the differences in magnitude as well as the model capturing a possible BC concentration and deposition peak in the early decades of the 20th century that is not observed in sedimentary SCP data.

Despite generally good agreement between SCP concentration and flux trends between lakes, some differences in the magnitude of depositional fluxes are evident. In general trends in deposition follow trends in emissions, as implied by the OsloCTM2-model. According to back trajectories of air masses it seems that trends in SCP deposition to the study sites are not caused by changes in general air mass transportation patterns, at least not during the last 25 years. On the contrary, differences in observed magnitudes of SCP deposition seem to be caused by differing quantities of polluted air masses being transported to the sites from nearby emission sources.

Our study also points to the fact that models might easily miss quite significant regional variation in BC concentrations and deposition both due to the coarse resolution of the model and possibly underestimation of local emission sources. The modelled trends are a manifestation of changes in emission strengths and geographical patterns. On a smaller geographical scale, however, the lack of detailed information on air mass transport patterns in the model becomes apparent. For example, the model cannot predict the higher SCP concentrations observed in a lake (Stepanovichjarvi) close to a known large emission source and it fails to capture the higher SCP deposition values in lakes receiving air masses from more polluted areas (Saanajärvi and Kuutsjärvi).

Our results underline the fact that significant variation in BC deposition can be recorded within a small geographical

area. The concentrations, deposition, and trends of BC may vary at a specific site for many reasons. These include factors that are captured by the OsloCTM2 model, local conditions that affect the sediment records ability to capture atmospheric deposition that the model cannot account for, and variation in transport patterns of air masses to the study sites. Therefore, numerous observational records are required to credibly validate and improve models. While ice sheets are extremely valuable as archives of atmospheric pollutant deposition histories, they are only found in restricted regions. Lake sediments can be found almost anywhere around the world and can play an important role in recording deposition history of BC and other pollutants.

Although the emissions of BC, specifically SCP, from industrial sectors have declined in Europe and North America during recent decades, emissions are increasing in Asian countries. Therefore, SCPs must also be considered as a significant component in climate change mitigation strategies in the future.

## Acknowledgments

The work was inspired and set in motion by collaboration with the NordForsk Top-Level Research Initiative Nordic Centre of Excellence CRAICC (Cryosphere-atmosphere interactions in a changing Arctic climate). M. Ruppel's work was funded by the Arctic Doctoral Programme ARKTIS of the University of Lapland, by CRAICC and the Academy of Finland Center of Excellence Program (Project 1118615) and by the Academy of Finland Project 257903. M. T. Lund's contribution was supported by the Norwegian Research Council within the project "Climate and Health Impacts of Short-Lived Atmospheric Components (SLAC)". Some of the model results are based on previous work by Ragnhild B. Skeie at CICERO. H. Grythe acknowledges the funding by CRAICC.

## References

- [1] T. Novakov, "The role of soot and primary oxidants in atmospheric chemistry," *Science of the Total Environment*, vol. 36, pp. 1–10, 1984.
- [2] E. D. Goldberg, *Black Carbon in the Environment*, John Wiley & Sons, New York, NY, USA, 1985.
- [3] J. I. Hedges, G. Eglinton, P. G. Hatcher et al., "The molecularly-uncharacterized component of nonliving organic matter in natural environments," *Organic Geochemistry*, vol. 31, no. 10, pp. 945–958, 2000.
- [4] C. A. Masiello, "New directions in black carbon organic geochemistry," *Marine Chemistry*, vol. 92, no. 1–4, pp. 201–213, 2004.
- [5] M. Elmquist, G. Cornelissen, Z. Kukulska, and Ö. Gustafsson, "Distinct oxidative stabilities of char versus soot black carbon: implications for quantification and environmental recalcitrance," *Global Biogeochemical Cycles*, vol. 20, no. 2, Article ID GB2009, 2006.
- [6] K. Hammes, M. W. I. Schmidt, R. J. Smernik, L. A. Currie, W. P. Ball et al., "Comparison of quantification methods to measure fire-derived (black/elemental carbon in soils and sediments using reference materials from soil, water, sediment and the atmosphere," *Global Biogeochemical Cycles*, vol. 21, Article ID GB3016, 2007.
- [7] N. L. Rose and B. Rippey, "The historical record of PAH, PCB, trace metal and fly-ash particle deposition at a remote lake in north-west Scotland," *Environmental Pollution*, vol. 117, no. 1, pp. 121–132, 2002.
- [8] N. L. Rose, S. Harlock, and P. G. Appleby, "The spatial and temporal distributions of spheroidal carbonaceous fly-ash particles (SCP) in the sediment records of European Mountain Lakes," *Water, Air, and Soil Pollution*, vol. 113, no. 1–4, pp. 1–32, 1999.
- [9] J. N. Cape, M. Coyle, and P. Dumitrescu, "The atmospheric lifetime of black carbon," *Atmospheric Environment*, vol. 59, pp. 256–263, 2012.
- [10] R. Jaenicke, "Atmospheric aerosols and global climate," *Journal of Aerosol Science*, vol. 11, no. 5–6, pp. 577–588, 1980.
- [11] M. Wik and I. Renberg, "Recent atmospheric deposition in Sweden of carbonaceous particles from fossil-fuel combustion surveyed using lake sediments," *Ambio*, vol. 20, no. 7, pp. 289–292, 1991.
- [12] N. L. Rose and S. Juggins, "A spatial relationship between carbonaceous particles in lake sediments and sulphur deposition," *Atmospheric Environment*, vol. 28, no. 2, pp. 177–183, 1994.
- [13] N. L. Rose, C. L. Rose, J. F. Boyle, and P. G. Appleby, "Lake-sediment evidence for local and remote sources of atmospherically deposited pollutants on Svalbard," *Journal of Paleolimnology*, vol. 31, no. 4, pp. 499–513, 2004.
- [14] S. Hicks and E. Isaksson, "Assessing source areas of pollutants from studies of fly ash, charcoal, and pollen from Svalbard snow and ice," *Journal of Geophysical Research D*, vol. 111, no. 2, Article ID D02113, 2006.
- [15] R. Bindler, I. Renberg, P. G. Appleby, N. J. Anderson, and N. L. Rose, "Mercury accumulation rates and spatial patterns in lake sediments from west Greenland: a coast to ice margin transect," *Environmental Science and Technology*, vol. 35, no. 9, pp. 1736–1741, 2001.
- [16] N. C. Doubleday, M. S. V. Douglas, and J. P. Smol, "Paleoenvironmental studies of black carbon deposition in the High Arctic: a case study from Northern Ellesmere Island," *Science of the Total Environment*, vol. 160–161, pp. 661–668, 1995.
- [17] C. C. Martins, M. C. Bicego, N. L. Rose et al., "Historical record of polycyclic aromatic hydrocarbons (PAHs) and spheroidal carbonaceous particles (SCPs) in marine sediment cores from Admiralty Bay, King George Island, Antarctica," *Environmental Pollution*, vol. 158, no. 1, pp. 192–200, 2010.
- [18] N. L. Rose, V. J. Jones, P. E. Noon, D. A. Hodgson, R. J. Flower, and P. G. Appleby, "Long-range transport of pollutants to the Falkland Islands and Antarctica: evidence from lake sediment fly-ash particle records," *Environmental Science and Technology*, vol. 46, no. 18, pp. 9881–9889, 2012.
- [19] D. Broman, C. Näf, M. Wik, and I. Renberg, "The importance of spheroidal carbonaceous particles for the distribution of particulate polycyclic aromatic hydrocarbons in an estuarine-like urban coastal water area," *Chemosphere*, vol. 21, no. 1–2, pp. 263–286, 1990.
- [20] N. L. Rose and H. Yang, "Temporal and spatial patterns of spheroidal carbonaceous particles (SCPs) in sediments, soils and deposition at Lochnagar," in *Lochnagar: The Natural History of a Mountain Lake. Developments in Paleoenvironmental Research*, N. L. Rose, Ed., pp. 403–423, Springer, Dordrecht, The Netherlands, 2007.

- [21] N. L. Rose, "Fly-ash particles," in *Tracking Environmental Change Using Lake Sediments*, W. M. Last and J. P. Smol, Eds., vol. 2 of *Physical and Geochemical Methods*, pp. 319–349, Kluwer Academic, Dordrecht, The Netherlands, 2001.
- [22] R. B. Skeie, T. Berntsen, G. Myhre et al., "Black carbon in the atmosphere and snow, from pre-industrial times until present," *Atmospheric Chemistry and Physics*, vol. 11, no. 14, pp. 6809–6836, 2011.
- [23] J.-F. Lamarque, T. C. Bond, V. Eyring et al., "Historical (1850–2000) gridded anthropogenic and biomass burning emissions of reactive gases and aerosols: methodology and application," *Atmospheric Chemistry and Physics*, vol. 10, no. 15, pp. 7017–7039, 2010.
- [24] Y. H. Lee, J. F. Lamarque, M. G. Flanner, C. Jiao, D. T. Shindell et al., "Evaluation of preindustrial to present-day black carbon and its albedo forcing from ACCMIP (Atmospheric Chemistry and Climate Model Intercomparison Project)," *Atmospheric Chemistry and Physics Discussion*, vol. 12, pp. 21713–21778, 2012.
- [25] J. R. McConnell, R. Edwards, G. L. Kok et al., "20th-Century industrial black carbon emissions altered arctic climate forcing," *Science*, vol. 317, no. 5843, pp. 1381–1384, 2007.
- [26] J. R. McConnell, "New Directions: historical black carbon and other ice core aerosol records in the Arctic for GCM evaluation," *Atmospheric Environment*, vol. 44, no. 21–22, pp. 2665–2666, 2010.
- [27] J. R. McConnell and R. Edwards, "Coal burning leaves toxic heavy metal legacy in the Arctic," *Proceedings of the National Academy of Sciences of the United States of America*, vol. 105, no. 34, pp. 12140–12144, 2008.
- [28] J. F. Lamarque, D. T. Shindell, B. Josse, P. J. Young, I. Cionni et al., "The Atmospheric Chemistry and Climate Model Intercomparison Project (ACCMIP): overview and description of models, simulations and climate diagnostics," *Geoscientific Model Development*, vol. 6, pp. 179–206, 2013.
- [29] T. C. Bond, S. J. Doherty, D. W. Fahey, P. M. Forster, T. Berntsen et al., "Bounding the role of black carbon in the climate system: a scientific assessment," *Journal of Geophysical Research-Atmospheres*, vol. 118, pp. 1–173, 2013.
- [30] N. L. Rose, "Carbonaceous particle record in lake sediments from the Arctic and other remote areas of the Northern Hemisphere," *Science of the Total Environment*, vol. 160–161, pp. 487–496, 1995.
- [31] S. J. Doherty, S. G. Warren, T. C. Grenfell, A. D. Clarke, and R. E. Brandt, "Light-absorbing impurities in Arctic snow," *Atmospheric Chemistry and Physics*, vol. 10, no. 23, pp. 11647–11680, 2010.
- [32] M. T. Lund and T. Berntsen, "Parameterization of black carbon aging in the OsloCTM2 and implications for regional transport to the Arctic," *Atmospheric Chemistry and Physics*, vol. 12, no. 15, pp. 6999–7014, 2012.
- [33] T. Berntsen, J. Fuglestad, G. Myhre, F. Stordal, and T. F. Berglen, "Abatement of greenhouse gases: does location matter?" *Climatic Change*, vol. 74, no. 4, pp. 377–411, 2006.
- [34] I. Renberg and H. Hansson, "The HTH sediment corer," *Journal of Paleolimnology*, vol. 40, no. 2, pp. 655–659, 2008.
- [35] J. R. Glew, "A new trigger mechanism for sediment samplers," *Journal of Paleolimnology*, vol. 2, no. 4, pp. 241–243, 1989.
- [36] P. G. Appleby, P. J. Nolan, D. W. Gifford et al., "210Pb dating by low background gamma counting," *Hydrobiologia*, vol. 143, no. 1, pp. 21–27, 1986.
- [37] P. G. Appleby, N. Richardson, and P. J. Nolan, "Self-absorption corrections for well-type germanium detectors," *Nuclear Instruments and Methods in Physics Research B*, vol. 71, no. 2, pp. 228–233, 1992.
- [38] N. L. Rose, "A note on further refinements to a procedure for the extraction of carbonaceous fly-ash particles from sediments," *Journal of Paleolimnology*, vol. 11, no. 2, pp. 201–204, 1994.
- [39] N. L. Rose, "Quality control in the analysis of lake sediments for spheroidal carbonaceous particles," *Limnology and Oceanography*, vol. 6, pp. 172–179, 2008.
- [40] M. J. Prather, "Numerical advection by conservation of 2nd-order moments," *Journal of Geophysical Research-Atmospheres*, vol. 91, no. D6, pp. 6671–6681, 1986.
- [41] M. Tiedtke, "A comprehensive mass flux scheme for cumulus parameterization in large-scale models," *Monthly Weather Review*, vol. 117, no. 8, pp. 1779–1800, 1989.
- [42] A. A. M. Holtslag, E. I. F. De Bruijn, and H.-L. Pan, "A high resolution air mass transformation model for short-range weather forecasting," *Monthly Weather Review*, vol. 118, no. 8, pp. 1561–1575, 1990.
- [43] A. M. Thomson, K. V. Calvin, S. J. Smith et al., "RCP4.5: a pathway for stabilization of radiative forcing by 2100," *Climatic Change*, vol. 109, no. 1, pp. 77–94, 2011.
- [44] W. F. Cooke, C. Liousse, H. Cachier, and J. Feichter, "Construction of a 1 degrees x 1 degrees fossil fuel emission data set for carbonaceous aerosol and implementation and radiative impact in the ECHAM4 model," *Journal of Geophysical Research D*, vol. 104, no. 18, pp. 22137–22162, 1999.
- [45] E. Vignati, J. Wilson, and P. Stier, "M7: an efficient size-resolved aerosol microphysics module for large-scale aerosol transport models," *Journal of Geophysical Research D*, vol. 109, no. D22, article 27, 2004.
- [46] A. Stohl, C. Forster, A. Frank, P. Seibert, and G. Wotawa, "Technical note: the Lagrangian particle dispersion model FLEXPART version 6.2," *Atmospheric Chemistry and Physics*, vol. 5, no. 9, pp. 2461–2474, 2005.
- [47] A. Stohl and D. J. Thomson, "A density correction for Lagrangian particle dispersion models," *Boundary-Layer Meteorology*, vol. 90, no. 1, pp. 155–167, 1999.
- [48] A. Stohl, A. J. Prata, S. Eckhardt et al., "Determination of time- and height-resolved volcanic ash emissions and their use for quantitative ash dispersion modeling: the 2010 Eyjafjallajökull eruption," *Atmospheric Chemistry and Physics*, vol. 11, no. 9, pp. 4333–4351, 2011.
- [49] J. L. Palau, J. Meliá, D. Segarra, G. Pérez-Landa, F. Santa-Cruz, and M. M. Millán, "Seasonal differences in SO<sub>2</sub> ground-level impacts from a power plant plume on complex terrain," *Environmental Monitoring and Assessment*, vol. 149, no. 1–4, pp. 445–455, 2009.
- [50] A. Stohl, "Characteristics of atmospheric transport into the Arctic troposphere," *Journal of Geophysical Research*, vol. 111, no. D11, pp. 1–17, 2006.
- [51] D. P. Dee, S. M. Uppala, A. J. Simmons et al., "The ERA-Interim reanalysis: configuration and performance of the data assimilation system," *Quarterly Journal of the Royal Meteorological Society*, vol. 137, no. 656, pp. 553–597, 2011.
- [52] S. M. Uppala, P. W. Kållberg, A. J. Simmons et al. et al., "The ERA-40 re-analysis," *Quarterly Journal of the Royal Meteorological Society*, vol. 131, pp. 2961–3012, 2005, <http://reanalyses.org/atmosphere/era40-references>.

- [53] A. Korhola, S. Sorvari, M. Rautio et al., “A multi-proxy analysis of climate impacts on the recent development of subarctic Lake Saanajärvi in Finnish Lapland,” *Journal of Paleolimnology*, vol. 28, no. 1, pp. 59–77, 2002.
- [54] N. L. Rose, S. Juggins, and J. Watt, “The characterisation of carbonaceous fly-ash particles from major European fossil-fuel types and applications to environmental samples,” *Atmospheric Environment*, vol. 33, no. 17, pp. 2699–2713, 1999.
- [55] T. S. Traaen, T. Moiseenko, V. Dauvalter, S. Rognerud, A. Hemiksen, and L. Kudravseva, “Acidification of surface waters, nickel and copper in water and lake sediments in the Soviet-Norwegian border areas,” Progress Report to Norwegian-Soviet Environmental Protection Commission, 1991.
- [56] A. Korhola, J. Weckström, and M. Nyman, “Predicting the long-term acidification trends in small subarctic lakes using diatoms,” *Journal of Applied Ecology*, vol. 36, no. 6, pp. 1021–1034, 1999.
- [57] G. Muri, S. G. Wakeham, and N. L. Rose, “Records of atmospheric delivery of pyrolysis-derived pollutants in recent mountain lake sediments of the Julian Alps (NW Slovenia),” *Environmental Pollution*, vol. 139, no. 3, pp. 461–468, 2006.
- [58] Ö. Gustafsson, F. Haghseta, C. Chan, J. Macfarlane, and P. M. Gschwend, “Quantification of the dilute sedimentary soot phase: implications for PAH speciation and bioavailability,” *Environmental Science and Technology*, vol. 31, no. 1, pp. 203–209, 1997.
- [59] Ö. Gustafsson, T. D. Bucheli, Z. Kukulska et al., “Evaluation of a protocol for the quantification of black carbon in sediments,” *Global Biogeochemical Cycles*, vol. 15, no. 4, pp. 881–890, 2001.
- [60] T. C. Bond, D. G. Streets, K. F. Yarber, S. M. Nelson, J.-H. Woo, and Z. Klimont, “A technology-based global inventory of black and organic carbon emissions from combustion,” *Journal of Geophysical Research D*, vol. 109, no. D14, article 27, 2004.
- [61] T. C. Bond, E. Bhardwaj, R. Dong et al., “Historical emissions of black and organic carbon aerosol from energy-related combustion, 1850–2000,” *Global Biogeochemical Cycles*, vol. 21, no. 2, Article ID GB2018, 2007.
- [62] M. Elmquist, Z. Zencak, and Ö. Gustafsson, “A 700 year sediment record of black carbon and polycyclic aromatic hydrocarbons near the EMEP air monitoring station in Aspvreten, Sweden,” *Environmental Science and Technology*, vol. 41, no. 20, pp. 6926–6932, 2007.
- [63] D. T. Shindell, M. Chin, F. Dentener et al., “A multi-model assessment of pollution transport to the Arctic,” *Atmospheric Chemistry and Physics*, vol. 8, no. 17, pp. 5353–5372, 2008.
- [64] Y. Han, J. Cao, Z. An et al., “Evaluation of the thermal/optical reflectance method for quantification of elemental carbon in sediments,” *Chemosphere*, vol. 69, no. 4, pp. 526–533, 2007.
- [65] Y. Han, J. Cao, J. C. Chow et al., “Evaluation of the thermal/optical reflectance method for discrimination between char- and soot-EC,” *Chemosphere*, vol. 69, no. 4, pp. 569–574, 2007.
- [66] L. Husain, A. J. Khan, T. Ahmed, K. Swami, A. Bari et al., “Trends in atmospheric elemental carbon from 1835 to 2005,” *Journal of Geophysical Research*, vol. 113, no. D13102, 2008.
- [67] Z. Zencak, M. Elmquist, and Ö. Gustafsson, “Quantification and radiocarbon source apportionment of black carbon in atmospheric aerosols using the CTO-375 method,” *Atmospheric Environment*, vol. 41, no. 36, pp. 7895–7906, 2007.
- [68] E. Vignati, M. Karl, M. Krol, J. Wilson, P. Stier, and F. Cavalli, “Sources of uncertainties in modelling black carbon at the global scale,” *Atmospheric Chemistry and Physics*, vol. 10, no. 6, pp. 2595–2611, 2010.

## Research Article

# Comparisons between Hygroscopic Measurements and UNIFAC Model Predictions for Dicarboxylic Organic Aerosol Mixtures

Jae Young Lee and Lynn M. Hildemann

*Civil & Environmental Engineering Department, Stanford University, Stanford, CA 94305, USA*

Correspondence should be addressed to Jae Young Lee; [jaeyoung.lee@alumni.stanford.edu](mailto:jaeyoung.lee@alumni.stanford.edu)

Received 22 February 2013; Revised 15 May 2013; Accepted 9 June 2013

Academic Editor: Lucas Alados-Arboledas

Copyright © 2013 J. Y. Lee and L. M. Hildemann. This is an open access article distributed under the Creative Commons Attribution License, which permits unrestricted use, distribution, and reproduction in any medium, provided the original work is properly cited.

Hygroscopic behavior was measured at 12°C over aqueous bulk solutions containing dicarboxylic acids, using a Baratron pressure transducer. Our experimental measurements of water activity for malonic acid solutions (0–10 mol/kg water) and glutaric acid solutions (0–5 mol/kg water) agreed to within 0.6% and 0.8% of the predictions using Peng's modified UNIFAC model, respectively (except for the 10 mol/kg water value, which differed by 2%). However, for solutions containing mixtures of malonic/glutaric acids, malonic/succinic acids, and glutaric/succinic acids, the disagreements between the measurements and predictions using the ZSR model or Peng's modified UNIFAC model are higher than those for the single-component cases. Measurements of the overall water vapor pressure for 50 : 50 molar mixtures of malonic/glutaric acids closely followed that for malonic acid alone. For mixtures of malonic/succinic acids and glutaric/succinic acids, the influence of a constant concentration of succinic acid on water uptake became more significant as the concentration of malonic acid or glutaric acid was increased.

## 1. Introduction

The direct and indirect effects of atmospheric aerosols on global climate change have been well established in a number of previous studies. The direct effect is caused by scattering and absorbing solar radiation, and the indirect effect is caused by aerosols acting as cloud condensation nuclei (CCN) (e.g., [1–3]). For both effects, the hygroscopicity of the aerosol plays an important role, since it influences the size of the particle and its ability to become a CCN (e.g., [4–7]).

Atmospheric aerosols consist of inorganic and organic compounds. Organic compounds account for 20% to 90% of the total fine particle mass in the troposphere (e.g., [2, 8, 9]). Among the organic aerosol components in the atmosphere, dicarboxylic acids have been frequently measured in previous studies (e.g., [10]). Oxalic acid is the most dominant dicarboxylic acid in aerosols, followed by malonic and succinic acids [10, 11]. In addition, most dicarboxylic acids are highly soluble in water, which makes them likely to affect the hygroscopic properties of atmospheric aerosols [11–13].

A number of previous studies have measured the water uptake of pure water-soluble organic compounds (e.g., [11,

14–16]) and the water uptake of inorganic and water-soluble organic mixtures (e.g., [17–23]). In the inorganic-organic mixture studies, researchers have reported that the presence of organic compounds can reduce or enhance the hygroscopic growth of pure inorganic compounds. However, only a few studies have measured the hygroscopicity of organic mixtures [19, 24–26].

For an aerosol containing mixed inorganic/organic or organic/organic compounds, water uptake has been most commonly predicted using the Zdanovskii-Stokes-Robinson (ZSR) method [27]. Choi and Chan [19] and Marcolli et al. [24] reported that their measurements agreed well with the predictions made by ZSR method, while Svenningsson et al. [26] showed that the ZSR model was applicable to 3 out of the 4 mixtures they measured.

Another approach uses the UNIFAC (UNIQUAC Functional-Group Activity Coefficients) [28] or a modified UNIFAC [14] model to predict the hygroscopic behavior of a single or mixed organic solution. This method estimates activity coefficients of a system containing various functional groups based on previously determined interaction characteristics among those functional groups. Choi and Chan [19] reported

that their organic mixture results showed good agreement with the modified UNIFAC predictions. Moore and Raymond [25] reported that measurements of multicomponent mixtures of 5 to 10 dicarboxylic acids were in good agreement with the original UNIFAC predictions while glutaric-malonic mixture data were in good agreement with the modified UNIFAC predictions. However, there is still a dearth of experimental data involving the hygroscopic behavior of organic mixtures, so it is not yet possible to assess the overall reliability of using these models for organic mixtures.

This study examines how mixtures of two water-soluble organics (malonic and glutaric acid) take up water and how the water uptake of a sparingly soluble organic (succinic acid) is affected by the presence of a water-soluble organic (malonic or glutaric acid). To measure the hygroscopic behavior of organic mixtures, this study measured water vapor pressures at 12°C over aqueous bulk solutions containing dicarboxylic acids. These measurement data are compared with the predictions made using ZSR and Peng's modified UNIFAC model [14], one of the most frequently used methods for estimating the hygroscopic behavior of organic aerosols.

## 2. Experimental Procedures

**2.1. Materials.** The organic compounds used in this study are listed in Table 1. For this exploratory study, we focused on 3 species of dicarboxylic acids, a water-soluble chemical group frequently identified in atmospheric aerosols. Malonic acid and glutaric acid were used due to their high solubility, while succinic acid was chosen due to its relatively low solubility. The large odd-even variation in solubility for the dicarboxylic acids is due to the effects of the *cis*- versus *trans*-orientation of the end groups on the strength of the intermolecular interactions (e.g., [32]). Table 1 includes the chemical formula, molecular mass (g/mol), density (g/cm<sup>3</sup>), solubility (g/100 g of water), and manufacturer information.

**2.2. Water Vapor Pressure Measurements.** Hygroscopicity was analyzed by measuring the water vapor pressure over a bulk solution. This bulk solution measurement approach is similar to the one used by previous studies (e.g., [19, 33–35]). The bulk solution method has a couple advantages over two other commonly used methods to measure hygroscopicity, the tandem differential mobility analyzer (TDMA) and the electrodynamic balance (EDB). First, a bulk solution allows for a long residence time, ensuring equilibrium between water and organic compounds. Second, the vapor pressure over a bulk solution can be directly measured using the Baratron under highly controlled temperature conditions. A schematic of our measurement apparatus is illustrated in Figure 1.

An aqueous organic solution sample was prepared by adding Milli-Q purified water (18.2 M). The solid chemicals and liquid water mass were measured by digital balance with uncertainty of ±0.01 g (less than 1% of the total mass). The organic solution was mixed by a magnetic Teflon-coated stir bar and stirrer until the chemical was completely dissolved in pure water. This sample solution was placed on a glass vessel

manifold and then completely frozen with liquid nitrogen. The headspace air was pumped out using a high vacuum pump (GLD-051, ULVAC, Inc., MA, USA) while the aqueous solution was frozen. After these freeze-and-draw steps, the solution was thawed with a heat gun. All headspace air in the glass vessel manifold was purged by repeating the freeze-draw-thaw steps at least three times and then verifying that the headspace air pressure measured by the Baratron was less than 0.02 Torr. After purging all of the headspace air, the glass vessel containing the aqueous solution was submerged in a thermostat bath controlled by a refrigerated circulator (Neslab RTE-10, Thermo Electron Corp., Inc., NH, USA). The water temperature in the bath was measured with a digital thermometer (Digi Sense RTD Platinum, Eutech Instruments, Singapore). After submerging the glass vessel containing the organic solution, the target temperature, 12°C, was maintained for at least 30 minutes before the start of measurements, to achieve equilibrium.

The equilibrium water vapor pressure over the organic solution at 12°C was monitored by the Baratron pressure transducer (Model 626A, MKS Instruments, Inc., MA, USA) directly. Since the Baratron can only measure the total air pressure in the glass vessel, a quadrupole mass spectrometer (QMS 200, Stanford Research Systems, Inc., CA, USA) was used in parallel, to detect and quantify any organic vapor in the headspace air.

The Baratron and QMS were calibrated using Milli-Q water over a wide range of temperatures to eliminate any systematic error from the measurement setup. The small background signal originating from the mass spectrometer was measured before the experiment and then subtracted from the steady-state reading of the QMS. For the malonic, succinic, and glutaric acids used in this work, no organic vapor was detected by QMS in the headspace air of the glass vessel. As a result, all water vapor pressure values reported in this work are from the Baratron. The equilibrium water vapor pressure was measured independently four times for each solution. The standard deviation of these quadruplicate measurements was determined to be <0.4% for the averages reported in this study, so error bars of 0.4% are used in the figures. Any differences of 0.5% or more between measurements and model are viewed as significant.

For the physical dimensions (diameter and length) of the capillary used, the optimal performance of the QMS in terms of the detection sensitivity occurs for an inlet pressure of around 10 Torr. Therefore, we chose the solution temperature to be 12°C so that the vapor pressure over the bulk solution would be around 10 Torr.

## 3. Results and Discussion

Two approaches were used to measure the hygroscopic behavior of dicarboxylic acid mixtures. The malonic/glutaric acid mixtures were studied by varying concentration levels while maintaining a 50 : 50 molar mass ratio, due to the high solubility of both compounds. For the malonic/succinic and glutaric/succinic mixtures, a different approach was used, with the concentration of succinic acid held constant while varying the concentration of the second acid. This is because

TABLE 1: Chemical properties of organic compounds.

| Compound name | Chemical formula  | Molar mass (g/mol) | Density (g/cm <sup>3</sup> ) | Solubility (g/100 g) at 25°C | Manufacturer  |
|---------------|---|--------------------|------------------------------|------------------------------|---------------|
| Malonic acid  | $C_3H_4O_4$<br>(HOOC-CH <sub>2</sub> -COOH)                 | 104.06             | 1.619 <sup>a</sup>           | 161 <sup>b</sup>             | Alfa Aesar    |
| Succinic acid | $C_4H_6O_4$<br>(HOOC-(CH <sub>2</sub> ) <sub>2</sub> -COOH) | 118.09             | 1.572 <sup>a</sup>           | 8.8 <sup>b</sup>             | Sigma-Aldrich |
| Glutaric acid | $C_5H_8O_4$<br>(HOOC-(CH <sub>2</sub> ) <sub>3</sub> -COOH) | 132.12             | 1.429 <sup>a</sup>           | 116 <sup>b</sup>             | Alfa Aesar    |

<sup>a</sup>Lide [29]; <sup>b</sup>summarized in Saxena and Hildemann [30].

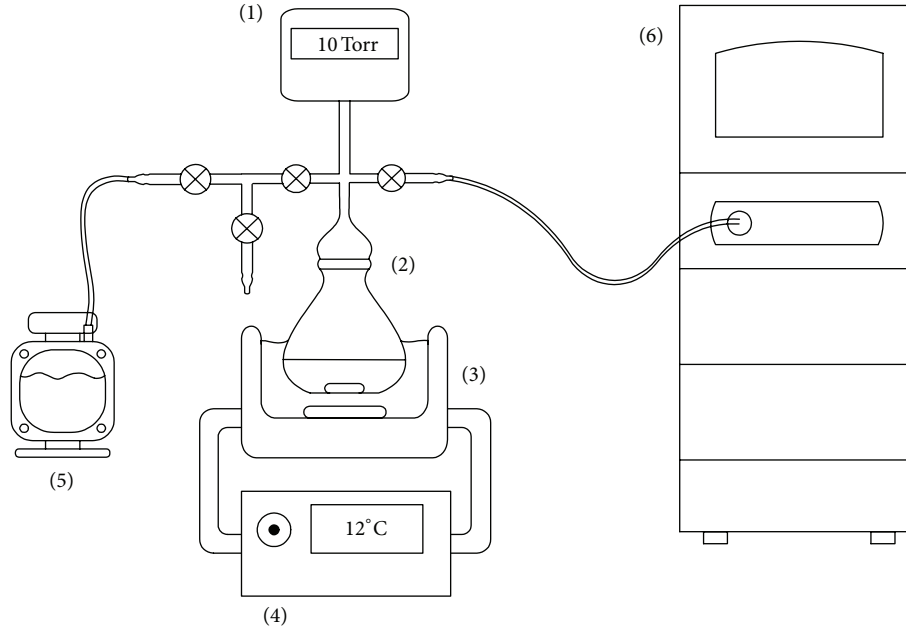


FIGURE 1: Schematic of water uptake measurement apparatus. This drawing shows the interconnections between (1) Baratron pressure transducer, (2) glass vessel manifold, (3) thermostat bath, (4) refrigerated circulator, (5) high vacuum pump, and (6) quadrupole mass spectrometer (QMS).

succinic acid is less soluble in water than the other two acids. Experimental measurements were compared with the predictions made using ZSR and UNIFAC.

**3.1. Single-Component Solutions.** For validation of the method and initial comparisons with UNIFAC, water vapor pressure was measured over single-component organic solutions. The water activity of a solution is related to the measured pressure via the following equation:

$$\text{Water activity } (a_w) = \frac{RH}{100} = \frac{p_s}{p_0}, \quad (1)$$

where RH = relative humidity (%);  $p_s$  = vapor pressure over organic solution; and  $p_0$  = vapor pressure over pure water.

For the single-component solutions, measurements spanned concentrations from 0.1 mol/kg water to near the solubility limits at 12°C (10 mol/kg water for malonic acid and 5 mol/kg water for glutaric acid). As shown in Figures 2(a) and 2(b), water activity plots for both malonic acid and glutaric acid decrease as the acid concentration increases and agree with other experimental studies. The dotted lines, denoting Peng's modified UNIFAC prediction, agree with our

data to within 0.6% for malonic acid (except for the 10 mol/kg water value, which differs by 2%) and 0.8% for glutaric acid. Note that Peng's measurement was taken at 25°C, while Braban's and ours were taken at around 12°C. Peng's modified UNIFAC also estimated water activity at 12°C. However, the variation in water uptake as the temperature increases from 12°C to 25°C is small for solute molalities of less than 8 mol/kg water; for example, for malonic acid, Braban et al. (2003) [11] experimentally observed a decrease in water uptake of <0.05%/C, while UNIFAC predicts a small increase in water uptake of <0.02%/C with increasing temperature.

The experimentally measured relationship between water activity and solute molality can be used to determine the hygroscopic growth factor ( $G_f$ )—the ratio between the wet and dry particle diameters—at a specific RH. The following equation [36, 37] relates the hygroscopic growth factor ( $G_f$ ) to the solute molality ( $m_s$ ):

$$G_f = \left\{ \frac{\rho_{\text{dry}} m_{\text{wet}}}{\rho_{\text{wet}} m_{\text{dry}}} \right\}^{1/3} = \left\{ \frac{\rho_{\text{dry}}}{\rho_{\text{wet}}} \left( \frac{10^3 + MW_s \times m_s}{MW_s \times m_s} \right) \right\}^{1/3}, \quad (2)$$

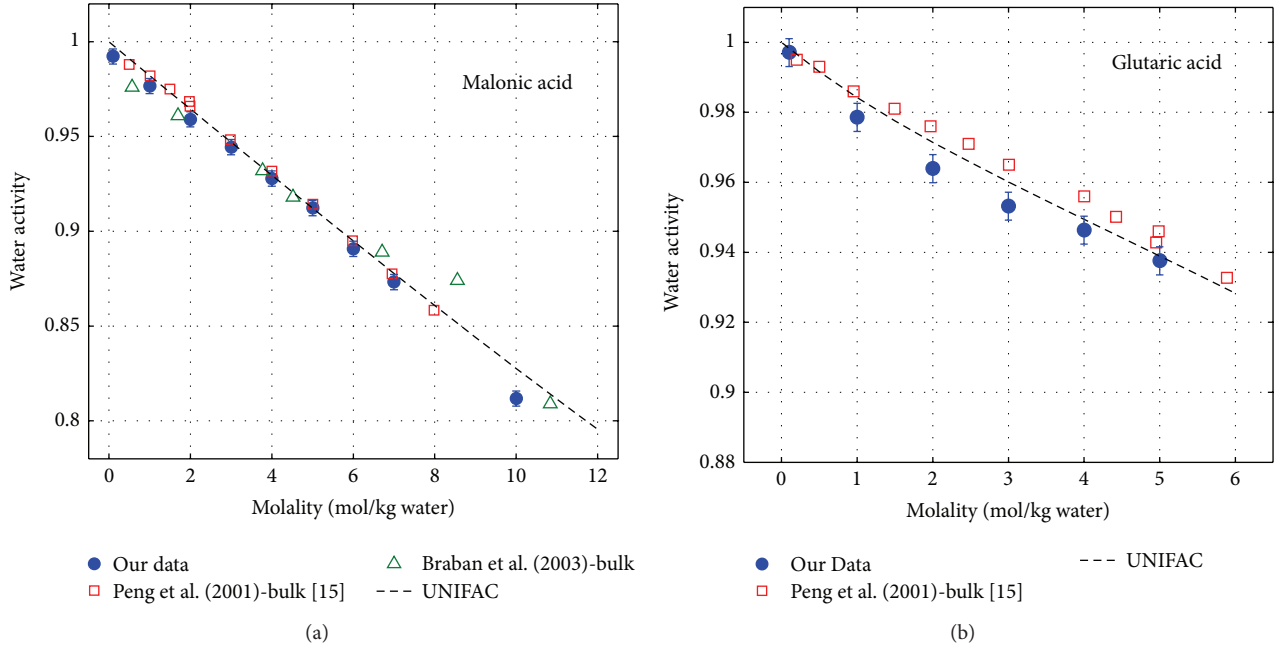


FIGURE 2: Water activity of (a) malonic acid and (b) glutaric acid. Each data point represents the average of 4 replicate measurements; error bars on measured data represent standard deviation of 0.4% (discussed in Section 2). The measurement data by Peng et al. (2001) [14] and Braban et al. (2003) [11] were at 25°C and 285.1 K (=11.95°C), respectively.

TABLE 2: Growth factors ( $G_f$ ) for malonic and glutaric acids in this study (at 12°C) versus other studies<sup>a</sup>.

|               | $G_f$ (85%)      |  | $G_f$ (90%)      |  | $G_f$ (95%) |                                       |
|---------------|------------------|--|------------------|--|-------------|---------------------------------------|
|               | This study       | Other studies  | This study       | Other studies  | This study  | Other studies <sup>b</sup>            |
| Malonic acid  | 1.43             | 1.40 <sup>d</sup> , 1.37 <sup>e</sup><br>1.32 <sup>i</sup> , 1.28 <sup>g</sup> | 1.52             | 1.73 <sup>c</sup> ; 1.53 <sup>d</sup><br>1.52 <sup>g</sup> ; 1.48 <sup>f</sup> | 1.91        | 1.86 <sup>g</sup> ; 1.84 <sup>d</sup> |
| Glutaric acid | N/A <sup>c</sup> | 1.15 <sup>e</sup> ; 1.10 <sup>h</sup><br>1.09 <sup>d</sup> ; 1 <sup>f</sup>    | N/A <sup>c</sup> | 1.30 <sup>d</sup> ; 1.29 <sup>e</sup><br>1 <sup>f</sup>                        | 1.59        | 1.49 <sup>d</sup>                     |

<sup>a</sup> $G_f$  values for succinic acid are not measurable via bulk solution methods, since its DRH is greater than 95% at 12°C.

<sup>b</sup>Growth factors at 95% RH are calculated from their raw data.

<sup>c</sup>DRH is greater than 90% at 12°C. Therefore,  $G_f$  (85%) and  $G_f$  (90%) are not measurable via bulk solution methods at 12°C. Values listed from other studies used EDB, TDMA, or bulk solution method at 22–30°C.

<sup>d</sup>Peng et al. [14], EDB measurements at 25°C.

<sup>e</sup>Prenni et al. [16], TDMA measurements at 30°C.

<sup>f</sup>Wise et al. [31], bulk solution measurements at 25°C.

<sup>g</sup>Braban et al. [11],  $G_f$  is calculated from its raw data, bulk solution measurements at 285.1 K (=11.95°C).

<sup>h</sup>Cruz and Pandis [20], EDB measurements at 22–26°C.

where  $m_{\text{wet}}$  = wet particle mass;  $m_{\text{dry}}$  = dry particle mass;  $\rho_{\text{wet}}$  = wet particle concentration ( $\text{g}/\text{m}^3$ );  $\rho_{\text{dry}}$  = dry particle concentration ( $\text{g}/\text{m}^3$ );  $MW_s$  = molecular weight of solute ( $\text{g}/\text{mol}$ ); and  $m_s$  = solute molality ( $\text{mol}/\text{kg}$  water).

Table 2 summarizes the  $G_f$  values calculated at RHs of 85%, 90%, and 95%. As can be seen from Table 2, most of our  $G_f$  values are within the range of those found in, or calculated based on, the previous literature. The  $G_f$  values for glutaric acid at 85% and 90% RH cannot be assessed via our measurement setup. This is because the bulk solution method cannot simulate the particle condition prior to full deliquescence, and the DRH (deliquescence relative humidity) was found to be greater than 90% at 12°C—this can be seen via the fact that the water activity is greater than 0.9 at any concentrations of

glutaric acid up to the solubility limit (see Figure 2(b)). For comparison, DRH values for glutaric acid at 25°C have been reported to be 88.9% and 88.5% [14, 31]. Other researchers who reported  $G_f$  at 85% and 90% used an EDB, a TDMA, or a bulk solution method at higher temperature ranges (22–30°C) [14, 16, 20, 25]. Similarly, the  $G_f$  values for succinic acid are not available even at an RH of 95%, since its DRH is greater than 95% at 12°C. Wise et al. [31] and Peng et al. [14] reported DRH values for succinic acid at 25°C of 97.6% and 98.8%, respectively.

3.2. *Mixture of Malonic and Glutaric Acids.* To study the hygroscopicity of organic mixtures, the water vapor pressure was measured over organic solutions containing malonic acid

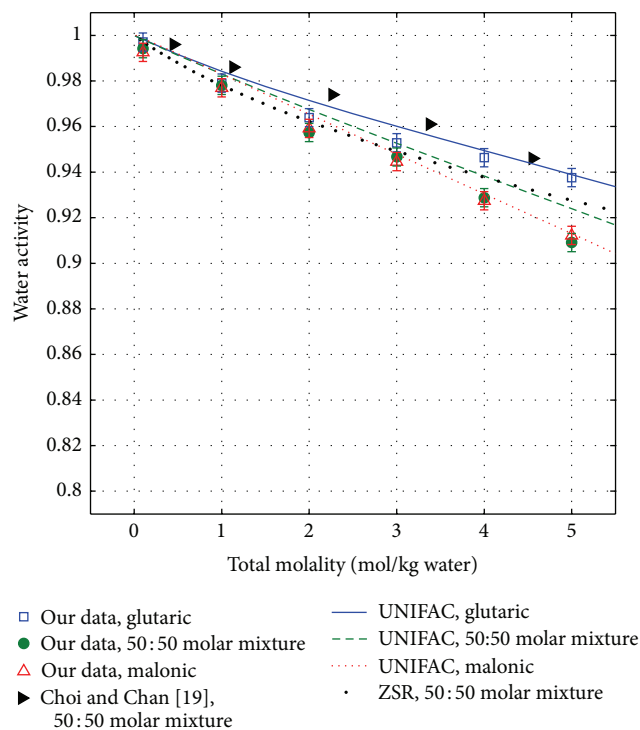


FIGURE 3: Water activity of malonic acid, glutaric acid and their equal molar mixture. Each data point represents the average of 4 replicate measurements; error bars on measured data represent standard deviation of 0.4%.

and glutaric acid at a 50 : 50 molar mass ratio. Figure 3 shows our measurements of water activity for the malonic/glutaric acid mixture along with the prediction made by UNIFAC.

Using Peng’s modified UNIFAC model for mixtures, this 50 : 50 molar mixture of malonic/glutaric acids was predicted to fall roughly midway between the hygroscopicity of the two individual organics. In the UNIFAC model, the contribution made by one functional group is independent of that made by another, and it systematically predicts a water activity for two-component mixtures that is intermediate between the individual dicarboxylic acids. However, in our measurements, the water uptake of this mixed solution closely followed that of malonic acid. This led to a greater water uptake than predicted by the modified UNIFAC model for mixtures. As a result, the measurements were higher than UNIFAC predictions for mixtures of these two acids by up to 1.6% at 5 mol/kg water. Since the standard deviation for each set of 4 replicate measurements was less than 0.4%, the observed discrepancies between our measurements and model predictions reflect a significant difference.

Previously, Moore and Raymond used HTDMA [25] and Choi and Chan used both EDB and the bulk method [19] to measure the hygroscopicity of malonic/glutaric acid mixtures. They reported good agreement between their data and UNIFAC predictions, over a wide range of RH (20–100%). However, in fact the water activity measurements in the HTDMA and EDB studies were consistently lower than the model predictions by up to ~1-2%, consistent with the decrease found in our study. However, as shown in Figure 3,

Choi and Chan’s measurements using the bulk solution method show higher water activities than the model. The cause of this disagreement is unclear; however, it might be due to differences in measurement temperature and/or the method of measuring water activity.

Figure 3 also shows the predictions based on the ZSR mixing rule. The original ZSR [27] equation is given by

$$\sum_i \frac{m_i}{M_i} = 1, \quad (3)$$

where  $m_i$  is the molality of solute  $i$  in a mixture and  $M_i$  is the molality of the solute when it is alone at a given relative humidity. This equation can be equivalently expressed as the following two equations (e.g., [20, 25]):

$$\text{mass}_{\text{water,mix}} = \sum_i \text{mass}_{\text{water},i} \quad (4)$$

$$G_{f,\text{mixture}} = \left\{ \epsilon \cdot G_{f,\text{malonic}}^3 + (1 - \epsilon) \cdot G_{f,\text{glutaric}}^3 \right\}^{1/3}, \quad (5)$$

where  $\text{mass}_{\text{water,mix}}$  is the total water uptake of the mixture,  $\text{mass}_{\text{water},i}$  is the water uptake of each species  $i$ , and  $\epsilon$  is the volume fraction of malonic acid in the dry particle. The growth factor of each individual compound was first calculated using (2), and then the growth factor for the mixture was estimated using (5). By converting back to molality, we show in Figure 3 that the predicted ZSR water activity for the mixture lies between those of the individual compounds. This result is due to the assumption that the water uptake of a mixture can be calculated by adding that of each individual compound within the mixture (see (4)). Thus, the ZSR approach overpredicts water activity, compared with our measurements up to 2.3%.

**3.3. Mixture of Malonic and Succinic Acids.** For mixtures of malonic and succinic acids, we added a set concentration (0.3 mol/kg water) of succinic acid to 1 to 7 mol/kg water of malonic acid solution. The concentration of succinic acid was chosen based on its maximum solubility at 12°C (see Table 1 for the reported solubility of succinic acid at 25°C). This approach allows an examination of how the hygroscopicity of a set concentration of the less-soluble succinic acid depends on the concentration of malonic acid in the mixture.

As seen in Figure 4, the modified UNIFAC model predicted that the additional amount of water uptake due to addition of succinic acid was essentially a constant increment, regardless of the concentration of malonic acid. However, for our measurements, the influence of the succinic acid on water activity was not significant for 1, 2, and 3 mol/kg water of malonic acid solutions (a decrease in water activity of less than 0.2%). In contrast, at higher concentrations, the malonic acid solution showed a noticeable decrease in water activity (of 1.0, 1.1, 1.1, and 1.4% for 4, 5, 6, and 7 mol/kg water of malonic acid, resp.) when 0.3 mol/kg water of succinic acid was added. This result again suggests that the noninteraction assumption in UNIFAC can lead to an overestimate of the water activity in dicarboxylic acid mixtures.

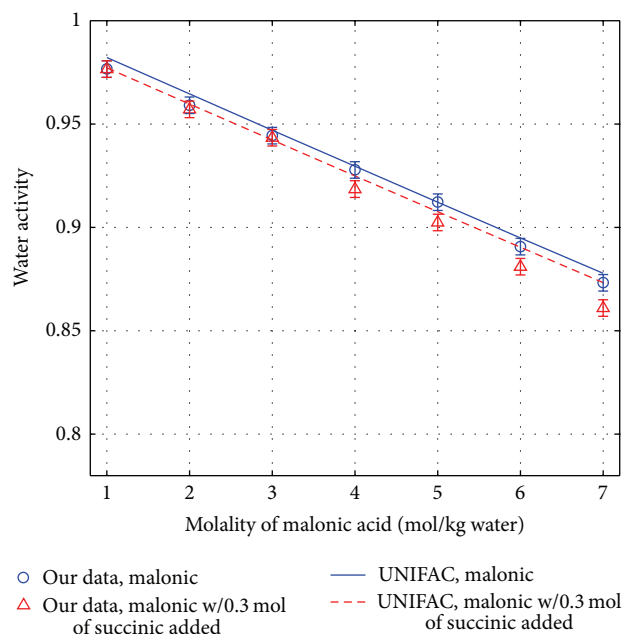


FIGURE 4: Water activity of malonic acid with and without succinic acid added. Each data point represents the average of 4 replicate measurements; error bars on measured data represent standard deviation of 0.4%.

3.4. *Mixture of Glutaric and Succinic Acid.* We also added 0.3 mol/kg water of succinic acid to 1 to 5 mol/kg water of glutaric acid solution. The modified UNIFAC model predictions for this mixture assume that the added succinic acid will take up water independently. However, as illustrated in Figure 5, our measurements show that the influence of a given concentration of succinic acid on water uptake systematically strengthened with glutaric acid concentration, although it only became significantly lower (with a decrease of 1.1%) at the 5 mol/kg level. These results indicate that the amount of water uptake due to succinic acid depends on the concentrations of other organic acids in the solution.

#### 4. Implications

We measured hygroscopic properties of three dicarboxylic acid mixtures (malonic/glutaric, malonic/succinic, and glutaric/succinic) using our bulk solution method. Our major findings are as follows.

- (1) While our pure malonic and glutaric acids solution data agree with UNIFAC to within 0.6% (for 0–7 mol/kg water) and 0.8% (for 0–5 mol/kg water), respectively, our measured water activity for mixtures of these two acids is lower than UNIFAC and ZSR predictions, by 1.6 and 2.3%, respectively.
- (2) The hygroscopicity of malonic/glutaric acid mixtures closely follows that of pure malonic acid alone.
- (3) In organic mixtures, succinic acid's effect on hygroscopicity becomes more pronounced as the concentration of a second, more soluble acid is increased.

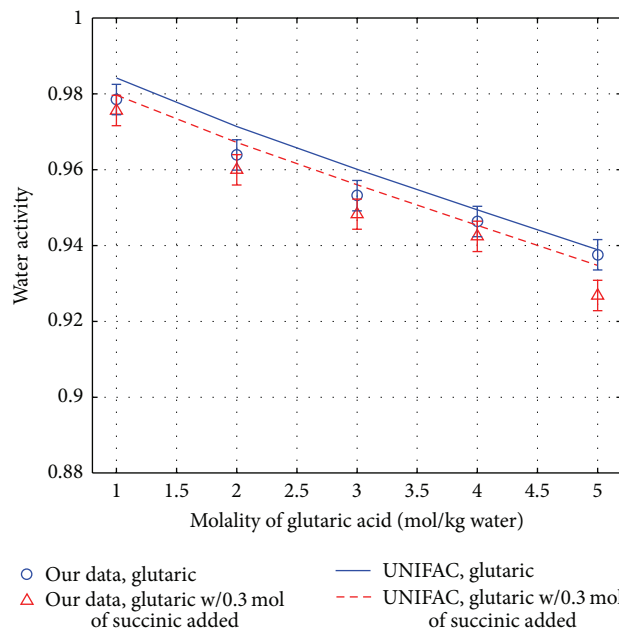


FIGURE 5: Water activity of glutaric acid with and without succinic acid added. Each data point represents the average of 4 replicate measurements; error bars on measured data represent standard deviation of 0.4%.

Our findings lend support to the hypothesis that interactions between different species of organics in a mixed solution can cause measurable alterations in hygroscopic behavior.

One possible cause for the trends observed in the hygroscopic properties of these mixtures may involve changes in the surface population of organics. We hypothesize that when two different organic acids are present in solution, they may exhibit a greater tendency to accumulate at the surface, leaving less surface area available for water molecules. Partial support for this hypothesis stems from the hydrophobic behavior of hydrocarbons, as illustrated in Figure 6(a), that is, their tendency to minimize the disruption of hydrogen bonds between water molecules by either staying at the solution surface or staying together [38].

For mixtures of organics in solution, the same mechanism drives less-polar molecules to the surface, or together. However, in this case, driving the different types of acid molecules together is less effective in terms of reducing the contact area and increasing the entropy (Figure 6(b)). As a result, the molecules are more likely to be driven to the surface than to be driven close to each other. Thus when two different organic acids are present in solution, they will exhibit a tendency to accumulate at the surface, leaving less surface area available for water molecules.

This surface population behavior would explain why our measured water activities for the malonic/glutaric mixtures are lower than UNIFAC and ZSR predictions. For the succinic/malonic and succinic/glutaric mixtures, the effect of a set concentration of succinic acid on water vapor suppression increases as the second acid's concentration is increased, suggesting that the number of succinic acid molecules at the surface is increasing.

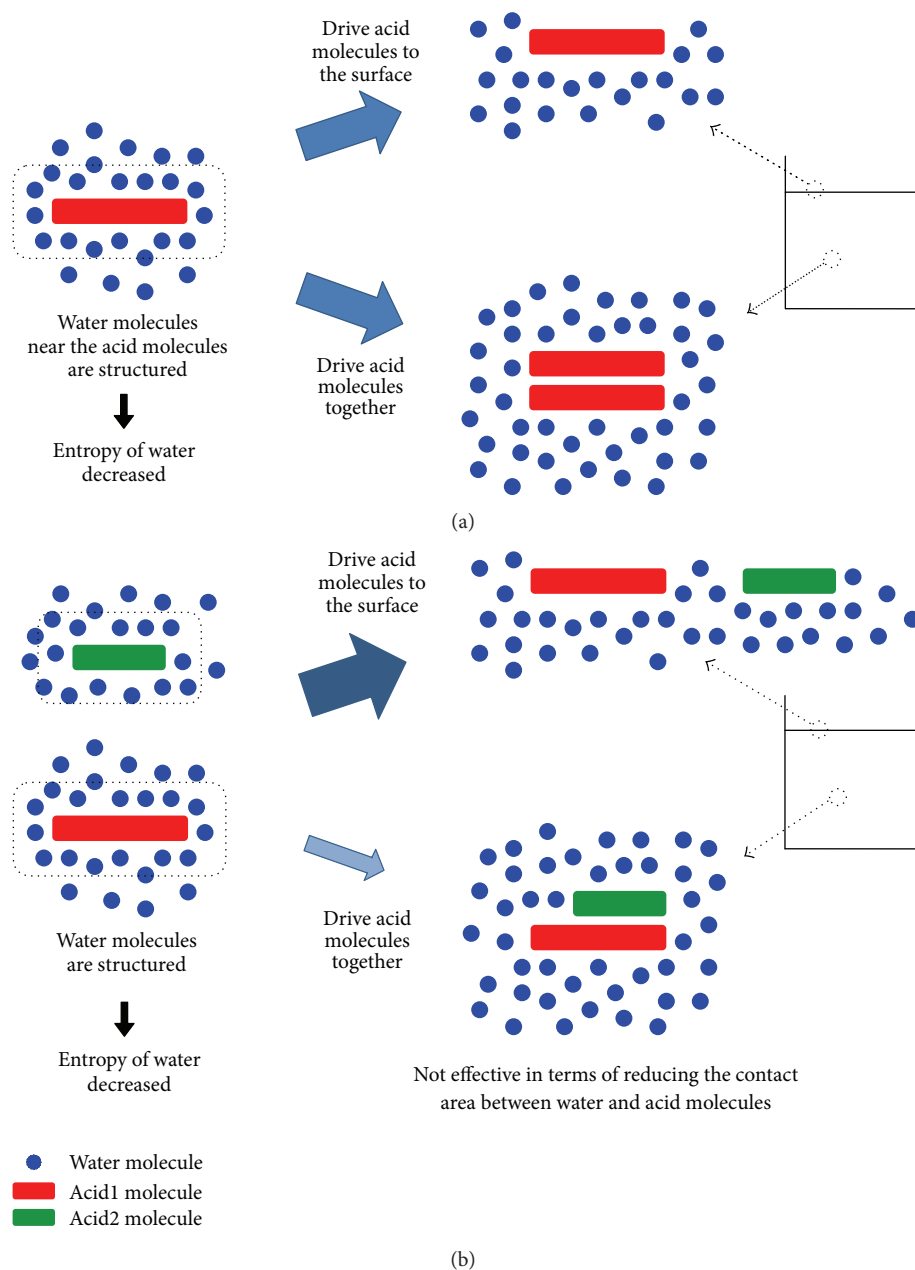


FIGURE 6: Illustration of hydrophobic effect for (a) a single-compound solution and (b) a mixed solution. The width of each arrow reflects the strength of that pathway.

Our results support the hypothesis that reliable estimates of the hygroscopic behavior of an organic solution mixture cannot be solely based on the behavior of individual organics but must include the interactions between the organics in the solution. Modeling approaches which do not consider species interactions, like UNIFAC and ZSR, were found in our study to systematically overestimate the water activity for dicarboxylic acid mixtures in solution, by up to 2.3%.

## 5. Conclusions

In this study, we observed systematic differences between measured and modeled hygroscopic behavior for three dicarboxylic acid mixtures, over a range of concentrations. While

the two-component organic mixtures examined here are much simpler than real atmospheric aerosols, our results suggest that interactions between different organic components must be considered in order to accurately model aerosol hygroscopicity. Further measurements are needed, involving more diverse mixtures of organics and inorganics [39], to better understand and characterize these interactions between species.

## Acknowledgments

Funding for this research came from National Science Foundation (Grant ATM-0731451). The authors would like to

thank Martin Reinhard and David M. Golden for their help throughout this research.

## References

- [1] Intergovernmental Panel on Climate Change (IPCC), "Climate Change 2007: the physical science basis, Working group I contribution to the fourth assessment," Cambridge University Press, 2007.
- [2] M. Kanakidou, J. H. Seinfeld, S. N. Pandis et al., "Organic aerosol and global climate modelling: a review," *Atmospheric Chemistry and Physics*, vol. 5, no. 4, pp. 1053–1123, 2005.
- [3] T. Novakov and J. E. Penner, "Large contribution of organic aerosols to cloud-condensation-nuclei concentrations," *Nature*, vol. 365, no. 6449, pp. 823–826, 1993.
- [4] D. S. Covert, R. J. Charlson, and N. C. Ahlquist, "A study of the relationship of chemical composition and humidity to light scattering by aerosols," *Journal of Applied Meteorology*, vol. 11, pp. 968–976, 1972.
- [5] G. Hänel, "The properties of atmospheric aerosol particles as functions of the relative humidity at thermodynamic equilibrium with the surrounding moist air," *Advances in Geophysics*, vol. 19, no. C, pp. 73–188, 1976.
- [6] Y. Kitamori, M. Mochida, and K. Kawamura, "Assessment of the aerosol water content in urban atmospheric particles by the hygroscopic growth measurements in Sapporo, Japan," *Atmospheric Environment*, vol. 43, no. 21, pp. 3416–3423, 2009.
- [7] I. N. Tang, "Chemical and size effects of hygroscopic aerosols on light scattering coefficients," *Journal of Geophysical Research D*, vol. 101, no. 14, pp. 19245–19250, 1996.
- [8] M. O. Andreae and D. Rosenfeld, "Aerosol-cloud-precipitation interactions. Part 1. The nature and sources of cloud-active aerosols," *Earth-Science Reviews*, vol. 89, no. 1–2, pp. 13–41, 2008.
- [9] J.-P. Putaud, F. Raes, R. Van Dingenen et al., "A European aerosol phenomenology-2: chemical characteristics of particulate matter at kerbside, urban, rural and background sites in Europe," *Atmospheric Environment*, vol. 38, no. 16, pp. 2579–2595, 2004.
- [10] J. Sun and P. A. Ariya, "Atmospheric organic and bio-aerosols as cloud condensation nuclei (CCN): a review," *Atmospheric Environment*, vol. 40, no. 5, pp. 795–820, 2006.
- [11] C. F. Braban, M. F. Carroll, S. A. Styler, and J. P. D. Abbatt, "Phase transitions of malonic and oxalic acid aerosols," *Journal of Physical Chemistry A*, vol. 107, no. 34, pp. 6594–6602, 2003.
- [12] Y. Wang, G. Zhuang, S. Chen, Z. An, and A. Zheng, "Characteristics and sources of formic, acetic and oxalic acids in PM<sub>2.5</sub> and PM<sub>10</sub> aerosols in Beijing, China," *Atmospheric Research*, vol. 84, no. 2, pp. 169–181, 2007.
- [13] S. Yu, "Role of organic acids (formic, acetic, pyruvic and oxalic) in the formation of cloud condensation nuclei (CCN): a review," *Atmospheric Research*, vol. 53, no. 4, pp. 185–217, 2000.
- [14] C. Peng, M. N. Chan, and C. K. Chan, "The hygroscopic properties of dicarboxylic and multifunctional acids: measurements and UNIFAC predictions," *Environmental Science and Technology*, vol. 35, no. 22, pp. 4495–4501, 2001.
- [15] M. Mochida and K. Kawamura, "Hygroscopic properties of levoglucosan and related organic compounds characteristic to biomass burning aerosol particles," *Journal of Geophysical Research D*, vol. 109, no. 21, 2004.
- [16] A. J. Prenni, P. J. DeMott, S. M. Kreidenweis, D. E. Sherman, L. M. Russell, and Y. Ming, "The effects of low molecular weight dicarboxylic acids on cloud formation," *Journal of Physical Chemistry A*, vol. 105, no. 50, pp. 11240–11248, 2001.
- [17] M. N. Chan and C. K. Chan, "Mass transfer effects on the hygroscopic growth of ammonium sulfate particles with a water-insoluble coating," *Atmospheric Environment*, vol. 41, no. 21, pp. 4423–4433, 2007.
- [18] M. Y. Choi and C. K. Chan, "The effects of organic species on the hygroscopic behaviors of inorganic aerosols," *Environmental Science and Technology*, vol. 36, no. 11, pp. 2422–2428, 2002.
- [19] M. Y. Choi and C. K. Chan, "Continuous measurements of the water activities of aqueous droplets of water-soluble organic compounds," *Journal of Physical Chemistry A*, vol. 106, no. 18, pp. 4566–4572, 2002.
- [20] C. N. Cruz and S. N. Pandis, "Deliquescence and hygroscopic growth of mixed inorganic-organic atmospheric aerosol," *Environmental Science and Technology*, vol. 34, no. 20, pp. 4313–4319, 2000.
- [21] H.-C. Hansson, M. J. Rood, S. Koloutsou-Vakakis, K. Hämeri, D. Orsini, and A. Wiedensohler, "NaCl aerosol particle hygroscopicity dependence on mixing with organic compounds," *Journal of Atmospheric Chemistry*, vol. 31, no. 3, pp. 321–346, 1998.
- [22] A. J. Prenni, P. J. DeMott, and S. M. Kreidenweis, "Water uptake of internally mixed particles containing ammonium sulfate and dicarboxylic acids," *Atmospheric Environment*, vol. 37, no. 30, pp. 4243–4251, 2003.
- [23] S. Sjogren, M. Gysel, E. Weingartner et al., "Hygroscopic growth and water uptake kinetics of two-phase aerosol particles consisting of ammonium sulfate, adipic and humic acid mixtures," *Journal of Aerosol Science*, vol. 38, no. 2, pp. 157–171, 2007.
- [24] C. Marcolli, B. Luo, and T. Peter, "Mixing of the organic aerosol fractions: liquids as the thermodynamically stable phases," *Journal of Physical Chemistry A*, vol. 108, no. 12, pp. 2216–2224, 2004.
- [25] R. H. Moore and T. M. Raymond, "HTDMA analysis of multicomponent dicarboxylic acid aerosols with comparison to UNIFAC and ZSR," *Journal of Geophysical Research D*, vol. 113, no. 4, Article ID D04206, 2008.
- [26] B. Svenningsson, J. Rissler, E. Swietlicki et al., "Hygroscopic growth and critical supersaturations for mixed aerosol particles of inorganic and organic compounds of atmospheric relevance," *Atmospheric Chemistry and Physics*, vol. 6, no. 7, pp. 1937–1952, 2006.
- [27] R. H. Stokes and R. A. Robinson, "Interactions in aqueous nonelectrolyte solutions. I. Solute-solvent equilibria," *Journal of Physical Chemistry*, vol. 70, no. 7, pp. 2126–2131, 1966.
- [28] A. Fredenslund, R. L. Jones, and J. M. Prausnitz, "Group-contribution estimation of activity coefficients in nonideal liquid mixtures," *AIChE Journal*, vol. 21, no. 6, pp. 1086–1099, 1975.
- [29] D. R. Lide, *CRC Handbook of Chemistry and Physics*, Taylor and Francis, Boca Raton, Fla, USA, 89th edition, 2009.
- [30] P. Saxena and L. M. Hildemann, "Water-soluble organics in atmospheric particles: a critical review of the literature and application of thermodynamics to identify candidate compounds," *Journal of Atmospheric Chemistry*, vol. 24, no. 1, pp. 57–109, 1996.
- [31] M. E. Wise, J. D. Surratt, D. B. Curtis, J. E. Shilling, and M. A. Tolbert, "Hygroscopic growth of ammonium sulfate/dicarboxylic acids," *Journal of Geophysical Research*, vol. 108, no. D20, Article ID 4638, 2003.

- [32] H. D. Burrows, "Studying odd-even effects and solubility behavior using  $\alpha,\omega$ -dicarboxylic acids," *Journal of Chemical Education*, vol. 69, no. 1, pp. 69–73, 1992.
- [33] J. P. D. Abbatt, K. D. Beyer, A. F. Fucaloro et al., "Interaction of HCl vapor with water-ice: implications for the stratosphere," *Journal of Geophysical Research-Atmospheres*, vol. 97, pp. 15819–15826, 1992.
- [34] R. Zhang, P. J. Wooldridge, J. P. D. Abbatt, and M. J. Molina, "Physical chemistry of the  $\text{H}_2\text{SO}_4/\text{H}_2\text{O}$  binary system at low temperatures: stratospheric implications," *Journal of Physical Chemistry*, vol. 97, no. 28, pp. 7351–7358, 1993.
- [35] R. Zhang, P. J. Wooldridge, and M. J. Molina, "Vapor pressure measurements for the  $\text{H}_2\text{SO}_4/\text{HNO}_3/\text{H}_2\text{O}$  and  $\text{H}_2\text{SO}_4/\text{HCl}/\text{H}_2\text{O}$  systems: incorporation of stratospheric acids into background sulfate aerosols," *Journal of Physical Chemistry*, vol. 97, no. 32, pp. 8541–8548, 1993.
- [36] A. S. Ansari and S. N. Pandis, "Water absorption by secondary organic aerosol and its effect on inorganic aerosol behavior," *Environmental Science and Technology*, vol. 34, no. 1, pp. 71–77, 2000.
- [37] I. R. Zamora, A. Tabazadeh, D. M. Golden, and M. Z. Jacobson, "Hygroscopic growth of common organic aerosol solutes, including humic substances, as derived from water activity measurements," *Journal of Geophysical Research D*, vol. 116, no. 23, Article ID D23207, 2011.
- [38] P. Joos, *Dynamic Surface Phenomena*, VSP, Utrecht, The Netherlands, 1999.
- [39] J. Y. Lee and L. M. Hildemann, "Surface tension of solutions containing dicarboxylic acids with ammonium sulfate, D-glucose, or humic acid," *Journal of Aerosol Science*. In press.

## Research Article

# Identification and Characterization of Black Carbon Aerosol Sources in the East Baltic Region

Steigvilė Byčenkienė, Vidmantas Ulevicius, Vadimas Dudoitis, and Julija Pauraitė

Center for Physical Sciences and Technology, Savanorių 231, LT-02300 Vilnius, Lithuania

Correspondence should be addressed to Vidmantas Ulevicius; ulevicv@ktl.mii.lt

Received 19 February 2013; Accepted 27 April 2013

Academic Editor: Giulia Pavese

Copyright © 2013 Steigvilė Byčenkienė et al. This is an open access article distributed under the Creative Commons Attribution License, which permits unrestricted use, distribution, and reproduction in any medium, provided the original work is properly cited.

One-year continuous measurements of aerosol black carbon (BC) at the background site Preila (55°55'N, 21°00'E, 5 m a.s.l., Lithuania) were performed. Temporal and spatial evolution and transport of biomass burning (BB) and volcanic aerosols observed within this period were explained by the air mass backward trajectory analysis in conjunction with the fire detection data produced by the MODIS Rapid Response System and AERONET database. The surface measurements and analysis of the Angström exponent of the absorption coefficient done separately for shorter and longer wavelengths (i.e.,  $\alpha = 370\text{--}520$  nm and  $\alpha = 660\text{--}950$  nm) showed that high levels of aerosol BC were related to the transport of air masses rich in BB products from Ukraine caused by active grass burning. During the events the highest mean values of the Angström exponent of the absorption coefficients  $\alpha_{370\text{--}520}$  and  $\alpha_{590\text{--}950}$  nm were observed ( $2.4 \pm 0.1$  and  $1.5 \pm 0.1$ , resp.). The ash plume of the Grimsvötn eruption on May 21, 2011 offered an exceptional opportunity to characterize the volcanic aerosols. The largest ash plume (in terms of aerosol optical thickness) over Lithuania was observed at May 24/25, 2011. The highest values of the Angström exponent of the absorption coefficients  $\alpha_{370\text{--}520}$  and  $\alpha_{590\text{--}950}$  nm were reached ( $1.3 \pm 0.1$  and  $1.4 \pm 0.1$ , resp.).

## 1. Introduction

Atmospheric aerosol particles, which are very small and suspended in the air, affect Earth's climate directly by scattering and absorbing the atmospheric radiation and indirectly by acting as cloud condensation nuclei and modifying the optical properties of clouds. Furthermore, human exposure to fine particulate matter is associated with adverse impacts on human health [1–3] and the environment (climate, visibility, and biogeochemical cycles) [4].

High concentrations of carbonaceous particles, containing BC or organic compounds (OC) (organic carbon), are found mainly in the submicron size range. The main natural sources of BC are volcanic eruptions, forest fires, and so forth. Wildfires (biomass burning) emit a variety of trace gases and particulates [5–9]. The growing recognition of BB as a widespread and significant agent of change in Earth's system has led to an ongoing need for fire data on the regional, continental, and global scale. Due to high sorption capacity and optical properties, black carbon originated from BB is of

great importance to the atmosphere processes and is a good indicator of anthropogenic air pollutants. Black carbon from BB alters chemical and physical properties of the atmosphere and snow albedo.

The eruption of Grimsvötn in Iceland (May 21, 2011) initiated a great number of research activities to characterize the physical, chemical, and optical properties of airborne volcanic material associated with this eruption. The main challenge in measuring volcanic material in the surface air is that this material is always mixed with other pollutants present in the air. A large fraction of carbonaceous component of the aerosol (in upper troposphere/lower stratosphere) was identified by Murphy et al. [10] and Martinsson et al. [11]. Volcanic eruptions inject large quantities of ash and gases into the atmosphere. Despite the evident significances of carbonaceous aerosol in air chemistry and physics, information concerning their temporal variability is still quite incomplete.

The long-range transport (LRT) of atmospheric particulate matter (PM) is a transboundary problem that can have significant impacts on  $PM_{10}$  and  $PM_{2.5}$  levels in background

European areas [12]. LRT can cause high  $PM_{2.5}$  concentration peaks when air masses arrive under suitable meteorological conditions from regions with high emissions of particles and/or their precursor gases. Many research studies have been performed and reported for the background atmospheric monitoring of LRT [13–15]. Long-range transport of emissions from agricultural fires and volcanoes to Europe was recognized previously in USA, Europe, and Russia [16–20]. In addition to European transport, LRT of smoke from Russian biomass burning has been recorded in Mongolia, China, Japan, and Korea [21], and studies have revealed that hemispheric-scale transport is possible [16]. As the mass concentrations of fine particles are commonly lower in Northern Europe countries compared with those in Central Europe [22, 23], LRT can have a notable impact on the aerosol particle levels under favorable conditions [23, 24]. The LRT of emissions from wildfires from the Ukraine and European part of Russia frequently increases the particulate matter concentrations in these countries during spring and summer [25–27]. Volcanic dust plumes can also be transferred over long distances by air masses, affecting the air quality not only over Europe but in other parts of the world as well [28].

Combining the variety of terrestrial information operationally derived from satellite data including those from NASA's MODIS instrument enables linking the different temporal and spatial scales. The use of the Angström exponent  $\alpha$  has significantly increased in the last years, because this parameter is easily estimated using automated-surface sun photometry, while it is becoming increasingly accessible to satellite retrievals [29]. Moreover, the value of the Angström exponent is a qualitative indicator of the aerosol particle size or fine mode fraction [30].

In this work, the pollution events due to biomass burning that occurred in Lithuania on March 21–25, 2011 and pollution episode caused by long-range transported volcanic material from the Grimsvötn eruption that took place at the end of May 2011 in Iceland were investigated. Air mass backward trajectories, fire satellite observations, dispersion modeling results, and emission source data were used to identify the source. The mass and number concentrations of  $PM_{2.5}$  in conjunction with Angström exponent of the absorption coefficient and other optical properties of aerosol were studied.

## 2. Methodology

**2.1. Site Description.** The aerosol particle concentration measurements were performed at the Preila environmental pollution research station (55°55'N, 21°00'E, 5 m above sea level) in the coastal/marine environment. This station is located on the Curonian Spit, which separates the Curonian Lagoon and the Baltic Sea, and thus can be characterized as a regionally representative background area. The Curonian Lagoon, the largest coastal bay in the Baltic Sea, is a highly eutrophied water body. One of the nearest industrial cities, Klaipėda, is at a distance of about 40 km to the north, and the other major city, Kaliningrad, is 90 km to the south from Preila.

**2.2. Long-Range Transport and Air Mass Backward Trajectories.** Air mass backward trajectory analysis provides a better

understanding of air flow and long-range transport patterns during the events. We analyzed the aerosol characteristics with respect to categorized air mass backward trajectories for the initial estimation of the wildfire and volcanoes potential source locations and quantitative contribution. Backward trajectories were produced using the Flextra model (NILU; Institute of Meteorology and Geophysics, Vienna) [31] and meteorological data provided from ECMWF (European Centre for Medium Range Weather Forecast). The potential source areas of long-range transported pollution were studied using 7-day backward air mass trajectories with a starting height of 500, 1000, and 1500 m above the ground level. Trajectories were produced at 6 h intervals for each event. The height along the trajectories is indicated by colour (colour/height scale in the lower left corner of the plot). Each 3-hour interval along the trajectory path is indicated by a small legend and each 24-hour interval by a big legend.

To identify possible events of regional transport, hotspot/fire the location of a thermal anomaly was detected by MODIS using data from the middle infrared and thermal infrared bands [32]. Each MODIS sensor achieves global coverage once per day and once per night every 24 h. Therefore, most fires detectable at a 1 km spatial resolution have the potential to have their FRP (Fire Radiative Power) measured four times a day. Figure 2 shows the locations of the active fires identified from MODIS observations during study events over the area of our interest. The MODIS monthly fire maps, available since 2001, showed that these events of biomass burning in March–April occurred annually. However, the duration, geographical extent, and emission of the smoke from these fires differ year by year.

The AEROSOL ROBOTIC NETWORK (AERONET) is a ground-based network of Cimel sun photometer that measures the extinction aerosol optical depth at 7 wavelengths  $\lambda$  (340, 380, 440, 500, 670, 870, and 1020 nm) from the direct sun measurements over locations. The AOD measurements are accurate to within  $\pm 0.01$ . The size distribution of aerosols can be estimated from spectral AOD (typically 440–870 nm). The negative slope of AOT with the wavelength on a logarithmic scale is known as the Angström parameter ( $\alpha$ ). This parameter (1) can be calculated from two or more wavelengths using the least squares fit. Values of  $\alpha > 2.0$  indicate that fine mode particles exist (e.g., smoke particles and sulphates), while values of  $\alpha$  near zero indicate the presence of coarse mode particles such as desert dust [33]:

$$\alpha = -\frac{d \ln \tau_a}{d \ln \lambda} = -\frac{\ln(\tau_{a2}/\tau_{a1})}{\ln(\lambda_2/\lambda_1)}, \quad (1)$$

where  $\alpha$  is the wavelength exponent depending on the ratio of the particle coarse mode to the accumulation (small) one (Angström parameter),  $\tau_a$  is the AOD and  $\lambda$  is the wavelength.

The Navy Aerosol Analysis and Prediction System (NAAPS) model results were used to determine the distribution of aerosols from fires and volcanoes (model description and results are available from the web pages of the Naval Research Laboratory, Monterey, CA, USA; <http://www.nrlmry.navy.mil/aerosol/>). The NAAPS model

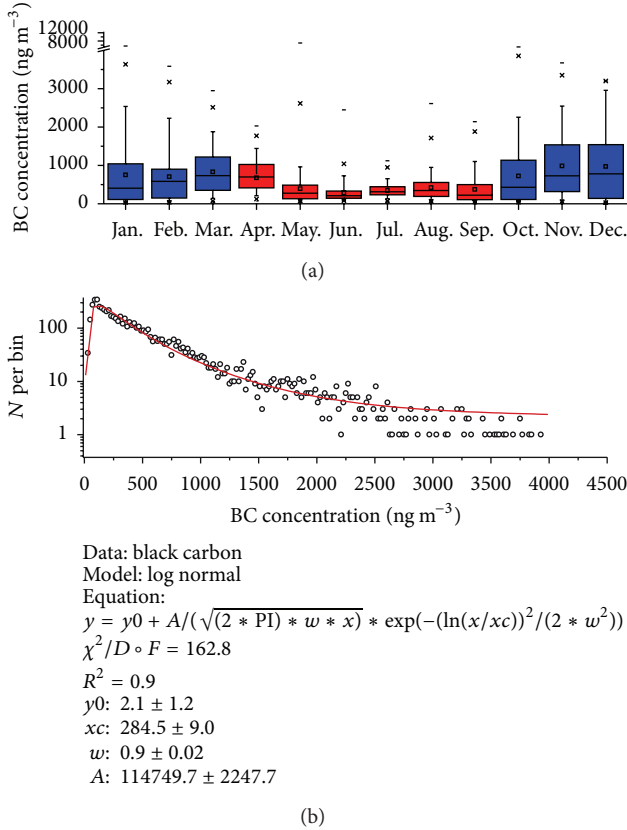


FIGURE 1: (a) Box and whisker plots for comparison of mass concentrations at Preila; (b) BC concentration frequency distribution.

has been modified to incorporate real-time observations of biomass burning based on the joint Navy/NASA/NOAA Fire Locating and Modeling of Burning Emissions system (FLAMBE, <http://www.nrlmry.navy.mil/aerosol/>) [34]. The method has proven to be helpful in previous studies of long-range and regional transport of smoke [35].

**2.3. Black Carbon and Aerosol Particle Size Distribution Measurements.** A Magee Scientific Company Aethalometer, Model AE31 Spectrum, manufactured by Optotek, Slovenia, was deployed at the Vilnius site and provided real-time, continuous measurements of the BC mass concentrations. The optical transmission of carbonaceous aerosol particles was measured sequentially at seven wavelengths  $\lambda$  (370, 450, 520, 590, 660, 880, and 950 nm). The 880 nm is considered as the standard channel for BC measurements as at this wavelength BC is the principal absorber of light. The Aethalometer output is calculated directly as the BC concentrations through an internal conversion use assumed mass absorption efficiency. The Aethalometer converts light attenuation to the BC mass using a fixed specific attenuation cross-section ( $\sigma$ ) of  $16.6 \text{ m}^2 \text{ g}^{-1}$  of BC (Aethalometer Operations manual, Magee Scientific) [36].

This is the default value set by the manufacturer for a wavelength of 880 nm. The Aethalometer data recorded with a 5-minute time base were compensated for loading effects

using an empirical algorithm [36]. The Aethalometer was equipped with an additional impactor removing the particles larger than  $2.5 \mu\text{m}$  of the particle aerodynamic diameter. The starting time referred in this paper is Greenwich Mean Time (for local time: GMT +2:00).

The absorption coefficient  $b_{\text{abs}}$  for airborne particles is defined with Lambert-Beer's law as follows:

$$I = I_0 e^{(-b_{\text{abs}} x)}, \quad (2)$$

where  $I_0$  is the intensity of the incoming light and  $I$  is the remaining light intensity after passing through a medium with thickness  $x$ .

A power law fit is commonly applied to describe the wavelength dependence of aerosol absorption coefficient  $b_{\text{abs}}$ :

$$b_{\text{abs}} \propto \lambda^{-\alpha}, \quad (3)$$

where  $\lambda$  is the wavelength and  $\alpha$  is the usually called Angström exponent of the absorption coefficient and is computed by fitting an exponential curve [37].

The aerosol size distribution was measured by using the Scanning Mobility Particle Sizer (SMPS) built by the Leibniz Institute for Tropospheric Research, Germany. The SMPS is composed of a differential mobility analyzer and CPC UF-02proto. This system had the following general specifications: size range: 8–900 nm; scan time: 5 min; resolution: 71 size channels.

### 3. Results

In general, BC particles are mainly produced by anthropogenic activities such as fossil fuel burning (industries and transport) and biomass burning (agriculture or wildfires). However, the natural sources such as wildfires and volcanic eruptions also contribute to the BC mass concentration, but their contributions are relatively much less. We focused on the strongest periods of wildfire and volcanic events. The first event occurred on April 24–30, 2011 and the second on May 25–27, 2011. The concentrations observed during both events are clear outliers in their respective series, both for hourly concentrations and 24 h means.

**3.1. Annual Variations of Aerosol Black Carbon.** Box and whisker plots of BC concentrations and mass concentration frequency distribution are shown in Figures 1(a) and 1(b). The range of the box depicts the bounds of the 25th and the 75th percentiles of the data. The whiskers extending from the box represent the bounds of the 10th and the 90th percentiles.

The median and outliers of each dataset are also shown. It can be clearly seen that higher concentrations of BC are observed during October to March, when cold weather conditions prevail during any year.

The concentration shows a decrease in June ( $280 \pm 230 \text{ ng m}^{-3}$ ), with the monthly mean BC concentration falling to more than half the value that prevailed in cold months. This low value is maintained until September. During this period no influence of residential heating was observed at the site. The mean BC concentration during this period is

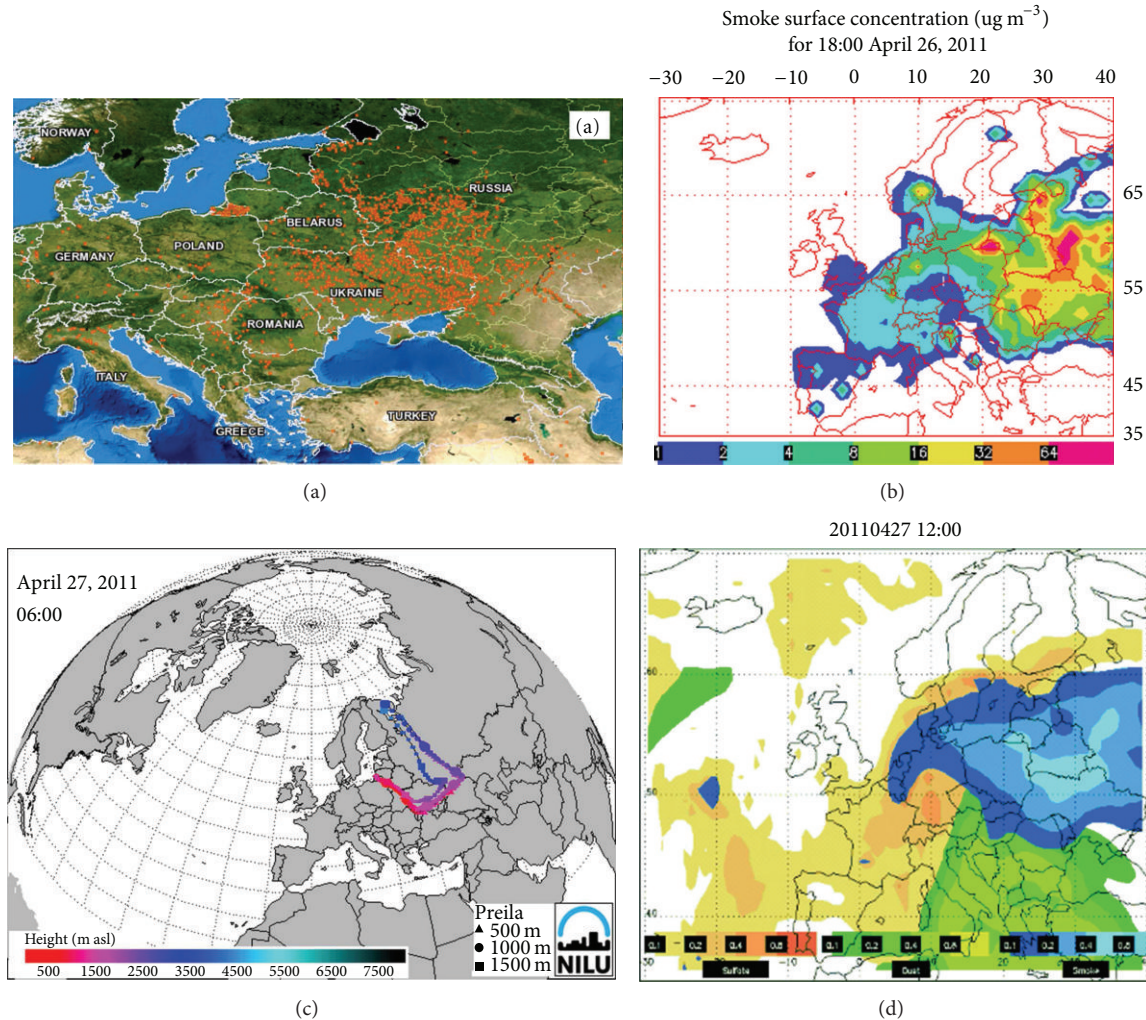


FIGURE 2: Active fires detected during April 24–30, 2011 during high BC concentration event: (a) by the MODIS Rapid Response System, ((b), (d) sulphate, dust, and smoke surface concentration ( $\mu\text{g m}^{-3}$ ) for 18:00 April 26 2011, and (c) 7-day air mass backward trajectories to Preila (at 500, 1000, and 1500 m AGL) during the event of grass fires.

$370 \pm 300 \text{ ng m}^{-3}$  in contrast to the value of  $750 \pm 550 \text{ ng m}^{-3}$  during cold months (in blue).

Taking  $25 \text{ ng m}^{-3}$  value as frequency statistics step, the frequency distribution map of hourly average concentration of BC aerosol is depicted in Figure 1(b). The frequency distribution of hourly average BC aerosol does not have normal characterization. Using the log-normal distribution function to fit the frequency distribution characteristics, results show that approximately 70% of the measurements hourly average concentrations of BC aerosols were found in a mode in a low range of concentrations centered at approximately  $200 \text{ ng m}^{-3}$  indicating a direct impact of local emissions from combustion activities at the station. Mean BC mass concentrations ( $580 \text{ ng m}^{-3}$ ) observed at Preila in 2011 are relatively low, comparable to that measured at the remote location. Comparing with the values reported from elsewhere for rural sites, mean BC values at Preila are comparable to that reported for Zappoli et al. [38] detected BC concentrations of  $600 \text{ ng m}^{-3}$  at a background site in Hungary (K-Puszt).

### 3.2. Spectroscopic Properties of Carbonaceous Aerosol

**3.2.1. April 24–30, 2011 Event.** Fire Mapper products have provided data about the location and extent of fires during the event days (Figure 2). Satellite images and model forecasts from NAAPS (Figures 2(b), 2(d)) for the study period suggested substantial emissions and LRT of smoke from the large fires burning in the southern part of Ukraine and Kaliningrad at that time.

Grass burning products were redistributed over Lithuania by the large-scale and regional atmospheric circulation. The air mass backward trajectory analysis showed that particles from BB with air masses in 3 days were brought to Lithuania and caused high peaks of aerosol number and BC concentrations. BC and aerosol number concentrations rose to higher levels over the whole territory of Lithuania. During this event the 1-hour average aerosol particle number concentration reached  $4000 \text{ cm}^{-3}$ , BC- $3500 \text{ ng m}^{-3}$ , while normally average concentration values are about  $3100 \text{ cm}^{-3}$  and  $580 \text{ ng m}^{-3}$ ,

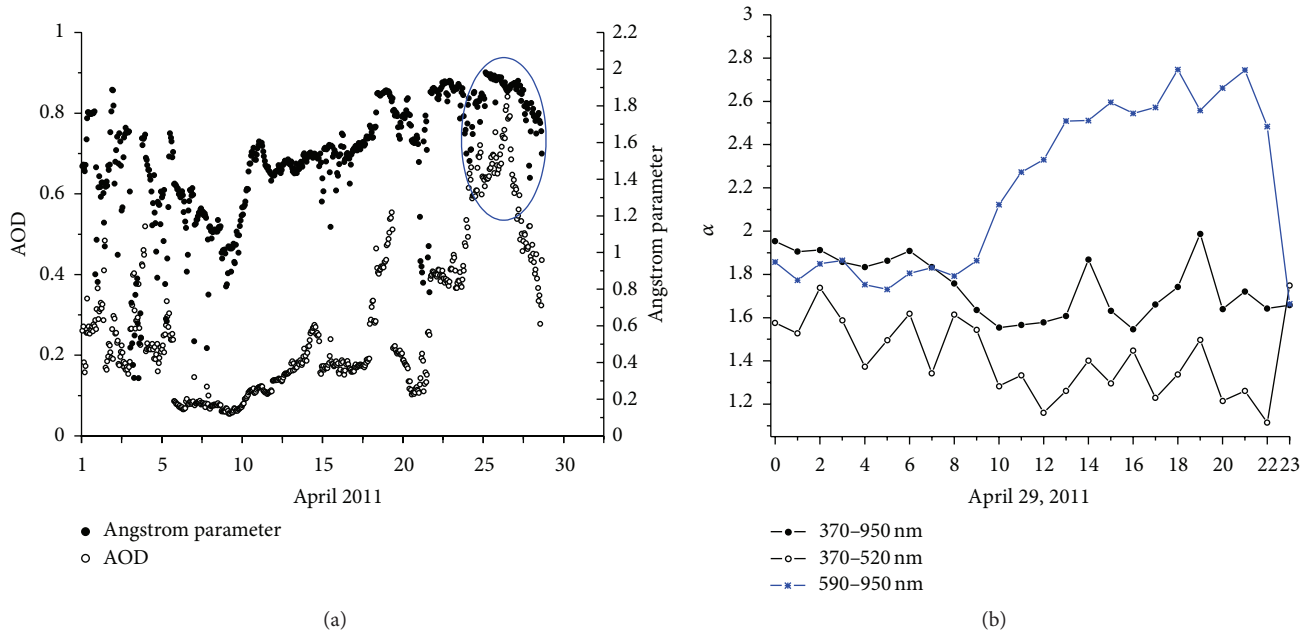


FIGURE 3: (a) The spectral variation of instantaneous measurements of AOD for April 2011 showing the gradual buildup and decline of smoke concentrations in this period (April 25–29, blue cycle); (b) values of the Angström exponent of the absorption coefficient (April 29, 2011) showing dynamic variations as a result of both increasing (decreasing) AOD and BC concentration and greater domination of fine mode versus coarse mode optical depth.

respectively. It should be noted that during April 24–30, 2011, urban sites belonging to the Lithuanian Automatic Urban Network (EPA) (<http://stoteles.gamta.lt/>) experienced peaks of  $PM_{10}$  concentration which coincided with extensive wildfires in Ukraine exceeding the European limit value 1.5 times.

Data analysis of the BC combined with TERRA/Moderate Resolution Imaging Spectroradiometer MODIS fire detections (Figure 2(a)) and NAAPS aerosol optical depth provided some insight into the aerosol regional transport of smoke. As shown in Figure 2(a), the MODIS clearly illustrates the fire location. The model forecasts from NAAPS for this period suggested substantial emissions and regional transport of smoke (Figure 2(c)) from the large fires burning in Kaliningrad and Ukraine regions at that time. During the study the NAAPS model predicted the optical depth of 0.6 at a wavelength of 0.55 microns for three components: sulfate and smoke over Europe due to smoke from the wildfires (Figure 2(d)). On the same days substantial concentrations of BC were observed during the period after air masses arrived from the fire location.

During the air mass transport to Lithuania, aerosol optical properties changed due to both deposition and mixing with local aerosols. The similar events were detected and studied by lidar networks covering the whole continent [39, 40] and also by a single lidar station [41]. Smoke plume was detected by the lidar and sun-photometric stations in Minsk, Belarus, Poland, and Belsk [42]. Belsk site is a joint AERONET site and it was possible to characterize the optical properties of aerosol particles at this site during our case study. From the first general overview of the field data, April

BB event can be recognized. In this study, the values of the Angström parameter were computed in the wavelength interval of 440–870 nm, using the AOD data of the selected AERONET Belsk site, applying the least-squares method. AERONET profiles of the absorption Angström parameter (indicator of the AOD spectral dependence and related to particle size predominance) and AOD values at 500 nm obtained from MODIS for a period between April 1 and 30, 2011 are presented in Figure 3(a). The AOD measured in Belsk reached  $0.90 \pm 0.02$  (these results are based on the AERONET cloud-screened and quality-assured data (level 2.0)). It can be seen that the Angström parameter values are mostly in the 1.4–2.0 range suggesting the presence of species that absorb more strongly at shorter wavelengths than black carbon, which might be associated with organics from biomass burning [43]. It is known that typical values of the Angström parameter range  $\sim 2$  for fresh smoke particles (accumulation mode) to  $\sim 0$  for coarse mode particles [33].

The wavelength dependence of the light absorption can be better approximated by separate exponential fits of the shorter (370–520 nm) and longer (660–950 nm) wavelengths obtained by an exponential curve fit over all 7 wavelengths. The Angstrom exponents were calculated by fitting  $b_{\text{abs}}$  for the whole available wavelength intervals: the short (370–520 nm) and long (590–950 nm) wavelength intervals (Figure 3(b)).

On the event day (April 29) the mean  $\alpha$  values were significantly larger for the longer wavelengths ( $\alpha_{590-960} = 2.2 \pm 0.1$ ) compared to the shorter wavelengths ( $\alpha_{370-520} = 1.4 \pm 0.1$ ). During the event day the highest values of  $\alpha_{590-960}$  were observed between 11 AM and 11 PM ( $2.7 \pm 0.1$ ) while the highest values of  $\alpha_{370-520}$  were observed

between midnight and morning ( $1.7 \pm 0.1$ ). On nonevent days, the light absorption coefficients  $\alpha_{370-950}$ ,  $\alpha_{370-520}$ , and  $\alpha_{660-950}$  nm were within a narrow range of 1.2, with weak diurnal cycles. For example,  $\alpha$  value up to 1.5 was observed at a high Alpine station during a Saharan dust event [44].

Kirchstetter et al. [45] reported  $\alpha$  value of 2.2 for outdoor firewood burning, 1.8 for a savanna fire, and 0.8–1.1 for traffic-dominated sites (measurements with six wavelengths between 370 and 850 nm). Schnaiter et al. [46, 47] reported  $\alpha$  value of 1.1 for uncoated diesel soot (measurements with  $\lambda = 450, 550, \text{ and } 700$  nm). Previous investigations showed that the type of wood being burned also influenced the  $\alpha$  value as shown by Day et al. [48] where they measured fresh wood smoke from seven types of forest wood with an Aethalometer ( $\lambda = 370-950$  nm) and reported  $\alpha$  values between 0.9 and 2.2. Hoffer et al. [49] calculated  $\alpha = 6-7$  for water-soluble humic-like substances (HULIS) isolated from the fine fraction of the biomass burning aerosol spectrophotometer measurement with  $\lambda = 300-700$  nm).

These very high values of the absorption exponent are indicative of biomass combustion [37] in our case—wildfires as indicated by the air mass backward trajectory analysis (Figure 1) [50, 51]. Though the increase in BC concentration associated with the BB event was instantaneous, the gradual decay after some days instantly recovered the BC concentration to the preevent level despite the fact of long atmospheric lifetime of BC. Reddy and Venkataraman [52] have found an annual average value of  $\sim 6.5 \pm 4.8$  days for the BC lifetime. Globally, the average lifetime of BC is about 8 days.

The observed variations in the Angström exponent at 590–950 nm derived from the BC measurements are not consistent with AERONET Angström parameter (Figures 3(a), 3(b)). These comparisons show that there are differences between these two techniques for obtaining column average aerosol optical properties. Every aerosol technique has its advantages and disadvantages. Some are inherent in the instrument design or measurement type (e.g., sun photometers cannot measure valid AOD during cloudy periods).

**3.2.2. May 24–27, 2011 Event.** Figure 4 shows the air mass arriving at Preila at 12:00 (02 GMT) on May 24–27, 2011. As illustrated in Figure 4, the air mass came from the northeast, passing over Grimsvötn from which it was two-three days before arrival at the site. Results confirm that the volcanic plume arrived during the night between May 25 and May 26, 2011 after 72 h of transportation. The arrival elevation of 500 m a.g.l. locates within the inversion layer so that it is representative of the air sampled at Preila.

The sulphate concentration in the air was used as an indicator of volcanic pollution as sulphur dioxide is the third most abundant gas in volcanic emissions, after water vapor and carbon dioxide [53]. One week after the eruption the  $\text{SO}_2$  cloud reached Europe, where it was detected by ground-based instruments. At the Preila station, the plume was first detected on May 24–25 as  $\text{SO}_2$  concentrations peaked until reaching a maximum value of  $1.36 \text{ mg m}^{-3}$  and made up 14% of submicron aerosol particles [20]. The advection of volcanic plumes from Grimsvötn was also confirmed using the satellite images. For the UV/visible instrument GOME-2

the Differential Optical Absorption Spectroscopy was used. After the eruption, the plume drifted to the southeast where it formed a distinct loop due to atmospheric winds. GOME-2 measured  $\text{SO}_2$  column amounts on May 29, of  $>10 \text{ DU}$  after 8 days after the eruption (<http://sacs.aeronomie.be/>). Time variations of sulphate AOD observed during May 17–31, 2011 showed that the AOD values were significantly larger on May 28–29, whereas extremely low sulphate concentrations prevailed during the period from 25 to 26 May. Thus, we conclude that the high values of sulphate AOD measurements measured during the first half of the observation period after eruption were caused by the volcanic plumes transported from Grimsvötn.

A carbonaceous aerosol component has been observed in fresh volcanic clouds from several volcanoes [11]. The Angström exponent of the absorption coefficient for organic species depends on the wavelength. Studies show  $\alpha$  value for organic species is larger than for black carbon [45], whereas it is less dependent on the wavelength for BC. The dependence of  $\alpha$  on the wavelength can be seen in Figure 5 for the study case.

Figure 5 shows time series for the hourly mean values of  $\alpha$  from May 24 to May 28, 2011. Since at the UV wavelength there could be some organic compound strongly absorbing, thus leading to an overestimation of the  $\alpha$  parameter, the wavelength range 370–950 nm has been considered for the best-fit technique application and  $\alpha$  parameter estimation. The fact that  $\alpha_{370-550}$  becomes higher than  $\alpha_{590-950}$  shows that the influence of the organic aerosols exists, but its influence is limited, probably connected to changes in variations in the composition of air masses crossing the Preila site. BC concentration maximum values (at 880 nm), depending on the day, were varying between 150 and  $1200 \text{ ng m}^{-3}$ . In Preila, mean  $\alpha_{370-550}$  values (Figure 5) collected in May 25–26, 2011 have been found to be  $\sim 1.9 \pm 0.5$  while measurements collected during May 24 and 27–28, 2011 give mean alpha value  $\sim 1.5 \pm 0.5$ . Hence, it can be concluded that low BC contributed mainly to the light absorption, which is well consistent with an average  $\alpha_{370-550}$  and  $\alpha_{590-950}$  close to 1.5 and 1.8, respectively. Explanation of the carbon content of the air other than direct volcanic emissions needs to be considered [54].

Parallel to the measurement of  $\alpha$ , the aerosol absorption coefficient  $b_{\text{abs}}(\lambda)$  was evaluated (Figure 6). The spectral dependence allows distinguishing carbonaceous aerosols from different sources because of light absorbing OC which in contrast to BC exhibits a stronger absorption at shorter wavelengths [43]. In the period during the volcanic activity the value of  $\alpha_{370-550}$  was slightly lower ( $1.3 \pm 0.3$ ) than that of  $\alpha_{590-950}$  ( $1.4 \pm 0.2$ ) and was contrary to the value after air masses passed the Preila site, that is,  $\alpha_{370-550}$  and  $\alpha_{590-950}$  nm of  $2.1 \pm 0.4$  and  $2.4 \pm 0.4$ , respectively. This is a strong suggestion that the aerosol includes less absorbers of the shorter wavelengths during the volcanic event. According to values of the Angström exponent of the absorption coefficients  $\alpha_{370-550}$  and  $\alpha_{590-950}$  nm along with the air mass backward trajectories calculation, we can assume that the decrease in the organic carbon concentration was caused by the volcano at Grimsvötn in Iceland.

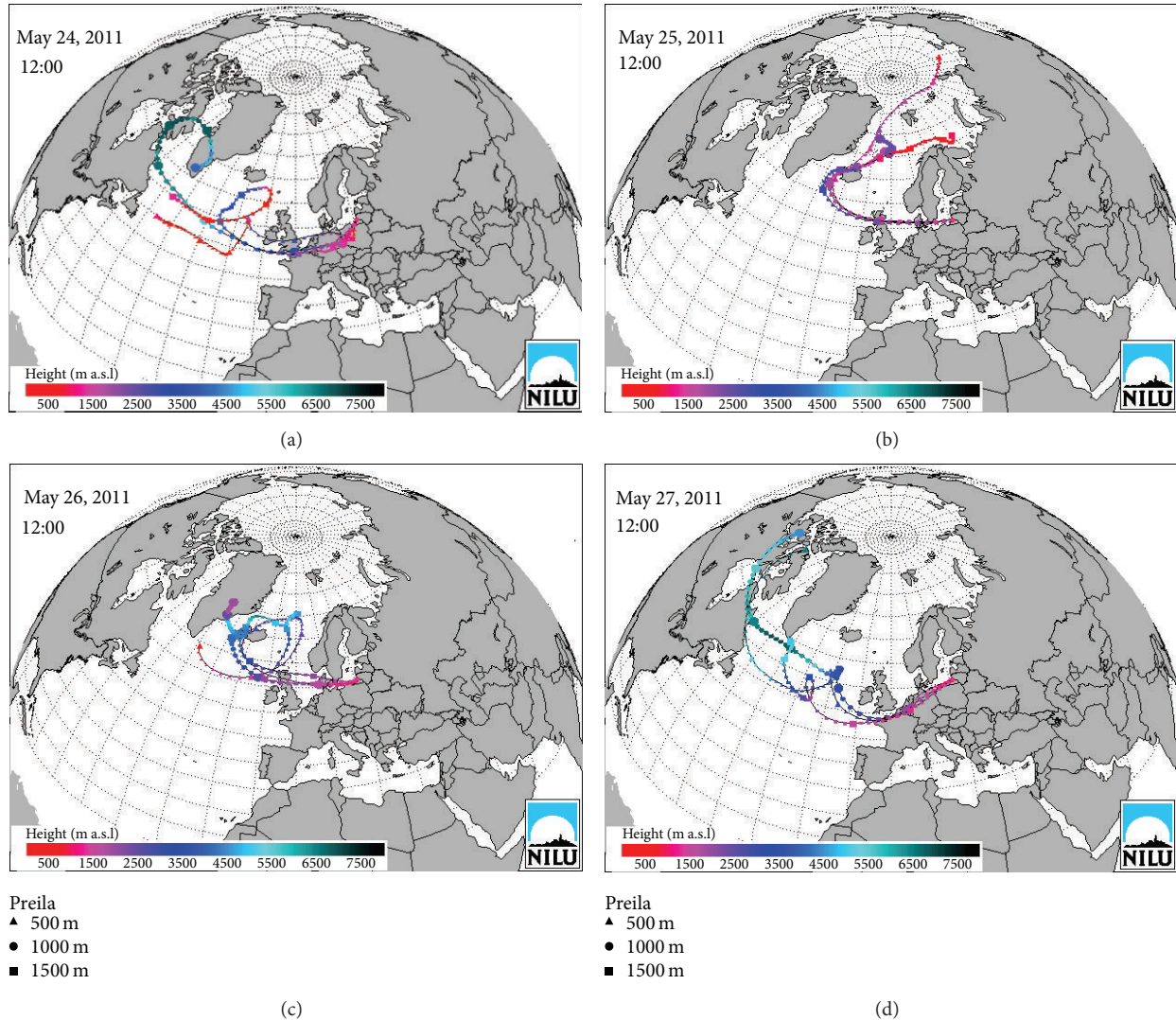


FIGURE 4: Backward trajectories of the air masses from the volcano at Grimsvötn to Lithuania on 24–27 ((a)–(d)) May 2011 (12:00 UTC).

It is to be noted that the Angstrom exponent could be a rough indicator of the size distribution of the aerosol particles whereas the Angström exponent of the absorption coefficient tells about the nature of absorbing aerosols. A low  $\alpha$  value ( $<1$ ) indicates dominance of larger-size particles and a high  $\alpha$  ( $>1$ ) indicates dominance of smaller-size particles [55]. This assumption was also confirmed in the study by Kvietkus et al. [20], when the particulate organic matter concentrations of  $PM_{10}$  were lower during the period of the volcanic eruption, but an increase in sulfate concentration from 1.13 to  $3.86 \mu\text{g m}^{-3}$  (90% of  $PM_{10}$ ) on May 25, in the Vilnius area was observed. Baker et al. [56] showed that in the volcanic cloud of Grimsvötn chlorine radicals rapidly depleted organic trace gases to levels well below background concentrations. This process could increase particulate carbon amount in the volcanic cloud. This could explain the increase in BC concentration in May 27 and parallel decrease in organic fraction (Figure 5).

Volcanic particles are assumed to be composed of ash particles and hygroscopic sulfates. Volcanic particles are injected in the atmosphere both as primary particles rapidly deposited due to their large sizes on time scales of minutes to a few weeks in the troposphere and as secondary particles mainly derived from the oxidation of sulphur dioxide [57]. For a detailed analysis of the event the diurnal pattern of the time dependent size distribution for Preila during May 24, 2011 is depicted in Figure 7. New particle formation events were found on 4 days (May 24–27). We will focus here on the event that we observed at the Preila station on May 24, 2011. In the morning of these days, air masses arrived to Preila from the Baltic Sea area when higher altitude (above 2000–3500 m a.s.l.) air masses continued to arrive straight from the Grimsvötn, the lower level (below 500 m a.s.l.). The aerosol also shows a high concentration of  $SO_2$  during the experiment when air masses came from the volcano accompanied with high sulphur ( $45.2 \mu\text{g m}^{-3}$ ).

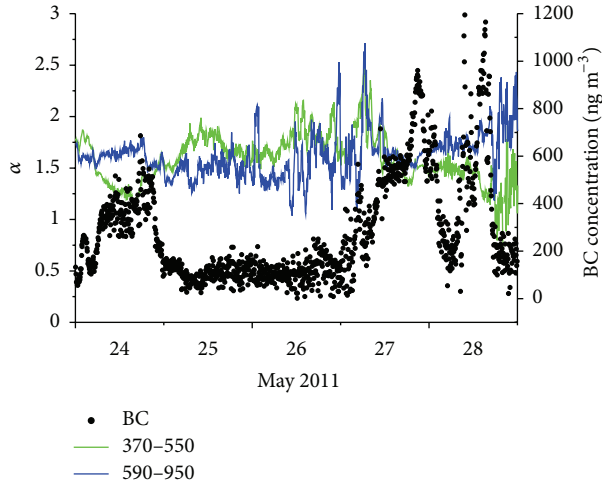


FIGURE 5: Time series of the hourly mean Angström exponent of the absorption coefficient on May 24–28, 2011.

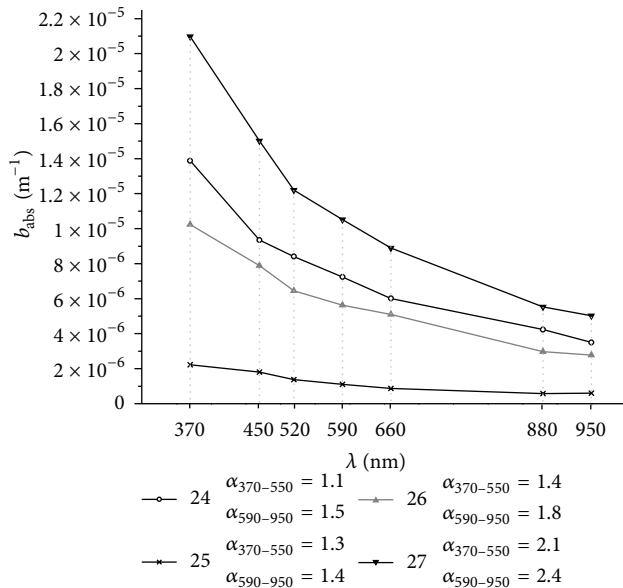
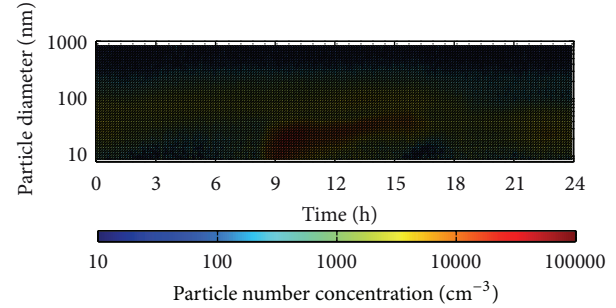


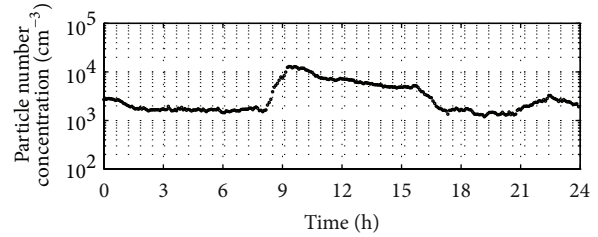
FIGURE 6: The light Angström exponent of the absorption coefficients  $\alpha_{370-520}$  and  $\alpha_{590-950}$  nm during May 24–27, 2011.

A very strong source of  $\text{SO}_2$  located in the southern maritime area is suspected to have caused these extraordinary high  $\text{SO}_2$  concentrations. As the sun is rising, photochemical reactions lead gas phase  $\text{SO}_2$  to be oxidized to sulfuric acid.

As shown in Figure 7, the night time 00:00–07:00 AM was associated with higher number concentration of accumulation mode particles ( $D_p \sim 100$  nm). During new particle formation events, the nucleation mode particles showed an obvious one-peak diurnal variation: the number concentration was very low in the early morning, started to increase abruptly at about 9:00 in the morning, and reached its maximum to a value of  $30,000 \text{ cm}^{-3}$ . On the contrary the concentration of Aitken mode particles remained low between 00:00 and 9:00 A.M. After this point, the formation



(a)



(b)

FIGURE 7: Contour plot of new particle formation and growth on 24 May 2011; colour represents logarithm of concentration in  $\text{cm}^{-3}$ .

TABLE 1: The growth rate of new particles.

|                                 | Date   |        |        |        |
|---------------------------------|--------|--------|--------|--------|
|                                 | 24 May | 25 May | 26 May | 27 May |
| Growth rate, $\text{nm h}^{-1}$ | 5.36   | 2.55   | 5.58   | 25.20  |

of new particles started and the concentration of nucleation mode particles increased. Later the number of concentrations reached its lowest level from 6:00 P.M. till the next morning. The growth rates (Table 1) of new particles were calculated using the method described by Kulmala et al. [58].

The growth rates were in the range of  $2.55\text{--}25.20 \text{ nm h}^{-1}$ ; the growth rates are in the range of typical observed particle growth rates ( $1\text{--}20 \text{ nm h}^{-1}$ ) [59].

## 4. Conclusions

A combination of ground-based and satellite observations was used in this study to investigate different sources of aerosol BC loadings over Lithuania during two different time periods, April 24–30 and May 24–2, 2011. The 7-wavelength setup of the Aethalometer has been exploited to obtain information on variation of spectroscopic properties of carbonaceous particles. Although BC mass concentration values do not allow one to a priori determine which process produces BC, the wavelength dependence of the BC absorption gives the option to follow the variation carbonaceous aerosol properties and easily characterize the black carbon/organic component.

Near-source biomass burning smoke is observed routinely in Lithuania, while volcanic effluent plumes provided some new information. During these periods the measured

black carbon concentration during BB and volcanic activity events (3500 and 1200 ng m<sup>-3</sup>, resp.) exceeded previously established average values of 580 ng m<sup>-3</sup>. Compared to background aerosols, the sampled plumes have higher AOD and contain particles having expected differences in the Angstrom exponent and size. During the wildfire burning event on April 24–30 2011 the highest mean values of the Angstrom exponent of the absorption coefficients  $\alpha_{370-520}$  and  $\alpha_{590-950}$  nm were observed ( $1.4 \pm 0.1$  and  $2.2 \pm 0.1$ , resp.), and during the volcanic event on May 25–27, 2011 the peak values were determined ( $1.3 \pm 0.3$  and  $1.4 \pm 0.2$ , resp.). This is a strong suggestion that the aerosol includes less absorbers of the shorter wavelengths during the volcanic event.

The observational data and analysis presented here demonstrate that nucleation and subsequent growth can be derived from volcanic eruption gaseous released and that this new secondary particle formation event could occur within the lower troposphere at a large distance from the eruptive activity.

## Acknowledgments

This work was supported by the Lithuanian-Swiss Cooperation Programme “Research and Development” project AEROLIT (Nr. CH-3-ŠMM-01/08). The authors thank Piotr Sobolewski, Brent Holben, and Aleksander Pietruczuk and their staff for establishing and maintaining the Belsk site used in this investigation. The authors declare that they have no competing interests as defined by Advances in Meteorology or other interests that might be perceived to influence the results and discussion reported in this paper.

## References

- [1] M. L. Bell, J. M. Samet, and F. Dominici, “Time-series studies of particulate matter,” *Annual Review of Public Health*, vol. 25, pp. 247–280, 2004.
- [2] C. A. Pope and D. W. Dockery, “Health effects of fine particulate air pollution: lines that connect,” *Journal of the Air and Waste Management Association*, vol. 56, no. 6, pp. 709–742, 2006.
- [3] J. P. Schwarz, J. R. Spackman, D. W. Fahey et al., “Coatings and their enhancement of black carbon light absorption in the tropical atmosphere,” *Journal of Geophysical Research*, vol. 113, no. 3, Article ID D03203, 2008.
- [4] V. Ramanathan, F. Li, M. V. Ramana et al., “Atmospheric brown clouds: hemispherical and regional variations in long-range transport, absorption, and radiative forcing,” *Journal of Geophysical Research*, vol. 112, no. 22, Article ID D22S21, 2007.
- [5] P. J. Grutzen and M. O. Andreae, “Biomass burning in the tropics: impact on atmospheric chemistry and biogeochemical cycles,” *Science*, vol. 250, no. 4988, pp. 1669–1678, 1990.
- [6] P. G. Simmonds, A. J. Manning, R. G. Derwent et al., “A burning question: can recent growth rate anomalies in the greenhouse gases be attributed to large-scale biomass burning events?” *Atmospheric Environment*, vol. 39, no. 14, pp. 2513–2517, 2005.
- [7] M. O. Andreae and P. Merlet, “Emission of trace gases and aerosols from biomass burning,” *Global Biogeochemical Cycles*, vol. 15, no. 4, pp. 955–966, 2001.
- [8] Y. J. Kaufman, D. Tanré, and O. Boucher, “A satellite view of aerosols in the climate system,” *Nature*, vol. 419, pp. 215–223, 2002.
- [9] H. Huntrieser, J. Heland, H. Schlager et al., “Intercontinental air pollution transport from North America to Europe: experimental evidence from airborne measurements and surface observations,” *Journal of Geophysical Research*, vol. 110, no. 1, pp. 1–22, 2005.
- [10] D. M. Murphy, D. S. Thomson, and M. J. Mahoney, “In situ measurements of organics, meteoritic material, mercury, and other elements in aerosols at 5 to 19 kilometers,” *Science*, vol. 282, no. 5394, pp. 1664–1669, 1998.
- [11] B. G. Martinsson, C. A. M. Brenninkmeijer, S. A. Cam et al., “Influence of the 2008 Kasatochi volcanic eruption on sulfurous and carbonaceous aerosol constituents in the lower stratosphere,” *Geophysical Research Letters*, vol. 36, no. 12, Article ID L12813, 2009.
- [12] S. S. Abdalmogith and R. M. Harrison, “The use of trajectory cluster analysis to examine the long-range transport of secondary inorganic aerosol in the UK,” *Atmospheric Environment*, vol. 39, no. 35, pp. 6686–6695, 2005.
- [13] “TF-HTAP. Hemispheric Transport of Air Pollution,” in *Air Pollution Studies*, no. 16, United Nations Economic Commission for Europe, New York, NY, USA and Geneva, Switzerland, 2007, <http://www.htap.org/>.
- [14] J. F. Liu, D. L. Mauzerall, and L. W. Horowitz, “Source-receptor relationships of trans-pacific transport of East Asian sulfate,” *Atmospheric Chemistry and Physics*, vol. 8, pp. 5537–5561, 2008.
- [15] E. Saikawa, V. Naik, L. W. Horowitz, J. Liu, and D. L. Mauzerall, “Present and potential future contributions of sulfate, black and organic carbon aerosols from China to global air quality, premature mortality and radiative forcing,” *Atmospheric Environment*, vol. 43, no. 17, pp. 2814–2822, 2009.
- [16] R. Damoah, N. Spichtinger, C. Forster et al., “Around the world in 17 days—Hemispheric-scale transport of forest fire smoke from Russia in May 2003,” *Atmospheric Chemistry and Physics*, vol. 4, no. 5, pp. 1311–1321, 2004.
- [17] J. V. Niemi, H. Tervahattu, H. Vehkamäki et al., “Characterization and source identification of a fine particle episode in Finland,” *Atmospheric Environment*, vol. 38, no. 30, pp. 5003–5012, 2004.
- [18] D. Müller, I. Mattis, U. Wandinger, A. Ansmann, D. Althausen, and A. Stohl, “Raman lidar observations of aged Siberian and Canadian forest fire smoke in the free troposphere over Germany in 2003: microphysical particle characterization,” *Journal of Geophysical Research*, vol. 110, no. 17, Article ID D17201, pp. 75–90, 2005.
- [19] B. Langman, A. Folch, M. Hensch, and V. Matthias, “Volcanic ash over Europe during the eruption of Eyjafjallajökull on Iceland, April-May 2010,” *Atmospheric Environment*, vol. 48, pp. 1–8, 2012.
- [20] K. Kvietkus, J. Šakalys, J. Didžbalis, I. Garbarienė, N. Špirkauskaitė, and V. Remeikis, “Atmospheric aerosol episodes over Lithuania after the May 2011 volcano eruption at Grimsvötn, Iceland,” *Atmospheric Research*, vol. 122, pp. 93–101, 2013.
- [21] K. H. Lee, J. E. Kim, Y. J. Kim, J. Kim, and W. Von Hoyningen-Huene, “Impact of the smoke aerosol from Russian forest fires on the atmospheric environment over Korea during May 2003,” *Atmospheric Environment*, vol. 39, no. 1, pp. 85–99, 2005.
- [22] M. Sillanpää, R. Hillamo, S. Saarikoski et al., “Chemical composition and mass closure of particulate matter at six urban sites in

- Europe,” *Atmospheric Environment*, vol. 40, no. 2, pp. 212–223, 2006.
- [23] P. Anttila, U. Makkonen, H. Hellén et al., “Impact of the open biomass fires in spring and summer of 2006 on the chemical composition of background air in south-eastern Finland,” *Atmospheric Environment*, vol. 42, no. 26, pp. 6472–6486, 2008.
- [24] A. Karppinen, J. Härkönen, J. Kukkonen, P. Aarnio, and T. Koskentalo, “Statistical model for assessing the portion of fine particulate matter transported regionally and long range to urban air,” *Scandinavian Journal of Work, Environment and Health*, vol. 30, no. 2, pp. 47–53, 2004.
- [25] M. Sillanpää, A. Frey, R. Hillamo, A. S. Pennanen, and R. O. Salonen, “Organic, elemental and inorganic carbon in particulate matter of six urban environments in Europe,” *Atmospheric Chemistry and Physics*, vol. 5, no. 11, pp. 2869–2879, 2005.
- [26] J. Ovadnevaite, K. Kvietkus, and A. Maršalka, “2002 summer fires in Lithuania: impact on the Vilnius city air quality and the inhabitants health,” *Science of the Total Environment*, vol. 356, no. 1–3, pp. 11–21, 2006.
- [27] S. Saarikoski, M. Sillanpää, M. Sofiev et al., “Chemical composition of aerosols during a major biomass burning episode over northern Europe in spring 2006: experimental and modelling assessments,” *Atmospheric Environment*, vol. 41, no. 17, pp. 3577–3589, 2007.
- [28] V.-M. Kerminen, J. V. Niemi, H. Timonen et al., “Characterization of volcanic ash in southern Finland caused by the Grimsvötn eruption in May 2011,” *Atmospheric Chemistry and Physics*, vol. 11, pp. 12227–12239, 2011.
- [29] G. L. Schuster, O. Dubovik, and B. N. Holben, “Ångström exponent and bimodal aerosol size distributions,” *Journal of Geophysical Research*, vol. 111, no. 7, Article ID D07207, 2006.
- [30] Y. J. Kaufman, A. Gitelson, A. Karnieli et al., “Size distribution and scattering phase function of aerosol particles retrieved from sky brightness measurements,” *Geophysical Research Letters*, vol. 99, pp. 10341–10356, 1994.
- [31] A. Stohl, G. Wotawa, P. Seibert, and H. Kromp-Kolb, “Interpolation errors in wind fields as a function of spatial and temporal resolution and their impact on different types of kinematic trajectories,” *Journal of Applied Meteorology*, vol. 34, no. 10, pp. 2149–2165, 1995.
- [32] L. Giglio, “Characterization of the tropical diurnal fire cycle using VIRS and MODIS observations,” *Remote Sensing of Environment*, vol. 108, no. 4, pp. 407–421, 2007.
- [33] T. F. Eck, B. N. Holben, J. S. Reid et al., “Wavelength dependence of the optical depth of biomass burning, urban, and desert dust aerosols,” *Journal of Geophysical Research*, vol. 104, no. 24, pp. 31333–31349, 1999.
- [34] J. S. Reid, E. M. Prins, D. L. Westphal et al., “Real-time monitoring of South American smoke particle emissions and transport using a coupled remote sensing/box-model approach,” *Geophysical Research Letters*, vol. 31, no. 6, Article ID L06107, 5 pages, 2004.
- [35] R. E. Honrath, R. C. Owen, M. Val Martín et al., “Regional and hemispheric impacts of anthropogenic and biomass burning emissions on summertime CO and O<sub>3</sub> in the North Atlantic lower free troposphere,” *Journal of Geophysical Research*, vol. 109, no. 24, pp. 1–17, 2004.
- [36] A. Virkkula, T. Mäkelä, R. Hillamo et al., “A simple procedure for correcting loading effects of aethalometer data,” *Journal of the Air and Waste Management Association*, vol. 57, no. 10, pp. 1214–1222, 2007.
- [37] J. Sandradewi, A. S. H. Prévôt, E. Weingartner, R. Schmidhauser, M. Gysel, and U. Baltensperger, “A study of wood burning and traffic aerosols in an Alpine valley using a multi-wavelength Aethalometer,” *Atmospheric Environment*, vol. 42, no. 1, pp. 101–112, 2008.
- [38] S. Zappoli, A. Andracchio, S. Fuzzi et al., “Inorganic, organic and macromolecular components of fine aerosol in different areas of Europe in relation to their water solubility,” *Atmospheric Environment*, vol. 33, no. 17, pp. 2733–2743, 1999.
- [39] A. Ansmann, J. Bösenberg, A. Chikovsky et al., “Long-range transport of Saharan dust to northern Europe: the 11–16 October 2001 outbreak observed with EARLINET,” *Journal of Geophysical Research*, vol. 108, no. 24, pp. 1–15, 2003.
- [40] J. G. Goldammer, “The wildland fire season 2002 in the Russian Federation: an assessment by the global fire monitoring centre (GFMC),” *International Forest Fire News*, vol. 28, pp. 2–14, 2003.
- [41] A. E. Kardas, K. M. Markowicz, S. P. Malinowski et al., “SAWA experiment—properties of mineral dust aerosol as seen by synergic lidar and sun-photometer measurements,” *Atmospheric Chemistry and Physics Discussions*, vol. 6, pp. 12155–12178, 2006.
- [42] A. Pietruczuk and A. P. Chaikovsky, “Properties of fire smoke in Eastern Europe measured by remote sensing methods,” in *Remote Sensing of Clouds and the Atmosphere*, vol. 6745 of *Proceedings of SPIE*, October 2007.
- [43] H. Moosmüller, R. K. Chakrabarty, and W. P. Arnott, “Aerosol light absorption and its measurement: a review,” *Journal of Quantitative Spectroscopy and Radiative Transfer*, vol. 110, pp. 844–878, 2009.
- [44] M. Collaud-Coen, E. Weingartner, D. Schaub et al., “Saharan dust events at the Jungfraujoch: detection by wavelength dependence of the single scattering albedo and first climatology analysis,” *Atmospheric Chemistry and Physics*, vol. 4, no. 11–12, pp. 2465–2480, 2004.
- [45] T. W. Kirchstetter, T. Novakov, and P. V. Hobbs, “Evidence that the spectral dependence of light absorption by aerosols is affected by organic carbon,” *Journal of Geophysical Research*, vol. 109, no. 21, Article ID D21208, 12 pages, 2004.
- [46] M. Schnaiter, H. Horvath, O. Möhler, K. H. Naumann, H. Saathoff, and O. W. Schock, “UV–VIS–NIR spectral optical properties of soot and soot-containing aerosols,” *Journal of Aerosol Science*, vol. 34, pp. 1421–1444, 2003.
- [47] M. Schnaiter, C. Linke, O. Möhler et al., “Absorption amplification of black carbon internally mixed with secondary organic aerosol,” *Journal of Geophysical Research*, vol. 110, no. 19, Article ID D19204, pp. 1–11, 2005.
- [48] D. E. Day, J. L. Hand, C. M. Carrico, G. Engling, and W. C. Malm, “Humidification factors from laboratory studies of fresh smoke from biomass fuels,” *Journal of Geophysical Research*, vol. 111, no. 22, Article ID D22202, 2006.
- [49] A. Hoffer, A. Gelencsér, P. Guyon et al., “Optical properties of humic-like substances (HULIS) in biomass-burning aerosols,” *Atmospheric Chemistry and Physics*, vol. 6, no. 11, pp. 3563–3570, 2006.
- [50] V. Ulevičius, S. Byčėnkiėnė, V. Remeikis et al., “Characterization of aerosol particle episodes in Lithuania caused by long-range and regional transport,” *Atmospheric Research*, vol. 98, no. 2–4, pp. 190–200, 2010.
- [51] V. Ulevičius, S. Byčėnkiėnė, N. Špirauskaite, and S. Kecorius, “Biomass burning impact on black carbon aerosol mass concentration at a coastal site: case studies,” *Lithuanian Journal of Physics*, vol. 50, no. 3, pp. 335–344, 2010.

- [52] M. S. Reddy and C. Venkataraman, "Direct radiative forcing from anthropogenic carbonaceous aerosols over India," *Current Science*, vol. 76, no. 7, pp. 1005–1011, 1999.
- [53] R. von Glasow, N. Bobrowski, and C. Kern, "The effects of volcanic eruptions on atmospheric chemistry," *Chemical Geology*, vol. 263, no. 1-4, pp. 131–142, 2009.
- [54] S. M. Andersson, B. G. Martinsson, J. Friberg et al., "Composition and evolution of volcanic aerosol from eruptions of Kasatochi, Sarychev and Eyjafjallajökull in 2008–2010 based on CARIBIC observations during air space closure in April and May 2010," *Atmospheric Chemistry and Physics*, vol. 13, pp. 1781–1796, 2013.
- [55] O. Dubovik, B. Holben, T. F. Eck et al., "Variability of absorption and optical properties of key aerosol types observed in worldwide locations," *Journal of the Atmospheric Sciences*, vol. 59, no. 3, pp. 590–608, 2002.
- [56] A. K. Baker, A. Rauthe-Schöch, T. J. Schuck et al., "Investigation of chlorine radical chemistry in the Eyjafjallajökull volcanic plume using observed depletions in non-methane hydrocarbons," *Geophysical Research Letters*, vol. 38, Article ID L13801, 2011.
- [57] U. Schumann, B. Weinzierl, O. Reitebuch et al., "Airborne observations of the Eyjafjalla volcano ash cloud over Europe during air space closure in April and May 2010," *Atmospheric Chemistry and Physics Discussions*, vol. 10, no. 9, pp. 22131–22218, 2010.
- [58] M. Kulmala, T. Petäjä, P. Mönkkönen et al., "On the growth nucleation mode particles: source rates of condensable vapor in polluted and clean environments," *Atmospheric Chemistry and Physics*, vol. 5, no. 2, pp. 409–416, 2005.
- [59] M. Kulmala, H. Vehkamäki, T. Petäjä et al., "Formation and growth rates of ultrafine atmospheric particles: a review of observations," *Journal of Aerosol Science*, vol. 35, no. 2, pp. 143–176, 2004.